Eindige-elementenmodellering van biodegradeerbare stents

Finite Element Modelling of Biodegradable Stents

Nic Debusschere

Promotoren: prof. dr. ir. B. Verhegghe, prof. dr. P. Dubruel
Proefschrift ingediend tot het behalen van de graad van
Doctor in de Ingenieurswetenschappen: Biomedische Ingenieurstechnieken

Vakgroep Elektronica en Informatiesystemen
Voorzitter: prof. dr. ir. R. Van de Walle
Faculteit Ingenieurswetenschappen en Architectuur
Academiejaar 2015 - 2016

UNIVERSITEIT
GENT

ISBN 978-90-8578-881-2
NUR 929
Wettelijk depot: D/2016/10.500/13

Preface

During the last year of my master's studies in biomedical engineering, now five years ago, I wrote a thesis on finite element modelling of biodegradable polymeric stents, under supervision of my promoters prof. Bendedict Verhegghe and prof. Peter Dubruel. As I found the topic very interesting, I did not hesitate long when my tutor and personal coach Matthieu De Beule asked me whether I would like to continue my investigations more thoroughly as a PhD-researcher. So first of all, I am very thankful to my supervisors Bendedict and Peter for giving me the chance to do this research and for their valuable scientific input. Special thanks go to Matthieu who has been my main mentor during the past five years and who's scientific support and enthusiasm have been a key factor in the success of this PhD-research. Thanks also go to the director of the lab prof. Patrick Segers who supported me so well and who gave me so many opportunities to present my work all over the world on scientific conferences. Although this research topic was quite new at our lab, I received much help from my colleagues of the stent research group. Thank you Francesco, Sander, Gianluca, Mathias and Peter, your input has been very much appreciated. Not only does a doctorate give you the chance to see part of the world, also, the world comes to you. I have really enjoyed working within an international group of young colleagues. Thank you for the numerous Italian, Portuguese, Russian, Cuban, Colombian and Belgian parties and dinners! I have also liked assisting in teaching the courses of parametric modelling, of biomechanics and of biosystems. I was lucky to guide some very interested and clever master students with their thesis, whose work has proven very important for my own research. Thank you Wouter, Mathias and Arnout. And of course thanks to my friends and family, my sister and especially my parents for their infinite support.

Thank you very much!

Nic Debusschere, February 2016, Ghent

Samenvatting
Summary

Samenvatting

Biodegradeerbare stents

Het domein van de cardiologie onderging een revolutie in het begin van de jaren '90 van de vorige eeuw met de opkomst van minimaal invasivieve technieken zoals percutane coronaraire interventie (PCI) en het gebruik van stents. De eerste biodegradeerbare stents werden recent ontwikkeld. Een tijdelijk en bio-oplosbaar coronair implantaat kan mogelijk enkele van de complicaties van permanente metalen stents omzeilen, zoals in-stent restenose en late stent-trombose. De tijdelijke aard van biodegradeerbare stents laat bovendien bloedvathermodellering en herstel van vasomotie toe. Degradeerbare biomaterialen kunnen ook gebruikt worden als opslag voor lokale medicijnenafgifte. Hoofdstuk 1 geeft een kort historisch overzicht van de opkomst van coronaire angioplastie en de recente ontwikkelingen op het gebied van biodegradeerbare stents. Twee types materialen voor bio-oplosbare stents, biodegradeerbare polymeren en biocorrodeerbare metalen, worden uitgelicht. Dit hoofdstuk eindigt met een literatuurstudie van de biodegradeerbare stents die tot op heden ontwikkeld zijn en die de fase van klinische trial bereikt hebben.

Inleiding tot vaste-stofcontinuümmechanica, constitutieve materiaalmodellering en de eindige-elementenmethode

Tijdens de vier jaar onderzoek leidend tot deze doctoraatsthesis werd intensief gebruik gemaakt van computertechnieken en de eindige-elementenmethode in het bijzonder. Eindige-elementenanalyse (FEA) is een waardevolle en tijdsefficiënte manier om de mechanische performantie van biomedische implantaten zoals stents te evalueren. De ontwikkeling van biodegradeerbare stents zorgt voor nieuwe uitdagingen voor wat betreft deze mathematische en computationele methodes door hun complexe en tijdsafhankelijke materiaalgedrag. Hoofdstuk

2 geeft een inleiding tot vaste-stofcontinuümmechanica en constitutieve materiaalwetten. Het concept hyperelasticiteit wordt geïntroduceerd en de theoretische basis van de eindige-elementenmethode wordt uitgelicht. Het laatste deel van dit hoofdstuk focust op continuümschademechanica, dat ons in staat stelt wiskundige modellen voor materiaalgedrag en degradatiegedrag met elkaar te combineren.

Eindige-elementenmodellering van biodegradeerbare stents

Het aantal referenties in de wetenschappelijke literatuur over computermodelleren van biodegradeerbare stents is relatief beperkt. Toch hebben een aantal onderzoeksgroepen de laatste jaren interessant werk gepubliceerd omtrent het simuleren van de mechanica van biodegradeerbare stents. Hoofdstuk 3 geeft een overzicht van de in de literatuur beschikbare mathematische en computationele strategieën om het vergankelijke mechanisch gedrag van bioabsorbeerbare stents te simuleren. Zowel modellen voor polymere stents als voor biocorrodeerbare stents gemaakt uit metaallegeringen worden hier beschreven.

In vitro experimenten om de evolutie van de mechanische eigenschappen van een magnesiumlegering voor biodegradeerbare stents te karakteriseren

Een reeks *in vitro* experimenten werd uitgevoerd om de degradatie-eigenschappen en het mechanisch gedrag van een biocorrodeerbare magnesiumlegering te kunnen vaststellen. De resultaten van deze experimenten werden vervolgens gebruikt als input voor de beschikbare wiskundige materiaal- en degradatiemodellen. De experimentele methodologie en resultaten staan beschreven in hoofdstuk 4. Een inleidend deel van dit hoofdstuk wijdt uit over de fysicochemische processen die micro-galvanische corrosie en pitting corrosie veroorzaken. Vervolgens worden ook enkele standaard experimentele technieken voor het bepalen van materiaalmassaverlies en corrosiesnelheden van metaallegeringen beschreven. Van deze technieken werd gecombineerde onderdompeling in fysiologische zoutoplossing en meting van de vorming van waterstofgas voorgesteld als de preferentiële experimentele methode voor magnesiumlegeringen. Spannings-rekproeven op regelmatige tijdsintervallen lieten bovendien toe om de mechanische eigenschappen van de magnesiumlegering uit te zetten als functie van degradatietijd. Materiaalparameters en degradatieconstanten konden vervolgens afgeleid worden door vergelijking met de uitkomst van computersimulaties.

Computationeel raamwerk voor het modelleren van degradatie van biocorrodeerbare metallische stents door middel van een implicitie einde-elementenoplossingstechniek

De methodologie en resultaten beschreven in hoofdstuk 5 werden aanvaard voor publicatie in Annals of Biomedical Engineering. De ingezonden paper toont aan hoe mathematische modellen voor degradatie van magnesium kunnen worden aangewend voor de modellering van biocorrodeerbare metallische stents door gebruik te maken van een impliciete eindige-elementensolver. De uitdrukkingen voor bestaande modellen voor magnesium pitting corrosie en spanningscorrosie worden hier met elkaar vergeleken door middel van computersimulaties. De beschikbare materiaal- en degradatiemodellen werden geïmplementeerd in Fortran-code om compatibel te zijn me de commerciële eindige-elementsoftware Abaqus (Dassault Systèmes). Het gebruik van een impliciete eindige-elementensolver laat ons toe de simulatietijden aanzienlijk in te korten in vergelijking met een expliciet oplossingsschema. Als 'proof of concept' werden eerst een geometrisch model en eindige-elementenmesh gegenereerd van de Absorbable Metal Stent (AMS) (Biotronik) en vervolgens gecombineerd met de materiaalwetten om balloonexpansie in een vernauwd bloedvat te simuleren, en dit voor toenemende tortuositeit van de arterie. De simulatie-uitkomsten suggereren een invloed van de kromming van het bloedvat op de degradatiesnelheid van de stent.

Eindige-elementenstrategie voor het evalueren van de vrije ballonexpansie van een polymere biodegradeerbare stent

Hoofdstuk 6 vat het werk samen dat ook gepubliceerd werd als paper in Journal of Biomechanics. In deze studie werd een constitutief materiaalmodel geïmplementeerd dat het mechanisch gedrag van poly-L-lactide beschrijft, een biodegradeerbaar polyester dat de ruggengraat vormt van de Bioabsorbable Vascular Scaffold van Abbott. Dit constitutieve model houdt onder andere rekening met de viscoplastische eigenschappen van polymeren. Wij ontwikkelden ook een impliciete eindige-elementenstrategie om vrije expansie van een stent met ballon te modelleren, gebruik makend van een cylindrisch model van de ballon gecombineerd met anisotrope hyperelastische materiaaleigenschappen. Een reeks computersimulaties stelde ons vervolgens in staat de spanningen en rekken in de stent te evalueren, en dit voor

verschillende snelheden en drukken bij het opblazen van de ballon. De computeruitkomsten toonden aan dat de ontplooiingssnelheid van stent en ballon een grote impact kan hebben op de mechanische integriteit van deze polymere stent, en dit vanwege de visco-elasticiteit van het stentmateriaal. De studie bewees ook dat het mogelijk is om stent-ballonexpansie te modelleren door middel van een implicitie eindige-elemententechniek in plaats van een expliciete methode. Dit zorgt voor accurate output van spanningen en rekken en een grotere betrouwbaarheid van de resultaten door het afwezig zijn van dynamische en inertie-effecten. De gevolgde strategie stelde ons ook in staat typische fenomenen tijdens stentexpansie zoals 'dogboning' te visualiseren. De experimentele data die als input dienden voor deze studie werden bekomen door mechanisch testen van haltervormige poly-L-lactide specimens via lasersnijden uit polymere buisjes. Het materiaalmodel geeft een kwalitatieve indicatie over hoe graduele stentexpansie de opbouw van spanning in de stent en daaruitvolgend ook het risico op strutfracturen reduceert. Langzame ontplooiing van de stent kan mogelijk ook de initële elastische terugval van de stentdiameter beperken.

Conclusies

Het laatste hoofdstuk 7 vat de algemene conclusies van deze thesis samen, gaat in op de voornaamste limitaties van dit onderzoek en stelt enkele technieken voor toekomstige validatie voor. Eindige-elementenmodellering is uitgegroeid tot de gouden standaard als techniek voor het onderzoeken van de mechanische performantie van nieuwe minimaal invasieve protheses zoals stents. Bovendien laten computersimulaties toe bestaande stentgeometriën efficiënt te optimaliseren. De recente introductie van biodegradeerbare stents zorgt echter voor nieuwe uitdagingen wat betreft computermodelering door het complexe en tijdsafhankelijke materiaalgedrag van de biomaterialen waaruit deze stents zijn opgebouwd. Het onderzoek dat wordt voorgesteld in deze thesis heeft bijgedragen tot het algemene begrip van de mechanische eigenschappen van zowel bio-oplosbare polymeerstents als biocorrodeerbare metalen stents door middel van computersimulaties.

Summary

Biodegradable stents

The introduction of the techniques minimal invasive percutaneous coronary intervention (PCI) and stenting has revolutionized the field of cardiology in the beginning of the '90s. More recently, biodegradable stents have been developed, which carry the potential to avoid long-term complications of permanent bare metal and drug eluting stents, such as in-stent restenosis and late stent thrombosis. The temporary nature of these novel devices could allow for a restoration of vasomotion and vessel growth which makes them suitable for e.g. paediatric applications. Their bioresorbable backbone makes them an ideal vehicle for local drug delivery. Chapter 1 gives a brief historic overview of the advent of minimally invasive coronary angioplasty and stenting and the recent introduction of biodegradable coronary scaffolds. Both bioresorbable polymers and biocorrodible metals have been proposed as candidate materials for biodegradable stents. Some of the advantages and disadvantages of these different biomaterials are examined. A brief literature overview is given at the end of this chapter, listing the biodegradable stents that have been developed to date and that have reached clinical trial phase.

A brief introduction to solid mechanics, constitutive material modelling and the finite element method

During the four years of research leading to this thesis, intensive use was made of computational techniques and the finite element method in particular. Finite element analysis (FEA) has been proven to be a valuable and time efficient tool to evaluate the mechanical performance of biomedical implantable devices such as stents. The introduction of biodegradable stents poses new challenges to finite element modelling because of the evolving properties of the absorbable biomaterials. To be able to understand the methods used in this thesis, chapter 2 gives an introduction to solid mechanics and constitutive

material modelling. A definition of hyperelasticity is given and the theory behind finite element analysis is explained. The last section describes continuum damage mechanics, which will be used in subsequent chapters to couple constitutive material laws with models for material degradation.

Finite element modelling of biodegradable stents

Although the available references to mathematical methods to investigate the behaviour of biodegradable stents is relatively limited, a number of research groups have published interesting work about modelling of biodegradable scaffolds. Chapter 3 gives an overview of the available mathematical and computational methods presented in literature to model the transient mechanical behaviour of bioabsorbable stents during degradation. Both models for polymeric stents and metallic corrodible stents are presented in this chapter.

In vitro experiments to characterize the evolution of the mechanical properties of a biodegradable stent magnesium alloy

A series of in vitro degradation and mechanical experiments have been performed on a biocorrodible magnesium alloy to obtain input data for the available mathematical material and degradation models. The experimental methodology and results are given in chapter 4. The introduction of this chapter describes the mechanisms of micro-galvanic corrosion of metal alloys and the physicochemical phenomenon of pitting corrosion, followed by an overview of the available techniques to obtain mass loss and corrosion rates of metals. Combined immersion testing and measurement of hydrogen gas formation was chosen as the preferred method for testing. Tensile testing at regular time intervals allowed to obtain the evolution of mechanical properties for the magnesium alloy as a function of degradation time. Material parameters and degradation constants were then fit by iterative comparison with computer simulation results.

A computational framework to model degradation of biocorrodible metal stents using an implicit finite element solver

The methodology and results of chapter 5 have been accepted for publication in Annals of Biomedical Engineering. The paper presented

here shows how available models for magnesium corrosion can be used with an implicit finite element solver and can be applied to the modelling of biocorrodible magnesium stent mechanics. The behaviour of existing models for magnesium pitting corrosion and stress corrosion is compared by means of computer simulations. The available material and degradation models have been implementated into Fortran coded subroutines to be compatible with the commercial finite element solver Abaqus (Dassault Systèmes). The use of an implicit solver allows us to considerably speed up simulation times compared to an explicit finite element solution scheme. As a proof of concept, a geometrical model and mesh of the Absorbable Metal Stent (AMS) of Biotronik have been generated and applied to virtual expansion inside stenotic blood vessels with increasing degrees of tortuosity. The simulation outcomes indicate that blood vessel geometries might have an influence on the stent degradation rates.

A finite element strategy to investigate the free expansion behaviour of a biodegradable polymeric stent

Chapter 6 presents the work that has been published as a paper in Journal of Biomechanics. In this paper we implemented a constitutive material model for poly-L-lactic acid, a biodegradable polyester which forms the backbone of the Bioabsorbable Vascular Scaffold of Abbott. This constitutive model takes into account the viscoplastic behaviour of the material. An implicit finite element strategy was developed to model free balloon expansion of the stent, by making use of a cylindrical balloon model with anisotropic hyperelastic properties. A series of computer simulations were done, expanding the stent at different balloon pressurization rates. The computational results indicated that the deployment rate might have a large impact on the mechanical integrity of polymeric absorbable stents. The study showed that it is possible to use an implicit finite-element solver to model stent balloon expansion for which, to our knowledge, until now only explicit solvers have been used. An implicit solver benefits the accuracy and the reliability of the outputted stresses. It avoids dynamic inertia effects and therefore simplifies the interpretation of the simulation outcomes. The in this study presented implicit finite element solution strategy to model free balloon inflation of stents using a cylindrical balloon model and an anisotropic balloon material reflected well some of the stent's expansion characteristics such as the dogboning phenomenon. This chapter reveals insights in the direct mechanical behaviour of polymeric stents. Experimental data for input of material properties

was obtained by means of tensile testing on dumbbell shaped poly-L-lactic acid specimens cut out of cylindrical tubes. The material model gives a qualitative indication of how a gradual expansion procedure reduces the build-up of internal stresses and consequently the risk for strut fractures. Possibly, gradual expansion might also reduce the degree of elastic recoil after stent deployment.

Conclusions

The final chapter 7 summarizes the general conclusions of this thesis, lists the main limitations of this research and proposes some strategies for future validation of the here developed computer models. Finite element modelling has become a golden standard technique for investigating the feasibility and performance of new metallic stents and to optimize their geometry. The recent advent of biodegradable stents has posed new challenges for computer modelling because of the complex mechanical and degradation behaviour of their biomaterial backbones. The research presented in this thesis has contributed to the general understanding of the mechanical behaviour of both biodegradable polymeric and corrodible metallic stents via computer simulations.

Contents

List of Figures

List of Tables

One

Introduction

Chapter 1

Biodegradable stents

This chapter gives an introduction to ischaemic heart disease and coronary stenosis, and its treatment via minimally invasive percutaneous coronary intervention. A short history of the development of bare metal stents and the subsequent drug eluting stents is followed by the description of biodegradable stents. The last section of this chapter gives a literature overview of the biodegradable stents that have already been developed and have reached clinical trial phase.

1.1 Ischaemic heart disease and percutaneous coronary intervention

Ischaemic heart disease (IHD) is one of the most common causes of death worldwide and the main cause of death in Europe and in other western countries. The condition is caused by a disease called *atherosclerosis*, a local thickening of the arterial wall due to the accumulation of white blood cells and the proliferation of intimal smooth muscle cells that form a fatty plaque. These plaques contain both inflammation-producing living cells and a built up of dead cell materials including lipids and cholesterol. In a later stage, also calcifications of the plaque will form. Atherosclerosis occurs throughout the entire arterial system though manifests itself very locally – it is therefore a systemic disease with a focal distribution. Eventually, these atherosclerotic plaques will partially or entirely occlude the artery and cut off the supply of oxygen-rich and nutritious blood to the downstream

organs. Ischaemia of the heart occurs when such local narrowings or stenoses block the coronary arteries that oxygenate the heart muscle, and will eventually lead to myocardial infarction. Acute ischemia of the heart muscle or myocardial infarction also occurs when a blood cloth obstructs a coronary artery at the stenotic site. The mechanism of atherosclerosis and ischaemic heart disease is schematically depicted in Figure 1.1.

The sensitivity of the heart muscle to ischaemia is particularly high because the coronary arteries display a very low degree of redundancy. Figure 1.2 shows the main causes of death in Europe during the year 2014 [67]. As can be seen, mortality rates due to cardiovascular related diseases (CVD) are much higher for women (52%) than for men (42%). IHD accounts for about 20% of all causes of death, without distinction between both sexes. Risk factors for atherosclerosis and IHD include cigarette smoking, high blood pressure, high cholesterol levels, diabetes, obesity and a sedentary lifestyle in general. Also genetic factors play an important role. Projected statistics predict that IHD will be responsible for 13% of all deaths worldwide by the year 2030 [60].

Pharmaceutical or medical management – i.e. application of antianginal medication, use of statins, atihypertensives, smoking sessation, change of diet etc. – is mostly insufficient to relieve the symptoms of IHD and to take away the risk of cardiac infarction. The only option is often to alleviate the blockage or stenosis of the coronary arteries surgically. Since the 1970's, surgeons have been applying a technique called *coronary artery bypass grafting* (CABG), in which the patient's chest is opened and the stenosed coronary arteries are bypassed with a conduit of blood vessels that are harvested elsewhere, e.g. from the patient's limbs. Although CABG surgery has a high rate of success (nowadays a mortality rate of about 2-3%) [42], the operation is a severe and costly intervention with a rather high complication rate of 20-30%. Therefore, very soon, minimally invasive alternatives have been introduced. The field of interventional cardiology has witnessed a lot of progress since the introduction of *percutaneous coronary intervention* (PCI) at the beginning of the 1980's. Andreas Grüntzig et al. were the first to successfully apply a procedure called *percutaneous transluminal coronary angioplasty* (PTCA), by using an inflatable balloon mounted on the tip of a catheter. This catheter is inserted via a small peripheral incision (e.g. at the groin) and directed to the stenotic site via a guide wire and by using transluminal angiography. The balloon is then (repeatedly) pressurized to dilate

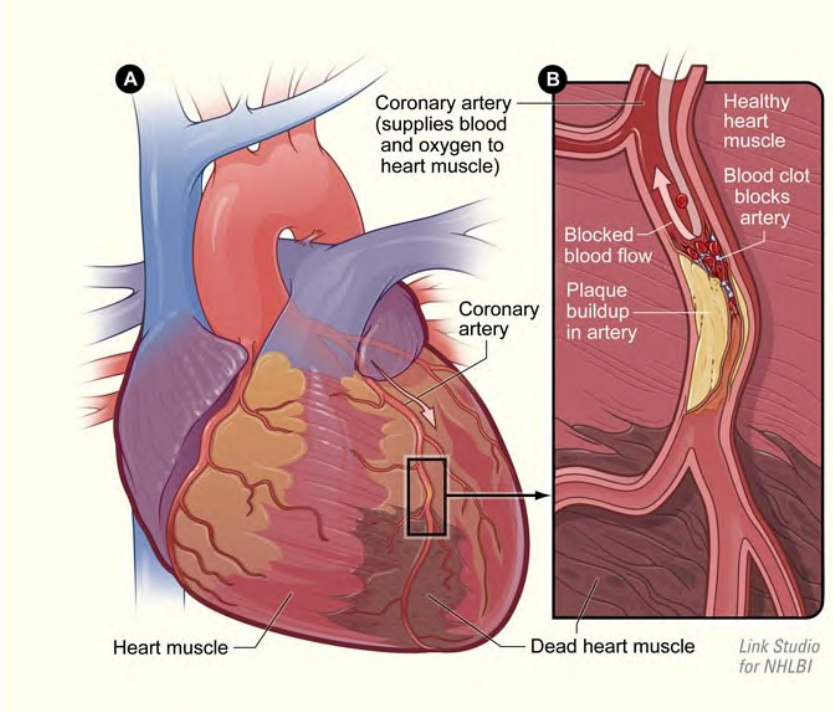

Figure 1.1: Ischaemic heart disease (IHD) occurs when a local narrowing of the coronary arteries blocks the supply of oxygen and nutritions to the heart muscle (Figure A.). Such a local narrowing or stenosis is usually caused by atherosclerosis, a systemic disease which manifests itself locally as the thickening of the arterial wall due to the accumulation of white blood cells and the proliferation of intimal smooth muscle cells that form a fatty plaque. A heart attack will occur when a blood cloth entirely obstructs the already narrowed coronary artery (Figure B.). Image taken from *National Heart, Lung, and Blood Institute, Diseases and Conditions Index* [68].

the occluded blood vessel and to compress the plaque. Early success rates and applicability of the procedure have been limited due to a number of complications of which acute vessel closure and *restenosis* are the most important. In general, balloon dilation induces damage and trauma of the arterial tissue and plaque which offsets a sequence of events including accumulation of platelets and fibrin, rupture of the plaque due to stretching sometimes resulting in dissection of the plaque, elastic recoil of the blood vessel and in a later stage constrictive remodelling of the artery. Accute occlusion occurs when the damaged blood vessel collapses (this was present in up to 8% of the cases) and often required emergency CABG surgery. Restenosis – or the renarrowing of the vessel – existed in 30 to 40% of the patients and occurs 6 months after PTCA and is caused by a complex combination

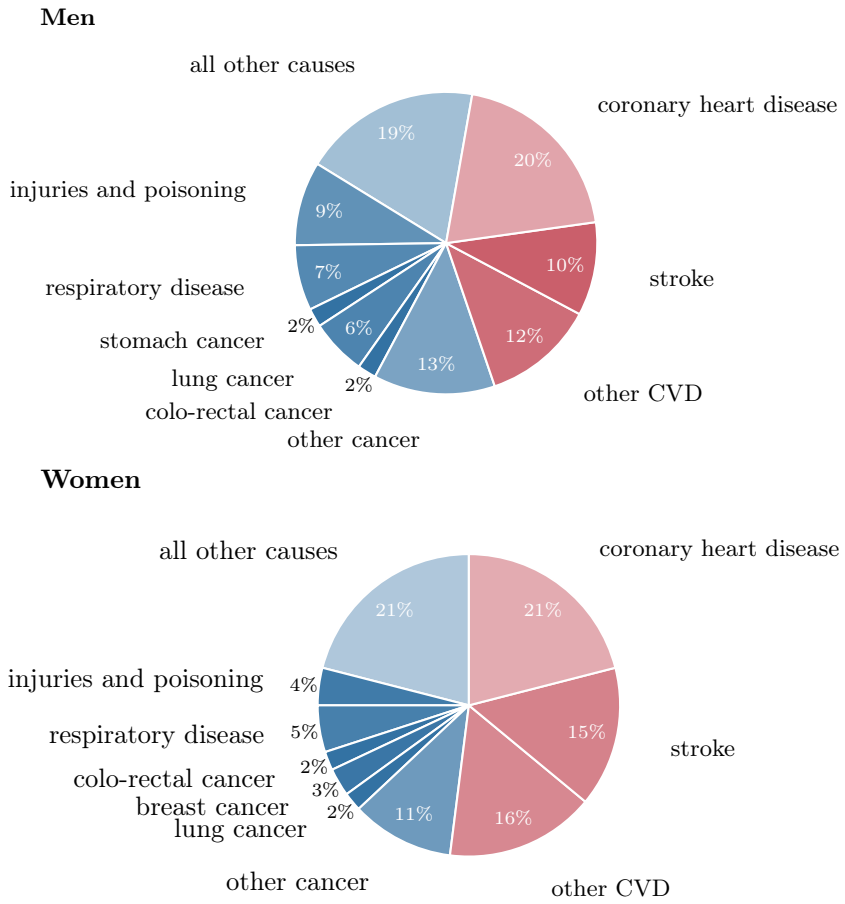

Figure 1.2: Main causes of death amongst men and women in Europe during the year 2014. The red colors of the chart indicate mortality due to cardiovascular diseases (CVD). In one out of five cases, coronary heart disease (CHD) was the cause of death for both men and women. Data taken from [67].

of mechanical and histological factors – such as inflammatory reactions, white blood cell migration, smooth muscle cell proliferation and constrictive remodelling – that result in the formation of scar tissue. Despite the obvious benefits of minimal invasive procedures – limited use of anaesthesia, a very short revalidation time and low cost for health care – rather poor clinical outcomes initially limited the use of PCI to about 5% of patients with IHD.

1.2 Bare-metal stents

Stents – small tubular spring-like devices to scaffold the artery after dilation – have been developed to prevent reocclusion of the arteries

treated with PTCA, to stabilize dissected plaque flaps and with the aim of diminishing restenosis. Figure 1.3 explains the stent placement procedure. The first succesfull implantations of coronary stents were performed in 1986 by Ulrich Sigwart and Jacques Puel and were the offset of a major revolution in medicine at the end of the '90s. Apart from scaffolding the stenotic lesion, a stent also counteracts posttraumatic vasospasms and prevents embolic complications. The combination of PTCA with *bare-metal stents* (BMS) – a term that was later introduced to distinguish between drug eluting stents – resulted in much better clinical outcomes compared to PTCA alone. The BENESTENT study was a clinical trial conducted in Belgium and the Netherlands in 1993 and showed that restenosis rates could be reduced from 32% to 22% and the number of patients undergoing target lesion revascularisation (TLR) – i.e. repeated PCI or CABG to the same site – reduced from about 30% for PTCA alone to 10% with bare metal stenting.

Important complications of the first generation cardiovascular stents – next to mechanical failure of the device – were caused by the thrombogenic effect of the foreign object and *in-stent restenosis*. In-stent restenosis is the excessive growth of scar tissue covering the stent struts and is caused by a combination of neointimal proliferation of endothelial cells, the deposition of platelets, the formation of blood cloths and the built-up of an extracellular matrix (cfr. Figure 1.4a). The reaction of the body to a foreign object such as a bare metal stent which is exposed to the blood stream can be generally characterized by four phases. First, there is a large increase in the number of subendothelial cells and platelets start to coagulate resulting in the formation of blood cloths. The second phase is characterized by inflammation of the blood vessel wall, with a peak one week post stenting. During the third phase, smooth muscle cells proliferate in the medial and intimal layers of the artery. The last phase involves remodelling of the blood vessel in an attempt to restore the homeostatic balance as a reaction on the changes in the physiological and mechanical environment caused by the presence of the stent. Stent thrombosis, which initially occurred in 16% of the patients, can be largely suppressed by the use of antithrombotic medicines. In-stent restenosis however remained high, in about 20% to 25% of the patients undergoing bare metal stent angioplasty, with even much higher incidence – up to 80% – in subgroups such as for diabetic patients. This number could only be reduced with the emergence of drug eluting stents.

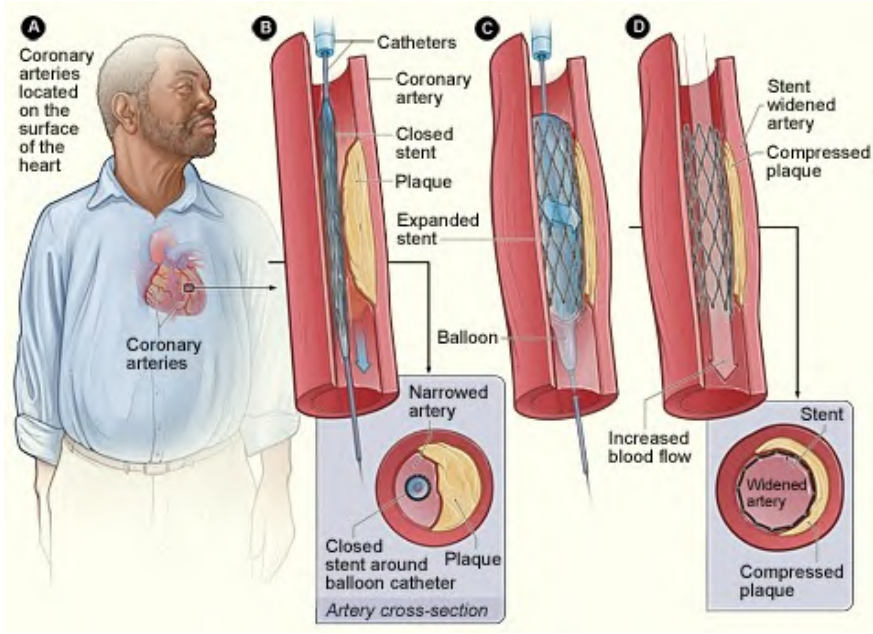

Figure 1.3: Percutaneous coronary intervention (PCI) with stent placement is a minimally invasive alternative for open chest coronary artery bypass surgery, to relieve the symptoms of ischeamic heart disease (Figure A.). A stent – a small tubular structure to scaffold the stenotic artery – is initially mounted on a catheter tip in its crimped configuration. The catheter is directed to the stenotic site by sliding it over a guide wire. Transluminal angiographic radiography aids in positioning the guidewire and the catheter tip with the stent (Figure B.). Usually, the stent is mounted on a small inflatable balloon. Water then pressurizes the balloon and expands the stent (Figure C.). Next to balloon-expandable stents, also self-expandable stents exist. The plastic properties of the stent material (or shape-memory/super-elastic properties of self-expandable stents) make sure that the stent maintains its expanded configuration. The opened stent now widens the arterial stenosis, thereby restoring blood flow and delivery of oxygen to the heart muscle (Figure D.). Image taken from *National Heart, Lung, and Blood Institute, Diseases and Conditions Index* [68].

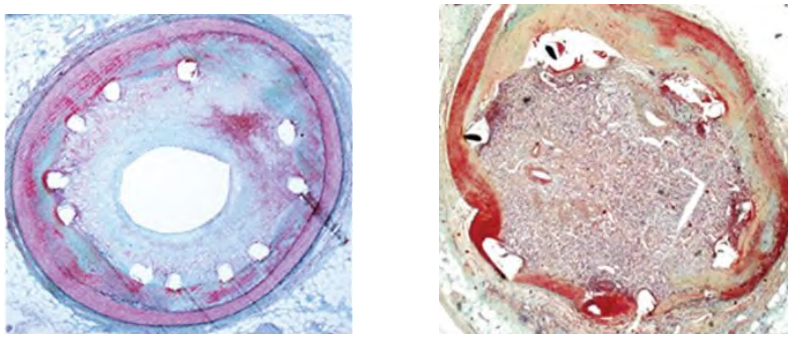

(a) In-stent restenosis **(b)** Stent thrombosis

Figure 1.4: These histological images taken from [66] show two common complications of bare metal stents and drug eluting stents. Figure 1.4a shows a case of severe in-stent restenosis, which is the renarrowing of the artery due to excessive scar tissue formation. Figure 1.4b shows a case of stent thrombosis, where a blood cloth is formed that completely occludes the artery.

1.3 Drug eluting stents

To counteract neointimal hyperplasia – and consequently in-stent restenosis – the metallic surface of stents has been covered with an anti-proliferative drug eluting coating. These *drug eluting stents* (DES) were expected to eliminate restenosis and the need for TLR or reintervention. The most common pharmaceutical agents for DES are the cell proliferation inhibitor paclitaxel and the immuno-suppressant sirolimus (also known as rapamycin[1]). Clinical trials with DES (e.g. the RAVEL-trial [62], the SIRIUS-trials [46] and the TAXUS-trials[76]) have demonstrated the superiority of DES over BMS by reducing restenosis rates with over 74%. One year and two year follow-up indicated that the stents were safe and DES were approved for use in Europe and the USA starting from 2002. Despite their higher cost compared to BMS, because of their good clinical outcomes, DES became soon the preferred device for PCI, with about 90% of all implanted stents being DES around the year 2006. However, since then, the enthusiasm for DES has been tempered because of increasingly frequent reports of late *in-stent thrombosis* (cfr. Figure 1.4b). In-stent thrombosis can occur many years after stent placement and happens when the protective drug eluting cover fails and partially detaches, thereby exposing the underlying metallic surface to the blood stream

[1]The active agent of rapamycin is produced by the fungus *Streptomyces hygroscopicus* which was first discovered in soil samples on Easter Island. The name rapamycin was derived from the island's indigenous name, Rapa Nui. Paclitaxel is harvested from the bark of the pacific yew tree *Taxus brevifolia*.

and triggering thrombus formation. Because the drug eluting cover inhibits cell growth, there is no intimal cell layer barrier shielding the stent struts from the blood stream as is the case for BMS. When in-stent thrombosis occurs, it has often fatal consequences: myocardial infarction and death incidence after DES thrombosis range between 45% and 75%. In-sent thrombosis risk for DES ranges between 0.5% and 4%. New generation DES aim at reducing the risk of in-stent thrombosis by the development of safer coatings and by improving coating biocompatibility by partially allowing smooth muscle cell coverage. However, since the introduction of PCI and stenting almost 40 years ago, cardiologists have stated that a stent should only temporarily scaffold the dilated artery. When the artery is fully healed, the stent is no longer necessary and should gradually disappear so to allow the artery to regain its normal functioning. The general idea behind a biodegradable stent is illustrated in Figure 1.5. The realization of such a *biodegradable stent* has long been hindered due the lack of candidate materials. Only recently, biodegradable stents are being used in clinical practice.

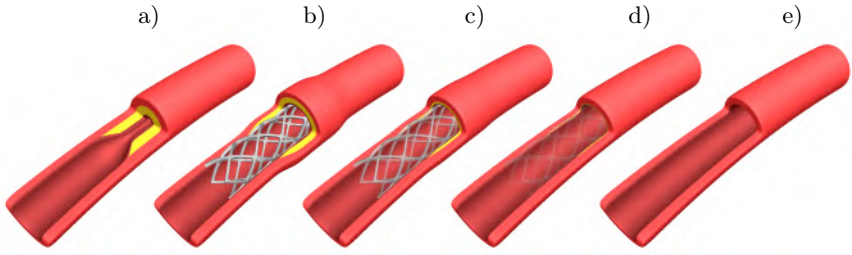

Figure 1.5: Illustration of the general idea behind an ideal biodegradable stent. An atherosclerotic plaque locally narrows a coronary artery (a). A biodegradable stent is implanted to restore blood flow and oxygen delivery to the heart muscle (b). General drug administration and local drug delivery help in the healing of the artery. In meantime, the stent is degrading though maintains sufficient structural integrity to keep the blood vessel opened (c). Eventually, the stent material will be fully absorbed by the arterial tissue (d). The gradual transition of the load from the stent to the blood vessel wall allows for restoration of vasomotion (e).

1.4 Biodegradable stents

Onuma et al. [72] have listed the following potential advantages of a fully biodegradable stent:

- Late adverse effects such as in-stent thrombosis can be avoided.
- The gradual softening and absorption of the stent material allows for remodelling of the blood vessel and restoration of vasomotion.
- Patients with stents undergo long term antiplatelet therapy to reduce the risk of blood cloth formation. The temporary presence of the biodegradable stent would allow to stop administration of anticoagulants after a certain period so to reduce the risk of bleeding complications.
- Repeated treatment of IHD is often restricted to CABG because the metallic cages of previously implanted stents hinder the placement of new devices. A biodegradable stent instead allows repeated treatment to the same site.
- Non-metallic biodegradable scaffolds are – unlike metallic stents – compatible with non-invasive imaging techniques such as computed tomography (CT) or magnetic resonance (MR) scanning which facilitates long term follow-up of patients.
- The bioabsorbable material matrix could provide an excellent reservoir for the local elution of anti-inflammatory and antiproliferative drugs. In future they can serve as a vehicle for gene delivery systems.

Figure 1.6 shows the evolution of the characteristics of an ideal biodegradable stent and summarizes the above listed properties. The stented artery has a healing period of about six months during which the stent must deliver sufficient radial support [73]. Afterwards, the stent should gradually soften to ensure a smooth transition of the mechanical load from the biodegradable scaffold to the artery, allowing the blood vessel to regain vasomotion. Full stent absorption should preferentially occur within a range of one or two years. Biodegradable stents can also prove particularly interesting for diseases other than IHD and atherosclerosis, e.g. for paediatric applications.

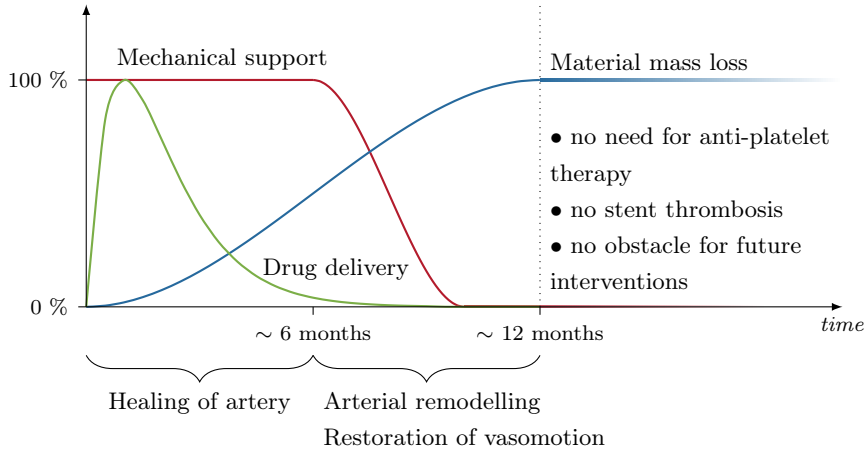

Figure 1.6: Schematic representation of the evolution of the characteristics of an ideal biodegradable stent. The blue curve plots the progression of material mass loss, indicating that the stent should have fully disappeared after about one year. The red curve represents the evolution of the stent's mechanical strength, which should be maintained within the first six months of arterial healing. Gradual softening of the bioabsorbable material allows for restoration of vasomotion and arterial remodelling. The green curve shows how the stent matrix can be used as a vehicle for drug delivery. Once the stent has fully disappeared, it is no obstacle for future intervention. Anti-platelet therapy can be avoided and there is no risk for late stent thrombosis.

The main challenges in the development of a biodegradable stent are in making a scaffold that has sufficient radial strength for an appropriate duration, that does not have unduly thick struts, that can be a drug delivery vehicle and where degradation does not generate an unacceptable inflammatory response [50]. Candidate materials for biodegradable stents can be generally subdivided into two groups: biodegradable polymers and biocorrodible metal alloys. Most of the investigated biodegradable polymers belong to the group of the aliphatic polyesters, including polylactic acid (PLA), polyglycolic acid (PGA) and polycaprolactone (PCL). These polyesters can be tailored to have well-defined degradation kinetics but have relatively poor mechanical properties, with a much lower Young's modulus and tensile strength compared to materials for DES such as stainless steel or cobalt chromium. Aliphatic polyesters disintegrate via a bulk degradation process during which the molecular mass is reduced by hydrolytic scission of the polymer chains. Biodegradable metal alloys have material properties more closely resembling those of conventional stents and degrade via corrosive surface erosion, which in vivo is a more complex and unpredictable mechanism. Table 1.1 lists the mechanical and degradation times for a number of candidate materials for

biodegradable stents. None of the listed materials combine all characteristics of an ideal biodegradable stent. The optimal stent might be a corrodible metallic stent covered with a bioabsorbable polymeric coating because it would combine the best characteristics – controlled degradation kinetics and biocompatibility vs. mechanical strength – of both material classes.

1.4.1 Biodegradable polymeric stents

During the past two decades, several biodegradable stents have been developed and have reached the clinical trial phase. A number of these stents are shown in Figure 1.7 and are listed in table 1.2. Poly(L-lactic acid) (PLLA) forms the backbone of the two oldest and most extensively investigated and trialled biodegradable stents, the Igaki-Tamai stent (Kyoto Medical Planning Co.) and the Bioresorbable Vascular Scaffold (Abbott Vascular) [108]. PLLA belongs to the class of the aliphatic polyesters and had previously proven excellent biocompatibility as a material for bioabsorbable sutures. It was also the development of high molecular weight (HMW) PLLA for these sutures which provided the appropriate candidate material for biodegradable stents. HMW PLLA is synthesized via ring opening polymerisation (ROP) of lactide, a cyclic monomer and was first commercialized by the company Cargill Inc, and requires highly pure lactide [7]. The first

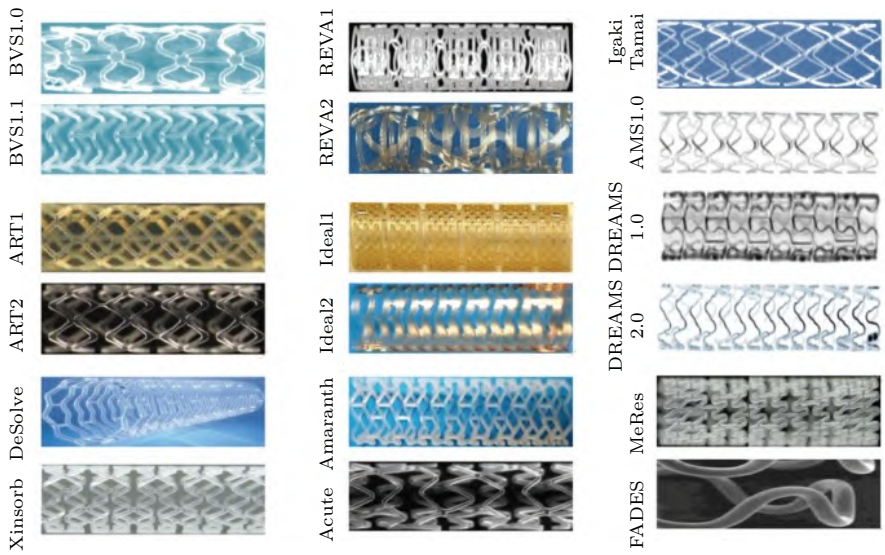

Figure 1.7: A number of biodegradable stents that are under development and/or have reached clinical trial phase. The images are taken from [108].

attempts to make biodegradable stents were simply made by knitting of absorbable sutures, but failed because they were not able to deliver sufficient support for vascular scaffolding [18]. The Igaki-Tamai stent was the first fully biodegradable stent to be implanted in humans in 1999, with a complete absorption time of 18 to 24 months [70]. A clinical trial on 50 patients showed good outcomes at 4-year follow-up with a high rate of overall survival (97.7%), and a relatively low degree of TLR (18%). Clinical interest in this first biodegradable stent was however limited because of the advent of DES around the same time and the stent's rather cumbersome deployment method involving heating with contrast agent at 80°C, so that the development of this cardiovascular stent has eventually been stopped. New Igaki-Tamai stent designs have however been created for use in the peripheral region.

The Bioresorbable Vascular Scaffold (BVS) has a semi-crystalline ultra-high molecular weight (UHMW) PLLA backbone and is coated with an everolimus eluting[2] poly(D,L-lactic acid) (PDLLA) layer [82] [24]. The stent geometry resembles those of many conventional metallic stents – a series of zigzag hoops that act as plastic hinges, linked by straight interconnecting segments – though with thicker (150 μm) struts to compensate for the lower elastic modulus. The stent is deployed via balloon expansion and has radio-opaque markers at its

[2]Like sirolimus, everolimus is a derivative of rapamycin and acts as an immunosuppressant and an inhibitor of restenosis.

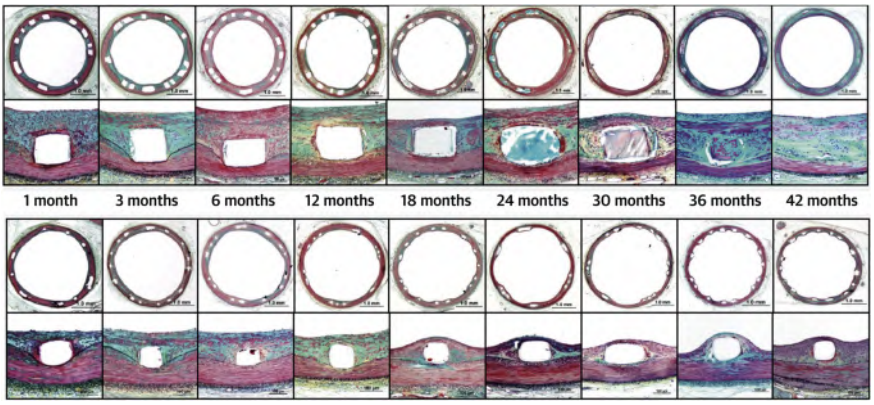

Figure 1.8: These histological images taken from [100] show the evolution of the arterial wall morphology for the Absorb BVS (upper images) compared to an everolimus-eluting DES (lower images) at different time points up to 42 months. The blood vessel wall lumen remains opened as the stent material is absorbed. After 42 months, almost all stent material has been absorbed and a healthy vessel with restored vasomotion remains.

ends to allow visibility during transluminal angiography. The polymeric chains of the PLLA and PDLLA material are gradually broken down into lactic acid which is then metabolised in the Krebs cycle. Like the Igaki-Tamai device, full absorption of the BVS is obtained after 24 months or longer. The stent has extensively been tested in the Absorb I [24] (30 patients) and Absorb II [23] (500 patients) clinical trials, comparing the performance of the biodegradable stent with an everolimus-eluting DES (the Xience-stent). Four-year follow-up of the degradable scaffold has proven clinical safety with few major adverse cardiac events (MACE), low restenosis rates and no cases of stent thrombosis (see also Figure 1.9). The trials indicated however insufficient scaffolding ability of the device, therefore the design of the stent has been optimized for a higher radial strength in the ABSORB II trial. The BVS has since 2012 been approved with the European CE marking [1] which makes it the first commercially available biodegradable coronary stent. Till now, the BVS has however a limited range of applicability and therefore, the new running Absorb III and planned Absorb IV trials will include in total 5000 patients with more complex coronary lesions [44]. One year follow-up during the Absorb III trial already showed no significant difference between the Absorb group and the group of patients implanted with the reference Xience-stent in rates of MACE. Stent thrombosis within 1 year was slightly higher in the Absorb group (1.5% vs 0.7%) [25].

The Ideal-stent (Bioabsorbable Therapeutic Inc.) was a poly(anhydride ester/salicylic acid) backbone biodegradable stent covered with a sirolimus coating and promised biodegradability in combination with anti-inflammatory and antiproliferative properties [80]. Poor results of the first in man (FIM) trial for this stent with respect to restenosis rates were attributed to the stent's very thick struts and a insufficient sirolimus dose which led to the development of a new Ideal BioStent (Xenogenics Corporation), which is currently undergoing preclinical evaluation [33].

The REVA stent (Boston Scientific) was made of a poly(tyrosine derived carbonate) polymer chemically modified with iodine to obtain a radio-opaque polymer [72]. The polymer molecular weight (MW) could be modified to obtain degradation times between 12 and 24 months. Unlike the polymeric stents mentioned above, stent deployment is not based on the plastic hinge principle but by using a slide-and-lock mechanism. The stent underwent clinical trial for 30 patients to investigate stent safety. Despite good results such as absence of vessel recoil at 6 months, the stent had a high rate of TLR

(66.7%) caused by mechanical failure of the device due to polymer embrittlement. A better stent design and modifications to the polymer have led to a more mechanically stable device called the ReZolve stent. First clinical trials with this new device showed excellent acute performance with minimal acute recoil [3].

Another poly-L-lactic acid polymeric stent is being developed by Elexir Medical Corporations (Sunnyvale, CA, USA) and contains two novel antiproliferative drugs (Novolimus and Myolimus) [108], and has been given the name DESolve. Like with other PLLA-stents, complete absorption takes about 2-3 years. The safety and performance of this stent have been evaluated in a FIM trial on 16 patients in Belgium and New Zealand. Optical coherence tomography (OCT) data showed that 99% of the stent struts were fully covered at 6 monts with only a minor reduction in lumen area. These promising initial clinical data have resulted in a new clinical trial – the DESolveNX-trial – including 126 patients.

The Xinsorb bioresorbable scaffold is a PLLA stent developed by Huaan Biotechnology (Hangzhou, China) [105]. The stent underwent preclinical evaluation using porcine models and a FIM implantation with a 35-year old patient suffering myocardial infarction [17]. Other PLLA-stents that have been deployed for pre-clinical testing in porcine models include the ART stent (Arterial Remodeling Technologies, Noisy le Roi, France) and the Amaranth absorbable stent (Amaranth Medical Inc. , Mountain View, CA, USA).

1.4.2 Biodegradable metallic stents

The second class of biodegradable materials for stents is represented by the biocorrodible metals. To date, the Absorbable Metal Scaffold (AMS) of Biotronic is the only biocorrodible stent that has reached clinical trial phase (cfr. table 1.2). It is made of a magnesium-aluminium-zinc alloy (alloy WE43), which, when it corrodes, brakes down into metal salts that are naturally present inside the human body and that can consequently completely be resorbed and metabolised, with little associated inflammatory response [27, 71, 74]. Biocorrodible metals have the advantage of material strength over biodegradable polymers, resulting in stents with thinner struts[3], which has been proven to be beneficial in terms of restenosis rates [16]. On the other hand, in vivo metal corrosion is a very complex and impredictable process involving physical phenomena (pitting corrosion, stress

[3]The struts of the AMS stent are however still a factor > 1.5 times thicker than for stainless steel or cobalt-chromium stents, to compensate for the lower elastic modulus and tensile strength (cfr. table 1.1).

corrosion cracking, ...) as wel as biological mechanisms (enzymetic reactions, effect of cell adhesion, ...). This makes it difficult to design a stent that is able to ensure sufficient radial strength for an appropriate duration. Other limitations lay in the development of stent manufacturing techniques that do not deteriorate the integrity of the material. The mechanical properties of the stent can be tuned via metal alloying and pre-processing techniques [106].

The AMS has been evaluated in three clinical trials – the PROGRESS trial and the DREAMS-1 and DREAMS-2 trials – each time with modifications to the design of the stent. The PROGRESS trial included 63 patients and resulted in a high (45%) incidence of TLR at 4 months follow-up [14]. This was mainly due to too fast resorption of the device – the device was completely resorbed in less than 4 months – which caused almost immediate loss of radial strength. A new device was developed with a modified magnesium alloy composition and an optimized geometry. The AMS-2 device was first tested in animal models and later improved with a paclitaxel-eluting biodegradable polymer coating. The performance of this DREAMS stent (where DREAMS stands for DRug Eluting AMS) has first been investigated in the BIOSOLVE-1 study (46 patients). The outcome was much better than for the first AMS, with a rate of TLR of 4.3% at 6 months, no cardiac deaths and no stent thrombosis [51]. Two year follow-up data were presented in 2013 and showed 6.8% target lesion failure, but no cardiac death or stent thrombosis. The magnesium stent was further optimized in terms of geometry and a sirolimus-eluting PLLA coating for better anti-proliferation properties, resulting in DREAMS-2, which is currently being studied in the BIOSOLVE-II trial (120 patients).

Next to magnesium alloys, pure iron has also been investigated as a biodegradable material for stents. Pure iron performs better than magnesium with respect to mechanical characteristics, with material properties resembling those of stainless steel (table 1.1. The stent has been evaluated in animal models (rabit and pig) [79]. Its degradation rate has been reported to be too slow for in human applicability, possibly due to the formation of a passivating oxide layer [54]. No iron-based biodegradable stent has reached clinical trial phase.

1.4.3 Applications for biodegradable scaffolds other than coronary stenting

The development of biodegradable stents has mainly focussed on coronary artery lesions. However, the advantages of a temporary

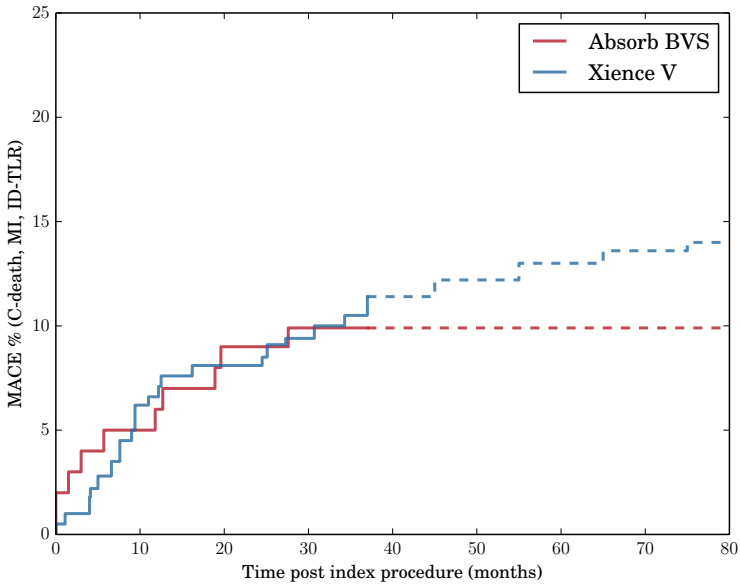

Figure 1.9: Kaplan-Meier plot of cumulative major adverse cardiac events (MACE) (including cardiac mortality (C-death), any myocardial infarction (MI) or ischaemic driven target lesion revascularisation (TLR)) for the bioresorbable vascular scaffold (BVS) Absorb B cohort (101 patients) compared with a 226 patients control group who received a Xience V stent (an everolimus-eluting DES). Image data are taken from [82] and show that the biodegradable stent and the permanent DES have similar event rates at 3 year follow-up. Prior to 10 months, MACE are more frequent for the absorbable stent, possibly due to the stent's lower mechanical properties and bulky struts. Interestingly, the cumulative event curve then flattens for the Absorb group. The dashed lines show how the event rates could possibly further evolve: events will continue to accumulate for the Xience V group due to the permanent presence of the stent, while MACE-rates for the Absorb group will be lower and not related to the BVS stent itself, which has disappeared after 30 months.

scaffold could also apply to stenting of blood vessels in the peripheral region. Stents and stent materials for applications in limbs can require high mechanical demands when they undergo large and repetitive (cyclic) deformations. The previously mentioned coronary Igaki-Tamai stent has been redesigned to be used in patients with occlusive superficial femoral artery (SFA) disease [99] and is now being evaluated in a 30 patient study. The stent seems to be safe, however relatively high restenosis rates have been reported.

Peuster et al. have reported long-term biocompatibility in pigs of a peripheral, fully corrodible pure iron stent. The aim of this biocorrdible stent is to be used for treatment of vascular obstructions in patients with congenital heart defects [75]. Treatment with permanent stents in these very young patients is limited because the blood vessels need to grow. Here, biodegradable scaffolds might provide a good solution. Studies in pigs have indicated that the iron stents are safe with neointimal proliferation comparable to permanent stainless steel stents. However, degradation times are rather long with most of the material remaining intact one year after implantation.

Usage of stents is not restricted to blood vessels, but can also be applied to other constricted tube-like anatomical regions. Oesophageal stents are used as a palliative treatment of patients suffering oesophageal cancer. The main purpose is to allow passage of food through the oesophagus, thereby somewhat comforting the end of the patient's life. For patients with benign constrictions of the oesophagus, e.g. due to benign tumours or as a result of caustic ingestions, no permanent stent can be inserted as it would become fully embedded in the surrounding tissue. Non-degradable oesophageal stents for benign strictures therefore have to be removed and replaced at short time intervals. Here, biodegradable scaffolds could provide a solution. An example of a biodegradable oesophageal stent is the ELLA-stent

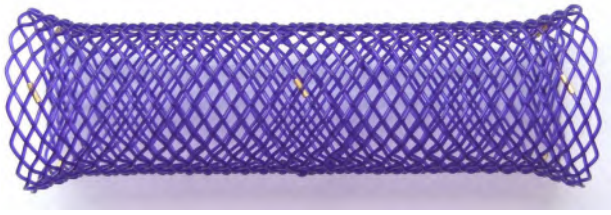

Figure 1.10: An example of an oesophageal biodegradable stent (SX Ella-BD stent, Ella-CS, Hradec Kralove, Czech Republic). The stent is made of bioabsorbable woven polydioxanone suture wires.

(SX Ella-BD stent, Ella-CS, Hradec Kralove, Czech Republic), which is made of woven biodegradable polydioxanone wires. The geometry of the stent is shown in Figure 1.10. Stivaros et al. have mentioned that patients with benign strictures should only be considered for biodegradable oesophageal stent insertion if conventional dilatation has had no significant improvement [92].

1.4.4 Biodegradable stents: strengths and weaknesses

Figure 1.9 shows a result from the Absorb B clinical trial for the Abbott BVS. The graph plots the cumulative incidence of major adverse cardiac events (MACE) during 38 months post stenting – this type of figure is referred to as a Kaplan-Meier plot – and includes data for a 101 patients group who received a biodegradable stent (red curve) and another group of 226 patients for whom a drug eluting Xience V stent was implanted (blue curve). Both stents are everolimus-eluting. The data indicate that the stents perform equally well at 3 year follow-up, with a cumulative MACE incidence of about 10%. During the first 10 months however, MACE-rates are higher for the absorbable scaffold. This can be due to a number of factors, e.g. the stent bulk material drug release is insufficient to prevent in-stent restenosis, the stent has not enough mechanical strength to support the blood vessel, the bulky struts of the stent partially occlude the blood vessel or induce excessive neo-intimal cell growth. Many of the here mentioned weaknesses can be attributed to the novelty of this stent and will be improved in future via engineering and fine-tuning of drug release, polymer composition and molecular weight and stent design. However, it is likely that biodegradable stents – both polymeric and metallic – will always be mechanically inferior to permanent metallic scaffolds. Also, current clinical trials with biodegradable stents have been limited to relatively mild atherosclerotic lesions, for blood vessels with low tortuosity and with exclusion of coronary bifurcations. This could mean that in future trials including patients with more complex lesions, initial MACE incidence rates will be higher than the values in Figure 1.9. Here, computer models and finite element analysis (FEA) can play an important role in expanding the applicability of biodegradable stents by improving stent geometries and by virtual classification of different absorbable scaffolds for different atherosclerotic lesions. After 10 months, the steepness of the red curve in Figure 1.9 decreases so that MACE incidences are the same as for the Xience V stent at 3 year follow up. The dashed lines in Figure 1.9 predict what would be the Kaplan-Meier plots at long terms. Assuming that all absorbable stent material has disappeared at 30 months, MACE

would become rare for the Absorb BVS and not related to the stent itself (because absent), while the blue curve would remain to increase as major cardiac events accumulate. Although such long term clinical outcomes are not yet available for biodegradable stents, this expected result would mean an obvious advantage of bioresorbable scaffolds over permanent prostheses. Even more importantly, the same stenotic lesion could be retreated with a stent in case of MACE, thereby avoiding open chest bypass graft surgery. Repeated stenting to the same stonotic site is therefore one of the major strengths of biodegradable scaffolds. Another obvious benefit of absorbable scaffolds lays in the restoration of the blood vessel wall and of vasomotion (unhindered by a metallic cage, cfr. Figure 1.8), which can be particularly important for young patients.

It is clear that, with several absorbable stents under development and with some of these stent's having obtained regulatory approval, biodegradable stents will play an increasingly important role in clinical practice. These biodegradable devices will be made of a wide range of biomaterials – including polymers and corrodible metal alloys – and will have many different geometries. To efficiently evaluate the mechanical properties of these novel devices, and to be able to classify different devices for different atherosclerotic lesions, computer models can prove a very useful tool. During this doctoral research, a number of strategies have be developed to model the mechanical behaviour of biodegradable stents using finite element analysis. To be able to understand the methods used later in this thesis, the next chapter gives an introduction to solid mechanics, the finite element method and continuum damage mechanics.

Table 1.1: Mechanical properties and *in vivo* degradation times for a number of candidate biodegradable stent materials. A selection of materials for DES have been included for comparison.

Material	Young's modulus [GPa]	Tensile strength [MPa]	Elongation at break [%]	Degradation time *in vivo* [mo]	Reference
cobalt chromium L605	243	1000	50	–	[77]
stainless steel 316L	193	670	43	–	[77]
nitinol	45	700 - 1100	10 - 20	–	[72]
platinum chromium	190 - 210	700 - 1300	27 - 40	–	[39]
poly-L-lactic acid (PLLA)	3.1 - 3.7	60 - 70	2 - 6	> 24	[72]
poly-D,L-lactic acid (PDLLA)	3.1 - 3.7	45 - 55	2 - 6	6 - 12	[72]
polyglycolic acid (PGA)	6.5 - 7.0	90 - 110	1 - 2	6 - 12	[72]
polycaprolactone (PCL)	0.25 - 0.33	11 - 13	430 - 490	< 24	[81]
50/50 PDLLA/PGA	3.4 - 3.8	40 - 50	1 - 4	1 - 2	[72]
82/18 PLLA/PGA	3.3 - 3.5	60 - 70	2 - 6	12 - 18	[72]
70/30 PLLA/PCL	0.02 - 0.04	18 - 22	> 100	12 - 24	[72]
magnesium alloy AZ31	44	235	7	< 9 [a]	[39]
magnesium alloy WE43	45	280	10	< 7 [a]	[39]
pure iron	200	210	40	N.A.	[43]

[a] Estimation based on *in vivo* corrosion rate values for a reference stent with 0.1 mm thick struts.

Table 1.2: Bioresorbable polymeric and biocorrodible metal coronary stents that have reach clinical trial stage. Data taken from [13].

Stent name (company)	Strut material	Strut thickness [µm]	Degradation time [mo]	Current status
AMS-1 (Biotronik)	magnesium alloy	165	< 4	stopped
DREAMS-1 (Biotronik)	magnesium alloy	120	9	stopped
DREAMS-2 (Biotronik)	magnesium alloy	125	24	clincal trial
Igaki-Tamai (Kyoto Medical)	poly(L-lactic acid)	170	18 - 24	stopped
Absorb BVS 1.0 (Abbott)	poly(L-lactic acid)	156	18 - 24	stopped
Absorb BVS 1.1 (Abbott)	poly(L-lactic acid)	156	18 - 24	CE-marked
Absorb BVS 2.0 (Abbott)	poly(L-lactic acid)	156	18 - 24	CE-marked
REVA (Boston Scientific)	poly(tyrosine derived carbonate)	200	24	stopped
ReZolve (Boston Scientific)	poly(tyrosine derived carbonate)	200	24	clinical trial
Fantom (Boston Scientific)	poly(tyrosine derived carbonate)	228	24	clinical trial
Pure Bioresorbable Scaffold (ART)	poly(L-lactic acid)	170	3 - 6	CE-marked
Fortitude (Amaranath Medical)	poly(L-lactic acid)	200	3 - 6	clinical trials
DESolve (Elixir)	poly(L-lactic acid)	150	12 - 24	CE-marked
Ideal (Bioabsorbable Therapeutic Inc.)	poly(anhydride ester)/salicylic acid	200	6 - 9	stopped
Ideal Biostent (Xenogenics)	poly(anhydride ester)/salicylic acid	150	6 - 9	pre-clinical

CHAPTER 2

A brief introduction to solid mechanics, constitutive material modelling and the finite element method

The results presented in this work were obtained by use of computational finite element analysis. This chapter gives a brief introduction to the solid mechanics mathematical framework, the general definition of deformation and stress, and the principal of virtual work which forms the basis for the finite element method for structural mechanics. A definition of isotropic and anisotropic hyperelasticity is given and a number of hyperelastic strain energy density functions are described. Finite element discretization is explained and two commonly used solution techniques, the explicit and implicit solution method, are explained. Finally, continuum damage theory is introduced and illustrated to form the basis for the modelling of mechanical material degradation of bioabsorbable stents. This chapter gives a general introduction to continuum mechanics and the finite element method. For a more detailed description of these theoretical concepts the reader is referred to the Abaqus theory manual [84] or for example [47], [37] and [10].

2.1 Deformation, strain and strain rate

2.1.1 Deformation

Consider the solid body $\mathscr{B}$ in figure 2.1, represented by the configuration $\mathcal{B}_0$ in 3D space, $\mathcal{B}_0 \subset \mathbb{R}^3$. During a given time interval $t \in [0, t_1] \subset \mathbb{R}^+$, the body $\mathscr{B}$ is deformed to a configuration $\mathcal{B}_t \subset \mathbb{R}^3$. From now on, let us call $\mathcal{B}_0$ the reference configuration of $\mathscr{B}$ and $\mathcal{B}_t$ the current configuration of $\mathscr{B}$. A material point $\boldsymbol{p}$ inside $\mathscr{B}$ had a spatial position represented by the vector $\vec{\boldsymbol{X}}$ in the reference configuration, which has been updated to $\vec{\boldsymbol{x}}$ in the current configuration. The associated displacement of $\boldsymbol{p}$ is given by the vector $\vec{\boldsymbol{u}} = \vec{\boldsymbol{x}} - \vec{\boldsymbol{X}}$. The relation $\boldsymbol{\chi}_t\left(\vec{\boldsymbol{X}}\right) : \mathcal{B}_0 \times \mathbb{R} \to \mathbb{R}^3$ maps the reference coordinates $\vec{\boldsymbol{X}}$ of any material point $\boldsymbol{p}$ onto the current coordinates $\vec{\boldsymbol{x}} = \boldsymbol{\chi}_t\left(\vec{\boldsymbol{X}}\right) \in \mathbb{R}^3$. The *deformation gradient* tensor $\boldsymbol{F}$ is an important concept in finite strain theory and is defined as

$$\boldsymbol{F} \coloneqq \partial_{\vec{\boldsymbol{X}}} \chi(\vec{\boldsymbol{X}}, t) = \frac{\partial \vec{\boldsymbol{x}}}{\partial \vec{\boldsymbol{X}}} \tag{2.1}$$

It characterises local deformation at $\boldsymbol{p}$ by projecting neighbouring points $d\vec{\boldsymbol{X}}$ of $\boldsymbol{p}$ onto $d\vec{\boldsymbol{x}}$ in the current configuration, $d\vec{\boldsymbol{x}} = \boldsymbol{F} d\vec{\boldsymbol{X}}$. According to polar decomposition theorem, the deformation gradient $\boldsymbol{F}$ can be uniquely decomposed into an orthogonal rotation tensor $\boldsymbol{R}$ and symmetric tensors $\boldsymbol{U}$ and $\boldsymbol{V}$ respectively representing material stretch and spatial stretch.

$$\boldsymbol{F} = \boldsymbol{R}\boldsymbol{U} = \boldsymbol{V}\boldsymbol{R} \tag{2.2}$$

From the point of view of the reference configuration, the deformation gradient thus expresses a sequence of material deformation and a rigid body rotation. Useful measures of deformation or stretch can be found through elimination of $\boldsymbol{R}$ by left and right side tensor multiplication of $\boldsymbol{F}$ with its transpose $\boldsymbol{F}^T$, resulting in the so-called left and right *Cauchy-Green tensors* $\boldsymbol{b}$ and $\boldsymbol{C}$.

$$\boldsymbol{b} = \boldsymbol{F}\boldsymbol{F}^T = \boldsymbol{V}^2, \quad \boldsymbol{C} = \boldsymbol{F}^T\boldsymbol{F} = \boldsymbol{U}^2 \tag{2.3}$$

2.1.2 Strain

Whereas *stretch* expresses true deformation, the concept *strain* is used to give the deviation of the current configuration from the rigid body

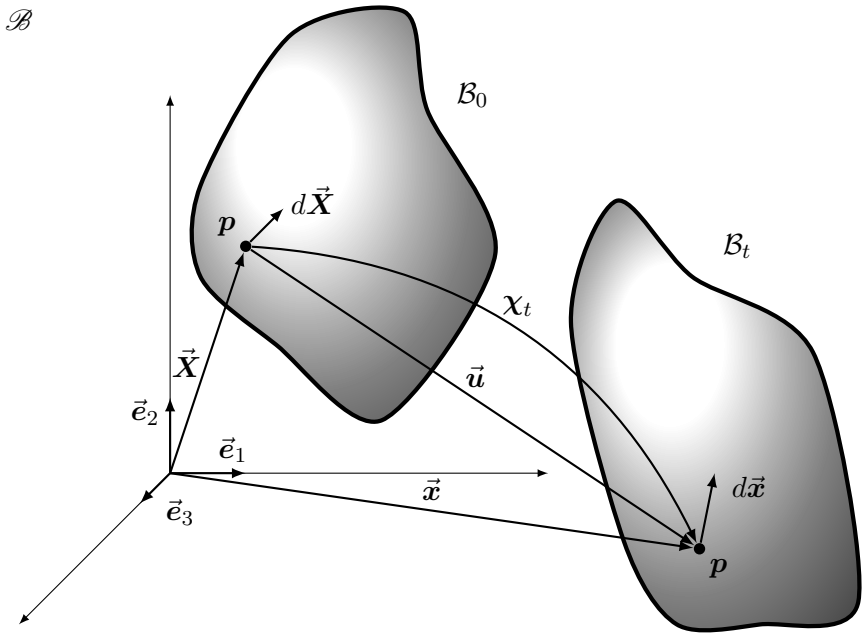

Figure 2.1: Deformation of a solid body $\mathscr{B}$. $\boldsymbol{\chi}_t$ represents the motion of the body $\mathscr{B}$ from the reference geometry $\mathcal{B}_0$ to the deformed geometry $\mathcal{B}_t$, mapping the reference coordinates $\vec{\boldsymbol{X}}$ of a material point $\boldsymbol{p}$ onto the current coordinates $\vec{\boldsymbol{x}}$. The displacement of $\boldsymbol{p}$ is given by the vector $\vec{\boldsymbol{u}}$ while local deformation at $\boldsymbol{p}$ can be expressed by the deformation gradient $\boldsymbol{F} = \partial\vec{\boldsymbol{x}}/\partial\vec{\boldsymbol{X}}$, which projects material positions $d\vec{\boldsymbol{X}}$ in the vicinity of $\boldsymbol{p}$ onto $d\vec{\boldsymbol{x}}$ in the current configuration.

displacement. A convenient measure of strain is given by the *Green-Lagrange strain* tensor $\boldsymbol{E}$.

$$\boldsymbol{E} = \frac{1}{2}\left(\boldsymbol{U}^2 - \mathbf{1}\right) = \frac{1}{2}\left(\boldsymbol{F}^T\boldsymbol{F} - \mathbf{1}\right) \tag{2.4}$$

Here, $\mathbf{1}$ represents the second order unit tensor having components $1_{ij} = \delta_{ij}$ with δ_{ij} the Kronecker-δ, which equals to one if $i = j$ and to zero otherwise. In terms of tensor components E_{ij} of $\boldsymbol{E}$ this results in the following expression

$$E_{ij} = \frac{1}{2}\left(\frac{\partial u_j}{\partial X_i} + \frac{\partial u_i}{\partial X_j} + \sum_k \frac{\partial u_i}{\partial X_k}\frac{\partial u_k}{\partial X_j}\right) \tag{2.5}$$

from which we can derive the classical definition of infinitesimal strain $\boldsymbol{\varepsilon}$ by assuming the mixed terms to disappear when deformations

become infinitely small.

$$\varepsilon_{ij} = \frac{1}{2}\left(\frac{\partial u_j}{\partial X_i} + \frac{\partial u_i}{\partial X_j}\right) \tag{2.6}$$

Other measures of deformation include the stretch tensor $\boldsymbol{U}$ and its eigenvalues (also known as principal stretches $\lambda_{i=1,2,3}$) and the logarithmic or 'true' strain $\boldsymbol{\varepsilon}_{log} = ln\,(\boldsymbol{V})$. We can express the volume change ratio in the vicinity of $\boldsymbol{p}$ by calculation of the determinant J of the deformation gradient, $J = \det(\boldsymbol{F})$. The scalar variable J is often referred to as the 'Jacobian' or the 'third invariant of strain' and is a measure for local material compression ($J < 1$) or expansion ($J > 1$). A material is said to be incompressible if $J := 1$ in all material points of $\mathscr{B}$ for any configuration $\mathcal{B}_t$.

2.1.3 Strain rate

The classical mechanical quantities *velocity* and *acceleration* can be derived for the material point movement $\boldsymbol{x}$ as the first and second order rate of change of the position vector $\vec{\boldsymbol{x}}$, $\vec{\boldsymbol{v}} = \dot{\vec{\boldsymbol{x}}} = \partial\vec{\boldsymbol{x}}/\partial t$ and $\vec{\boldsymbol{a}} = \ddot{\vec{\boldsymbol{x}}} = \partial^2\vec{\boldsymbol{x}}/\partial t^2$. The spatial velocity gradient tensor $\boldsymbol{L}$ is then defined as the gradient of the velocity vector field in the vicinity of p for the current configuration.

$$\boldsymbol{L} = \frac{\partial\vec{\boldsymbol{v}}}{\partial\vec{\boldsymbol{x}}} = \frac{\partial\vec{\boldsymbol{v}}}{\partial\vec{\boldsymbol{X}}}\frac{\partial\vec{\boldsymbol{X}}}{\partial\vec{\boldsymbol{x}}} = \frac{\partial}{\partial t}\frac{\partial\vec{\boldsymbol{x}}}{\partial\vec{\boldsymbol{X}}}\frac{\partial\vec{\boldsymbol{X}}}{\partial\vec{\boldsymbol{x}}} = \dot{\boldsymbol{F}}\boldsymbol{F}^{-1} \tag{2.7}$$

This tensor is for practical reasons often decomposed into a symmetric tensor $\boldsymbol{D}$ called the rate of deformation, and its anti-symmetric counterpart $\boldsymbol{W}$, the spin tensor.

$$\boldsymbol{D} = \frac{1}{2}\left(\boldsymbol{L} + \boldsymbol{L}^T\right), \quad \boldsymbol{W} = \frac{1}{2}\left(\boldsymbol{L} - \boldsymbol{L}^T\right) \tag{2.8}$$

Using the definition of logarithmic strain $\boldsymbol{\varepsilon}_{log} = ln\,(\boldsymbol{V})$ it is straightforward to show that $\boldsymbol{D}$ represents the logarithmic strain rate $\dot{\boldsymbol{\varepsilon}}_{log}$.

$$\dot{\boldsymbol{\varepsilon}}_{log} = \frac{1}{2}\frac{\partial}{\partial t}ln\left(\boldsymbol{V}^2\right) = \frac{1}{2}\frac{\partial}{\partial t}ln\left(\boldsymbol{F}\boldsymbol{F}^T\right) = \frac{1}{2}\left(\dot{\boldsymbol{F}}\boldsymbol{F}^{-1} + \boldsymbol{F}^{-T}\dot{\boldsymbol{F}}^T\right) = \boldsymbol{D} \tag{2.9}$$

2.2 Stress

To understand the mechanical concept *stress* we imagine an infinitely small surface area dS in the vicinity of the material point $\boldsymbol{p}$ at an intersection of the solid body $\mathscr{B}$ with current configuration $\mathcal{B}_t$ as shown in Figure 2.2. The traction force per unit area acting on $\boldsymbol{p}$ is represented by the vector $\vec{\boldsymbol{t}}$. With $\vec{\boldsymbol{n}}$ the normal unit vector characterizing the intersection surface dS, the 'true' stress or Cauchy stress $\boldsymbol{\sigma}$ at $\boldsymbol{p}$ is defined through:

$$\vec{\boldsymbol{t}} = \vec{\boldsymbol{n}}.\boldsymbol{\sigma}. \tag{2.10}$$

The Cauchy-stress $\boldsymbol{\sigma}$ is a symmetric 3×3-tensor and relates internal forces caused by deformation to the current configuration. Another frequently used measure of stress is the Kirchhoff stress $\boldsymbol{\tau}$, which relates to $\boldsymbol{\sigma}$ via $\boldsymbol{\tau} = J\boldsymbol{\sigma}$ with J the determinant of the deformation gradient $\boldsymbol{F}$. In finite strain theory, it is often convenient to define internal stresses with respect to the reference configuration, which can be obtained through the (generally non-symmetric) Piola-Kirchhoff stress tensor $\boldsymbol{P}$.

$$\boldsymbol{P} = J\boldsymbol{\sigma}\boldsymbol{F}^{-T} \tag{2.11}$$

A symmetric tensor can be derived via a pull-back operation to obtain the second Piola-Kirchhoff stress tensor.

$$\tilde{\boldsymbol{P}} = \boldsymbol{F}^{-1}\boldsymbol{P} = J\boldsymbol{F}^{-1}\boldsymbol{\sigma}\boldsymbol{F}^{-T} \tag{2.12}$$

The stress tensor $\boldsymbol{\sigma}$ can be subdivided into a hydrostatic pressure term p caused by local volume deformations, and the remaining so-called deviatoric stress $\boldsymbol{S}$.

$$\boldsymbol{\sigma} = \boldsymbol{S} - p\boldsymbol{1} \ , \ p = -\mathrm{tr}(\boldsymbol{\sigma})/3 \tag{2.13}$$

Here $\mathrm{tr}(\bullet)$ stands for the trace of a tensor, $\mathrm{tr}(\boldsymbol{\sigma}) = \sum \sigma_{ii}$. An often used scalar measure of stress is the Von Mises stress $\tilde{\sigma}$ which is defined through the deviatoric stress components S_{ij} as:

$$\tilde{\sigma} = \sqrt{\frac{2}{3}\sum_{i,j} S_{ij}S_{ij}} \tag{2.14}$$

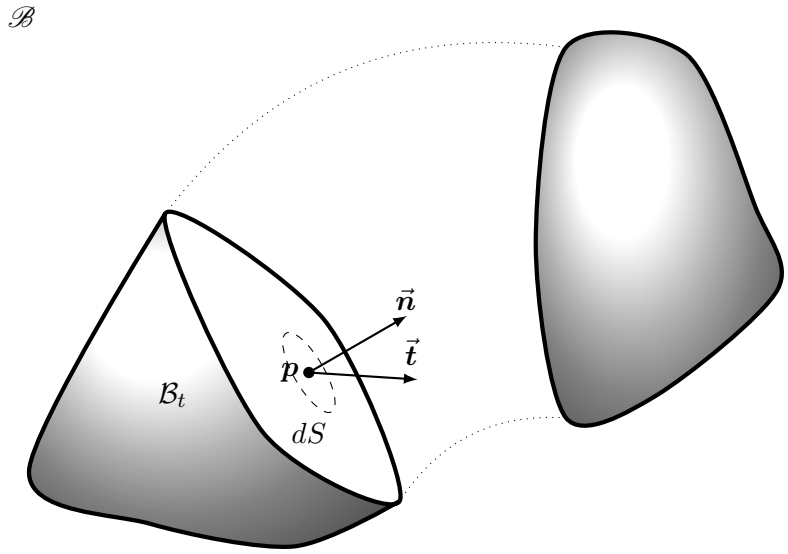

Figure 2.2: Definition of stress inside a solid body $\mathscr{B}$. The Cauchy stress tensor $\boldsymbol{\sigma}$ characterizes the traction force $\vec{\boldsymbol{t}}$ at a material point $\boldsymbol{p}$ that is acting on an arbitrary intersection surface dS through $\boldsymbol{p}$ with normal unit vector $\vec{\boldsymbol{n}}$, within the current configuration $\mathcal{B}_t$.

2.3 Constitutive material equations, isotropic linear elasticity and hyperelasticity

2.3.1 Linear elasticity

A constitutive equation relates the deformation of a solid body with the resulting internal stresses. For infinitesimal (i.e. small) deformations, material behaviour can be described as a function of infinitesimal strain $\boldsymbol{\varepsilon}$ as defined in equation 2.6, and the Cauchy stress $\boldsymbol{\sigma}$. For isotropic linear elastic materials, the relation between strain and stress is given by Hooke's law:

$$\sigma_{ij} = \lambda \mathrm{tr}(\boldsymbol{\varepsilon})\delta_{ij} + 2\mu\varepsilon_{ij} \tag{2.15}$$

Here, λ and μ are two scalar parameters called the Lamé constants. The relation 2.15 can also be written as the double tensor dot product of a fourth order stiffness tensor $\mathbb{C}$ and $\boldsymbol{\varepsilon}$,

$$\boldsymbol{\sigma} = \mathbb{C} : \boldsymbol{\varepsilon} = (\lambda \mathbf{1} \otimes \mathbf{1} + 2\mu\mathbb{I}) : \boldsymbol{\varepsilon} \tag{2.16}$$

or

$$\boldsymbol{\sigma} = \mathbb{C} : \boldsymbol{\varepsilon} = \left(\kappa \mathbf{1} \otimes \mathbf{1} + 2\mu \left(\mathbb{I} - \frac{1}{3} \mathbf{1} \otimes \mathbf{1} \right) \right) : \boldsymbol{\varepsilon} \tag{2.17}$$

where $\mathbb{I}$ is a fourth order unit tensor with components $\mathbb{I}_{ijkl} = 1/2(\delta_{ik}\delta_{jl} + \delta_{il}\delta_{jk})$ and $\otimes$ stands for the dyadic product of two tensors. The Lamé constants λ, μ and κ are related to Young's modulus E and the Poisson ratio ν as:

$$\lambda = \frac{\nu E}{(1+\nu)(1-2\nu)} \ , \ \mu = \frac{E}{2(1+\nu)} \ , \ \kappa = \frac{E}{3(1-2\nu)} \tag{2.18}$$

2.3.2 Hyperelasticity

The constitutive equations explained in the previous section are often sufficient to describe the mechanical behaviour of common engineering materials such as steel or concrete that are undergoing small deformations, or to describe the elastic regime of plastically deforming metals. However, many materials, such as rubbers or biological tissues, are able to undergo large elastic deformations, where the linear elastic material laws do no longer yield. The mechanical behaviour of these *hyperelastic* materials must be described within a finite strain framework. Hyperelastic materials can be characterized by a *strain energy density function* ψ, a scalar field that gives the elastic potential energy per unit of volume that is stored inside a material when subjected to deformation. For isotropic hyperelastic materials, the Piola-Kirchhoff stress tensor can be obtained through

$$\boldsymbol{P} = \frac{\partial \psi \left(\boldsymbol{F} \right)}{\partial \boldsymbol{F}} \tag{2.19}$$

Based on definition 2.11, the Cauchy stress is given by

$$\boldsymbol{\sigma} = \frac{1}{J} \frac{\partial \psi \left(\boldsymbol{F} \right)}{\partial \boldsymbol{F}} \boldsymbol{F}^T \tag{2.20}$$

The volume preserving part $\bar{\boldsymbol{F}}$ of the deformation gradient can be found as $\bar{\boldsymbol{F}} = J^{-1/3}\boldsymbol{F}$ so that per definition $\det(\bar{\boldsymbol{F}}) = 1$. The hyperelastic energy density function is then often split into a volume dependent and a deviatoric part as $\psi(\boldsymbol{F}) = \bar{\psi}(\bar{\boldsymbol{F}}) + \psi_{vol}(J)$. In general, for isotropic materials, the strain energy function $\bar{\psi}$ should further be independent of the chosen reference coordinate system and is

therefore usually written in terms of the first and second invariant of deformation, $\bar{I}_1$ and $\bar{I}_2$.

$$\psi(\boldsymbol{F}) = \bar{\psi}(\bar{I}_1, \bar{I}_2) + \psi_{vol}(J) \tag{2.21}$$

$$\bar{I}_1 = \mathrm{tr}(\bar{\boldsymbol{b}}) = \mathrm{tr}(\bar{\boldsymbol{C}}) \tag{2.22}$$

$$\bar{I}_2 = \frac{1}{2}\left(\bar{I}_1^2 - \mathrm{tr}(\bar{\boldsymbol{b}}^2)\right) = \frac{1}{2}\left(\bar{I}_1^2 - \mathrm{tr}(\bar{\boldsymbol{C}}^2)\right) \tag{2.23}$$

In equations 2.22 and 2.23, $\bar{\boldsymbol{b}} = J^{-2/3}\boldsymbol{b}$ and $\bar{\boldsymbol{C}} = J^{-2/3}\boldsymbol{C}$ are the left and right volume-preserving Cauchy-Green tensors. Under the condition of equation 2.21, the definition of the hyperelastic stress state 2.20 can be transformed into

$$\boldsymbol{\sigma} = \frac{2}{J}\mathrm{dev}\left[\left(\frac{\partial\bar{\psi}}{\partial\bar{I}_1} + \bar{I}_1\frac{\partial\bar{\psi}}{\partial\bar{I}_2}\right)\bar{\boldsymbol{b}} - \frac{\partial\bar{\psi}}{\partial\bar{I}_2}\bar{\boldsymbol{b}}^2\right] + \frac{\partial\tilde{\psi}}{\partial J}\mathbf{1} \tag{2.24}$$

In the above equation 2.24, $\mathrm{dev}\,(\bullet)$ is the deviatoric projection tensor operator, $\mathrm{dev}\,(\bullet) = \bullet - 1/3\mathrm{tr}\,(\bullet) = \mathbb{P} : \bullet$, with $\mathbb{P}$ a fourth order deviatoric projection tensor, $\mathbb{P} = \mathbb{I} - \frac{1}{3}\mathbf{1}\otimes\mathbf{1}$. The strain energy density function $\bar{\psi}$ can take many forms and can span various levels of complexity to model the mechanical behaviour of a wide range of materials. A simple form of $\bar{\psi}$ is given by the neo-Hookean model, referring to the analogy with Hooke's law from equation 2.15.

$$\bar{\psi}_{NH}\left(\bar{I}_1\right) = \frac{\mu}{2}\left(\bar{I}_1 - 3\right) \tag{2.25}$$

The neo-Hookean hyperelastic material model is a specific case of the generalized polynomial form given by

$$\bar{\psi}_P\left(\bar{I}_1, \bar{I}_2\right) = \sum_{i+j=1}^{N} c_{i,j}\left(\bar{I}_1 - 3\right)^i\left(\bar{I}_2 - 3\right)^j \tag{2.26}$$

Another model dedicated to the behaviour of rubber-like materials is the model proposed by Arruda and Boyce et al. [5] that models a linked polymer network as interconnected chains with each chain displaying spring-like behaviour. This constitutive model will be used in chapter 6 to describe the elastic behaviour of high molecular weight

poly-L-lactic acid (PLLA). The strain energy density function has the following form:

$$\bar{\psi}(\lambda_r) = \mu N \left(\lambda_r \mathcal{L}^{-1}(\lambda_r) + \ln \left(\frac{\mathcal{L}^{-1}(\lambda_r)}{\sinh \mathcal{L}^{-1}(\lambda_r)} \right) \right) \tag{2.27}$$

Here, the material parameters μ and N represent the shear modulus and the chain rank. $\lambda_r = \lambda/\sqrt{N}$ is the relative stretch with λ the local stretch $\lambda = \bar{I}_1/3$. $\mathcal{L}(x) = \coth(x) - 1/x$ is the Langevin function.

2.3.3 Tangent moduli tensor

Implicit integration of finite element problems (see Section 2.6) requires an exact or approximate implementation of the stiffness tensor $\mathbb{C}$, often referred to as the tangent moduli tensor. Similarly to Equation 2.24, the stiffness moduli in the current configuration can be expressed by the fourth order tensor $\mathbb{C}$ as

$$\mathbb{C} = \frac{1}{J}\mathbb{P} : \left[\mathcal{P}\left(\bar{\mathbb{C}}\right) - \frac{2}{3}\left(\bar{\mathbf{F}}\,\bar{\boldsymbol{\tau}}\bar{\mathbf{F}}^T \otimes \mathbf{1} + \mathbf{1} \otimes \bar{\mathbf{F}}\,\bar{\boldsymbol{\tau}}\bar{\mathbf{F}}^T \right) + \mathcal{P}\left(\mathbb{H}_{\bar{\boldsymbol{\tau}}}\right) \right] : \mathbb{P} - s\mathbf{1}\otimes\mathbf{1} \tag{2.28}$$

with $\mathbb{P}$ the previously defined fourth order deviatoric projection tensor. The stiffness tensor in the reference configuration $\bar{\mathbb{C}}$ can be expressed as $\bar{\mathbb{C}} = 4\partial^2\bar{\psi}/\partial\bar{\mathbf{C}}\partial\bar{\mathbf{C}}$. The operator $\mathcal{P}$ denotes the push-forward projection to the current configuration so that

$$\left[\mathcal{P}(\bar{\mathbb{C}})\right]_{ijkl} = \bar{\mathbf{F}}_{ip}\bar{\mathbf{F}}_{jq}\bar{\mathbf{F}}_{kr}\bar{\mathbf{F}}_{ls}\bar{\mathbb{C}}_{pqrs} \tag{2.29}$$

The fourth order tensor $\mathbb{H}_{\bar{\boldsymbol{\tau}}}$ in eq.2.28 has components $\mathbb{H}_{\bar{\boldsymbol{\tau}}_{ijkl}} = (\delta_{ik}\bar{\tau}_{jl} + \bar{\tau}_{ik}\delta_{jl} + \delta_{il}\bar{\tau}_{jk} + \bar{\tau}_{il}\delta_{jk})/2$ and the volumetric term s can be derived as $s = -\partial\tilde{\psi}/\partial J - J\partial^2\bar{\psi}/\partial J^2$. The above equations, in combination with a proper definition of the energy function $\psi(\mathbf{F})$, fully define the mechanical behaviour of a hyperelastic material. Equation

2.28 can now be rewritten as follows

$$\begin{aligned}\mathbb{C} = \frac{1}{J}\mathbb{P} : \Bigg[4 \Bigg[& \left(\frac{\partial^2 \bar{\psi}}{\partial \bar{I}_1^2} + \frac{\partial \bar{\psi}}{\partial \bar{I}_2} + 2\bar{I}_1 \frac{\partial^2 \bar{\psi}}{\partial \bar{I}_1 \partial \bar{I}_2} + \bar{I}_1^2 \frac{\partial^2 \bar{\psi}}{\partial \bar{I}_2^2} \right) \bar{\mathbf{b}} \otimes \bar{\mathbf{b}} \\ & - \left(\frac{\partial^2 \bar{\psi}}{\partial \bar{I}_1 \partial \bar{I}_2} + \bar{I}_1 \frac{\partial^2 \bar{\psi}}{\partial \bar{I}_2^2} \right) \left(\bar{\mathbf{b}} \otimes \bar{\mathbf{b}}^2 + \bar{\mathbf{b}}^2 \otimes \bar{\mathbf{b}} \right) \\ & + \frac{\partial^2 \bar{\psi}}{\partial \bar{I}_2^2} \bar{\mathbf{b}}^2 \otimes \bar{\mathbf{b}}^2 - \frac{\partial \bar{\psi}}{\partial \bar{I}_2} \mathbb{H}_{\bar{\mathbf{b}}} \Bigg] \\ & - \frac{2}{3} \left(\bar{\mathbf{F}}\, \bar{\boldsymbol{\tau}} \bar{\mathbf{F}}^T \otimes \mathbf{1} + \mathbf{1} \otimes \bar{\mathbf{F}}\, \bar{\boldsymbol{\tau}} \bar{\mathbf{F}}^T \right) + \mathcal{P} \left(\mathbb{H}_{\bar{\boldsymbol{\tau}}} \right) \Bigg] : \mathbb{P} \\ & + \left(\frac{\partial \tilde{\psi}}{\partial J} + J \frac{\partial^2 \tilde{\psi}}{\partial J^2} \right) \mathbf{1} \otimes \mathbf{1}\end{aligned} \tag{2.30}$$

Here, the term $\mathbb{H}_{\bar{\mathbf{b}}}$ was defined as $\mathbb{H}_{\bar{\mathbf{b}}_{ijkl}} = (\bar{b}_{ik}\bar{b}_{jl} + \bar{b}_{il}\bar{b}_{jk})/2$.

2.3.4 Implementation of hyperelasticity

During this research, it was necessary to implement material constitutive equations within Fortran-coded material user subroutines (UMAT) to be used with the commercial implicit finite element solver Abaqus/standard (Simulia, Dassault Systèmes). In this way, constitutive material decriptions for elasticity could be coupled with viscoplastic material behaviour, and with a continuum damage degradation field. This requires both a definition of the Cauchy stress tensor and the stiffness tensor. The approach below describes how a hyperelastic material that depends only on the first invariant $\bar{I}_1$ can be implemented.

1. Compute the volume deformation $J = \det(\boldsymbol{F})$.
2. Set the volume-independent part of the deformation gradient as $\bar{\boldsymbol{F}} = J^{-1/3}\boldsymbol{F}$.
3. Construct the left Cauchy-Green stretch tensor $\bar{\boldsymbol{b}} = \bar{\boldsymbol{F}}\bar{\boldsymbol{F}}^T$.
4. Determine the first invariant of strain $\bar{I}_1$ by using Equations 2.22 and 2.23.
5. Evaluate the first and second order derivatives of the energy density function $\bar{\psi}$: $\partial\bar{\psi}/\partial\bar{I}_1$, $\partial^2\bar{\psi}/\partial\bar{I}_1^2$.

6. Determine the Kirchhoff stress tensor as $\bar{\boldsymbol{\tau}} = 2\partial\bar{\psi}/\partial\bar{I}_1\bar{\boldsymbol{b}}$.

7. The stiffness tensor $\bar{\mathbb{C}}$ can now be constructed using the following steps:

   a) Set $\tilde{\mathbb{C}} = 4J^{-4/3}\partial^2\bar{\psi}/\partial\bar{I}_1^2\bar{\boldsymbol{b}}\otimes\bar{\boldsymbol{b}} - \frac{2}{3}(\bar{\boldsymbol{\tau}}\otimes\mathbf{1} + \mathbf{1}\otimes\bar{\boldsymbol{\tau}})$.

   b) Add to $\tilde{\mathbb{C}}$ the fourth order tensor $\mathbb{H}_{\bar{\tau}}$ with components $\mathbb{H}_{\bar{\boldsymbol{\tau}}_{ijkl}} = \frac{1}{2}(\delta_{ik}\bar{\tau}_{jl} + \bar{\tau}_{ik}\delta_{jl} + \delta_{il}\bar{\tau}_{jk} + \bar{\tau}_{il}\delta_{jk})$, so that $\bar{\mathbb{C}} = \tilde{\mathbb{C}} + \mathbb{H}_{\bar{\tau}}$.

8. Construct the deviatoric part of the Kirchhoff stress
   $\tau_{dev} = \mathrm{dev}(\bar{\tau}) = \bar{\tau} - \frac{1}{3}\mathrm{tr}(\bar{\tau})$.

9. Construct the deviatoric part of the stiffness tensor $\bar{\mathbb{C}}$ as
   $\mathbb{C}_{dev} = \mathbb{P} : \bar{\mathbb{C}} : \mathbb{P}$.

10. Compute the Cauchy stress $\boldsymbol{\sigma}$ by adding the pressure terms.
    $\boldsymbol{\sigma} = \frac{1}{J}\tau_{dev} + \frac{\partial\psi_{vol}}{\partial J}\mathbf{1}$

11. Compute the consistent tangent moduli tensor $\mathbb{C}$ by adding the pressure terms to $\mathbb{C}_{dev}$.
    $\mathbb{C} = \frac{1}{J}\mathbb{C}_{dev} + \left(\frac{\partial\psi_{vol}}{\partial J} + J\frac{\partial^2\psi_{vol}}{\partial J^2}\right)\mathbf{1}\otimes\mathbf{1}$

2.3.5 Anisotropic hyperelasticity

As mentioned previously, the above described hyperelastic material models are isotropic and are therefore written in terms of invariants that are independent of the reference coordinate system. Many materials however display direction dependent stress-strain behaviour. This is e.g. the case for thermoplastic polymers that are formed via extrusions during which the polymer chains align according to a preferential direction, resulting in anisotropic material behaviour. Also many biological tissues display anisotropic mechanical properties due to cell alignment or the presence of re-enforcing fibres, e.g. collagen fibres. A commonly used anisotropic material model that captures the mechanical behaviour of arterial tissue has been introduced by Holzapfel et al. Here, the effect of helically aligned collagen fibres is captured via the introduction of a set of fibre structure tensors

$\boldsymbol{A}_f = \vec{\boldsymbol{a}}_f \otimes \vec{\boldsymbol{a}}_f$, where $\vec{\boldsymbol{a}}_f$ are the deformed preferential fibre directions. Equation 2.21 is then rewritten as

$$\psi(\boldsymbol{F}, \boldsymbol{A}_{f_1}, \boldsymbol{A}_{f_2}) = \bar{\psi}_{iso}(\bar{I}_1) + \bar{\psi}_{aniso}(\bar{I}_1, \bar{I}_{f_1}, \bar{I}_{f_2}) + \psi_{vol}(J) \quad (2.31)$$

with $\bar{I}_{f_i}$ the fibre invariants ($\bar{I}_{f_i} = \mathrm{tr}(\boldsymbol{A}_{f_i})$, $\vec{\boldsymbol{a}}_{f_i} = \bar{\boldsymbol{F}}\vec{\boldsymbol{a}}_{0,f_i}$ and $\vec{\boldsymbol{a}}_{0,f_i}$ the reference fibre orientation). For the model presented by Holzapfel et al. $\bar{\psi}_{iso}$ is implemented according to the neo-Hookean model (equation 2.25) and the expression of $\bar{\psi}_{aniso}$ takes the following form:

$$\bar{\psi}_{aniso}(\bar{I}_1, \bar{I}_{f_1}, \bar{I}_{f_2}) = \sum_{f_1, f_2} \frac{k_1}{2k_2} \left(\exp\left(k_2 \left(\kappa(\bar{I}_1 - 3)^2 + (1 - 3\kappa)(\bar{I}_4 - 1)^2\right)\right) - 1\right) \quad (2.32)$$

2.4 Plasticity

2.4.1 Isotropic J_2 plasticity

The above described linear elastic and hyperelastic materials undergo reversible deformations when subjected to external forces. This means that the material will return to its original shape when the forces are removed. Many (bio)materials also undergo irreversible or plastic deformations, i.e. the microscopic structure of the material permanently changes if an internal force threshold is exceeded. For metals, this is usually a rearrangement of the crystal lattice structure. For polymers, the molecular chains undergo relative shearing when subjected to plastic deformation. The principle of permanent deformation is exploited for balloon expandable stents, who's struts are designed to act as plastic hinges. This type of stents contains zones (often referred to as the crowns of the stent) that undergo plastic deformations upon balloon expansion. When fully expanded, these local plastic deformations ensure that the stent is able to maintain a sufficiently large diameter when the balloon pressure is released. The plastic hinge mechanism is illustrated in Figure 2.3. Also balloon expandable metallic biocorrodible stents and polymeric absorbable stents make use of the plastic hinge principle.

The degradation-independent material response of the metallic corrodible stents described in this thesis is modelled using the classical

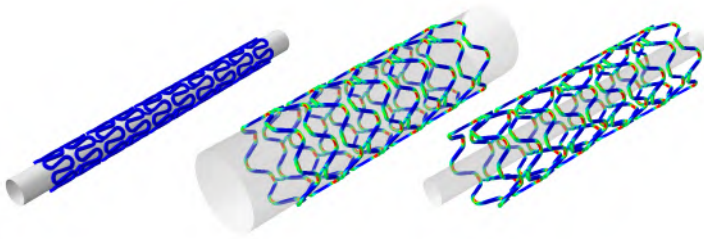

Figure 2.3: Computer simulation showing free expansion of a balloon expandable stent. Shown are the stent's initial crimped geometry, the stent at maximal expansion (i.e. at maximal balloon pressure) and the stent's final geometry. The balloon is modelled as a cylindrical surface. The colors plot the equivalent plastic strain, where red indicates zones of large plastic deformation and blue indicates no plastic deformation. Permanent plastic set is located in the crowns of the stent, which act as plastic hinges.

isotropic J_2-plasticity approach. To explain J_2-plasticity, let us first rewrite Equation 2.16 in its rate form.

$$\overset{\triangledown}{\boldsymbol{\sigma}} = \mathbb{C} : \boldsymbol{D} \tag{2.33}$$

Here, $\overset{\triangledown}{\boldsymbol{\sigma}}$ is an objective description of the rate of change of the stress tensor and $\boldsymbol{D}$ is the strain rate defined in Equation 2.8. A common assumption is to decompose the rate of deformation $\boldsymbol{D}$ additively into a reversible elastic part $\boldsymbol{D}^e$ and an irreversible plastic part $\boldsymbol{D}^p$.

$$\boldsymbol{D} = \boldsymbol{D}^e + \boldsymbol{D}^p \tag{2.34}$$

The rate form of Hooke's law written in Equation 2.33 can thus be expressed as follows.

$$\overset{\triangledown}{\boldsymbol{\sigma}} = \mathbb{C} : (\boldsymbol{D} - \boldsymbol{D}^p) \tag{2.35}$$

To model plasticity, we assume the existence of a so-called *yield function* f_y. For a J_2-Von Mises material, this yield function takes the following shape.

$$f_y(\boldsymbol{\sigma}, \sigma_y) = \tilde{\sigma} - \sigma_y \tag{2.36}$$

Here, σ_y is the current yield stress and $\tilde{\sigma}$ is the equivalent Von Mises stress as defined in Equation 2.14. Stresses are constrained to

stay within the elastic domain $f_y \leq 0$. Plastic deformation occurs when $f_y(\boldsymbol{\sigma}, \sigma_y) = 0$, and the plastic strain rate takes the following form.

$$\boldsymbol{D}^p = \Lambda \boldsymbol{N} \ , \ \boldsymbol{N} = \frac{\boldsymbol{S}}{\sqrt{\boldsymbol{S} : \boldsymbol{S}}} = \sqrt{\frac{3}{2}} \frac{\boldsymbol{S}}{\tilde{\sigma}} \tag{2.37}$$

The tensor $\boldsymbol{N}$ can be seen as the outward normal to the yield surface. Λ is a positive scalar called the consistency parameter which can be determined by solving the *consistency condition*

$$\dot{f}_y(\boldsymbol{\sigma}, \sigma_y) = 0 \tag{2.38}$$

Inside the elastic domain, $f_y < 0$ and $\Lambda = 0$ so that f_y and Λ can be obtained via the so-called *Kuhn-Tucker* loading and unloading conditions.

$$f_y \Lambda = 0 \ , \ \Lambda \geq 0 \ , \ f_y \leq 0 \tag{2.39}$$

The rate of change of the yield stress is given by the isotropic hardening law.

$$\dot{\sigma}_y = \sqrt{\frac{2}{3}} h \Lambda \tag{2.40}$$

where h is a hardening parameter referred to as the plastic modulus. If we define an equivalent measure for the effective plastic strain as $\dot{\bar{\varepsilon}}_p = \sqrt{\frac{2}{3} \boldsymbol{D}_p : \boldsymbol{D}_p}$, and by using $\Lambda^2 = \boldsymbol{D}_p : \boldsymbol{D}_p$ obtained from Equation 2.37, we can also write Equation 2.40 as

$$\dot{\sigma}_y = h \dot{\bar{\varepsilon}}_p \tag{2.41}$$

2.4.2 Viscoplasticity

Many materials – including polymeric materials for bioabsorbable stents – undergo *visco*plastic deformation, i.e. the effective Von Mises stress is no longer constrained to be lower than or equal to the yield stress, but can take values $\tilde{\sigma} \geq \sigma_y^{vp}$, where σ_y^{vp} symbolizes a vicoplastic yield stress. This results in an overstress $\Delta\bar{\sigma}$.

$$\Delta\bar{\sigma} = \left\langle \tilde{\sigma} - \sigma_y^{vp} \right\rangle \tag{2.42}$$

Here, the operator $\langle \bullet \rangle$ stands for $\langle \bullet \rangle = \frac{1}{2}(\bullet + |\bullet|)$. Plasticity occurs when $\Delta\bar{\sigma}$ is positive. To incorporate viscosity into the plasticity hardening laws, we used the following formulation, given by Ponthot in [78].

$$\Lambda = \sqrt{\frac{3}{2}} \left\langle \frac{\tilde{\sigma} - \sigma_y^{vp}}{\eta \bar{\varepsilon}_p} \right\rangle \tag{2.43}$$

Here, we introduced η as a viscosity parameter. This results in the hereunder written yield constraint, similar to the constraint defined in Equation 2.36.

$$\bar{f}_y = \tilde{\sigma} - \sigma_y^{vp} - \eta \bar{\varepsilon} \dot{\bar{\varepsilon}}_p = 0 \tag{2.44}$$

2.4.3 Corotational frame

To ensure incremental objectivity when integrating rate dependent plasticity constitutive equations, a common approach is to rewrite these equations in a so-called corotational frame. Such a moving corotational frame can be obtained in the following manner. For any skew-symmetric tensor $\boldsymbol{\omega}$ (i.e. $\boldsymbol{\omega}^T = -\boldsymbol{\omega}$) a set of rotation tensors can be generated that fulfil the requirements

$$\begin{cases} \dot{\boldsymbol{\rho}} = \boldsymbol{\omega}\boldsymbol{\rho} \\ \boldsymbol{\rho}|_{t=t_0} = \mathbf{1} \end{cases} \tag{2.45}$$

We can now use the rotation tensors $\boldsymbol{\rho}$ to express the components of the Cauchy stress tensor $\boldsymbol{\sigma}$ in a frame that has been rotated with respect to the reference Cartesian coordinate system. In the rotated coordinate system, the corotational Cauchy stress $\boldsymbol{\sigma}^{CR}$ is

$$\boldsymbol{\sigma}^{CR} = \boldsymbol{\rho}^T \boldsymbol{\sigma} \boldsymbol{\rho} \tag{2.46}$$

When written in rate form, i.e. upon time differentiation, and by using Equation 2.45, the above expression can be transformed into

$$\dot{\boldsymbol{\sigma}}^{CR} = \boldsymbol{\rho}^T \left(-\boldsymbol{\omega}\boldsymbol{\sigma} + \dot{\boldsymbol{\sigma}} + \boldsymbol{\sigma}\boldsymbol{\omega} \right) \boldsymbol{\rho} = \boldsymbol{\rho}^T \overset{\triangledown}{\boldsymbol{\sigma}}{}^{CR} \boldsymbol{\rho} \tag{2.47}$$

Here, $\overset{\triangledown}{\boldsymbol{\sigma}}{}^{CR}$ is an objective corotational stress rate. If we use the spin tensor $\boldsymbol{W}$ defined in Equation 2.8 for $\boldsymbol{\omega}$, $\overset{\triangledown}{\boldsymbol{\sigma}}{}^{CR}$ is also called the *Jaumann rate*. Another skew-symmetric tensor can be constructed as $\dot{\boldsymbol{R}}\boldsymbol{R}^T$ with $\boldsymbol{R}$ the rotation tensor resulting from polar decomposition of the deformation gradient $\boldsymbol{F}$ (Equation 2.2). In the latter case, with $\boldsymbol{\omega} = \dot{\boldsymbol{R}}\boldsymbol{R}^T$, $\overset{\triangledown}{\boldsymbol{\sigma}}{}^{CR}$ is referred to as the *Green-Naghdi* rate.

2.4.4 Integration of viscoplasticity

Using the constitutive equations defined in 2.4.2 and the corotational formulations from 2.4.3, the below listed approach described in [78] was followed to integrate viscoplasticity. This algorithm is compatible for implementation within material subroutines that can be used with the implicit finite element solver Abaqus/standard, which requires definition of the Cauchy stresses $\boldsymbol{\sigma}$ and the stiffness tensor $\mathbb{C}$.

1. Compute the deformation gradient increment $\Delta\boldsymbol{F}$, the rotation increment $\Delta\boldsymbol{R}$, the incremental Cauchy-Green strain $\Delta\boldsymbol{C}$ and the logarithmic strain increment $\Delta\boldsymbol{\varepsilon}_{log}$.

   $\Delta\boldsymbol{F} = \boldsymbol{F}|_{t=t_1}\boldsymbol{F}|^{-1}_{t=t_0}$ $\Delta\boldsymbol{C} = \Delta\boldsymbol{F}^T\Delta\boldsymbol{F}$

   Principal value decomposition gives:

   $\Delta\boldsymbol{C} = \sum_{p=1}^{3} c_p\vec{\boldsymbol{n}}_p \otimes \vec{\boldsymbol{n}}_p$

   $\Delta\boldsymbol{\varepsilon}_{log} = \frac{1}{2}\sum_{p=1}^{3} \ln(c_p)\vec{\boldsymbol{n}}_p \otimes \vec{\boldsymbol{n}}_p$

   $\Delta\boldsymbol{R} = \sum_{p=1}^{3} \sqrt{c_p}\vec{\boldsymbol{m}}_p \otimes \vec{\boldsymbol{n}}_p$

   with

   $\vec{\boldsymbol{m}}_p = \Delta\boldsymbol{F}\vec{\boldsymbol{n}}_p \;\;,\;\; p = 1,2,3$

2. Compute the trial stress $\boldsymbol{\sigma}_{tr}$ and rotate forward. Also compute the deviatoric trial stress and the equivalent Von Mises stress.

   $\boldsymbol{\sigma}_{tr} = \Delta\boldsymbol{R}\,(\boldsymbol{\sigma}|_{t=t_0} + \mathbb{C} : \Delta\boldsymbol{\varepsilon}_{log})\,\Delta\boldsymbol{R}^T$

   $\boldsymbol{S}_{tr} = \mathrm{dev}\,(\boldsymbol{\sigma}_{tr})$

   $\tilde{\sigma} = \sqrt{\frac{2}{3}\boldsymbol{S}_{tr} : \boldsymbol{S}_{tr}}$

3. Check whether the trial Von Mises stress exceeds the current viscoplastic yield stress. If so, update the yield stress σ_y^{vp}, update the viscoplastic strain ε_p, update the Cauchy stress tensor end the elastic tangent moduli tensor.

   if $\tilde{\sigma} > \sigma_y^{vp}|_{t=t_0}$ **then**

   $\Delta\varepsilon_p = \frac{\tilde{\sigma} - \sigma_y^{vp}|_{t=t_0}}{3\mu + h + \eta/\Delta t}$

   $\sigma_y^{vp}|_{t=t_1} = \sigma_y^{vp}|_{t=t_0} + h\Delta\varepsilon_p$

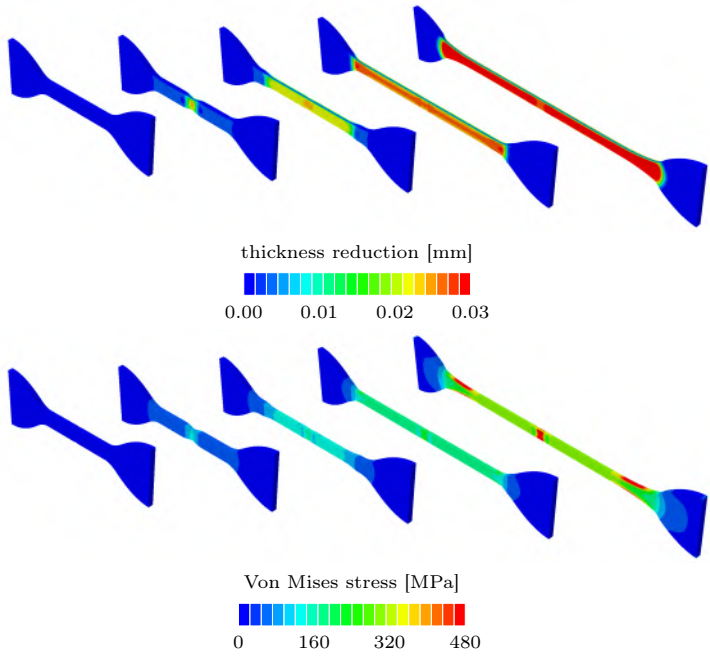

Figure 2.4: Computer simulation showing the deformation of a dumbbell-shaped tensile testing specimen under longitudinal extension. The material used for the simulations was modelled as a hyperelastic spring in parallel with a viscoplastic dashpot, by making use of the constitutive equations described in sections 2.3.4 and 2.4.2. The upper series of tensile test specimens show the reduction in specimen thickness as the magnitude of the displacement of the nodes of the FE-model in the direction perpendicular to the plane of the dumbbell. The lower series of specimens plot the values of the Von Mises stress. We can clearly see the formation of a plastic neck at the centre of the specimen, which progresses outward to the clamped ends of the specimens when further stretched. This necking behaviour is typical for plastic polymers.

$$\varepsilon_p|_{t=t_1} = \varepsilon_p|_{t=t_0} + \Delta\varepsilon_p$$

Update stresses:

$$\boldsymbol{\sigma}|_{t=t_1} = \boldsymbol{\sigma}|_{t=t_0} - \frac{3\mu\Delta\varepsilon_p}{\tilde{\sigma}}\boldsymbol{S}_{tr}$$

Update the consistent elastic tangent moduli tensor:

$$\bar{\mathbb{C}} = \kappa\mathbf{1}\otimes\mathbf{1} + 2\tilde{\mu}\left(\mathbb{I} - \tfrac{1}{3}\mathbf{1}\otimes\mathbf{1}\right) - 3\tfrac{\tilde{\mu}\gamma}{\tilde{\sigma}^2}\boldsymbol{S}_{tr}\otimes\boldsymbol{S}_{tr}$$

With $\tilde{\mu}$ and γ defined as

$$\tilde{\mu} = \beta\mu \quad , \quad \beta = \frac{\boldsymbol{\sigma}|_{t=t_1} + \Delta\varepsilon_p \eta/\Delta t}{\tilde{\sigma}}$$

$$\gamma = \frac{3\tilde{\mu} + (\beta - 1)\tilde{h}}{3\tilde{\mu} + \beta\tilde{h}} \quad , \quad \tilde{h} = h + \frac{\eta}{\Delta t}$$

end if

4. Store the plastic strain $\varepsilon_p|_{t=t_1}$ and the viscoplastic yield stress $\sigma_y^{vp}|_{t=t_1}$.

A hyperelastic-viscoplastic material can be defined as a hyperelastic network parallel to a elasto-viscoplastic damper. A similar material model will be used later in this thesis to define the mechanical behaviour of the bioresorbable material polylactic acid (PLLA). The implementation of such a model consist in defining the hyperelastic stresses $\boldsymbol{\sigma}_h$ and the tangent moduli $\mathbb{C}_h$, e.g. by using the scheme listed in section 2.3.4, and adding them to the elasto-viscoplastic stresses $\boldsymbol{\sigma}_{vp}$ and the corresponding tangent moduli $\mathbb{C}_{vp}$.

$$\boldsymbol{\sigma} = \boldsymbol{\sigma}_h + \boldsymbol{\sigma}_{vp} \quad , \quad \mathbb{C} = \mathbb{C}_h + \mathbb{C}_{vp} \tag{2.48}$$

The result of such a hyperelastic-viscoplastic material model implementation for use with a finite element solver is shown in Figure 2.4, where the plastic deformation of a dumbbell-shaped tensile testing specimen is simulated.

2.5 Force equilibrium and virtual work

During a time interval $t \in [0, t_1] \subset \mathbb{R}^+$, the body $\mathscr{B}$ is subjected to a loading history, including deformations, body forces, thermal loading, friction etc. , causing the build-up of internal stress in the current configuration $\mathcal{B}_t$. Now imagine an arbitrary volume V around the material point $\boldsymbol{p}$ enclosed by the boundary surface ∂V as illustrated in figure 2.5. A set of body forces $\vec{\boldsymbol{f}}$ are acting on this arbitrary volume V while traction forces $\vec{\boldsymbol{t}}$ interact with the surface ∂V. If $\mathscr{B}$ is in a *static state of equilibrium* at t, all forces acting on V and ∂V must add up to zero.

$$\int_V \vec{\boldsymbol{f}} dV + \int_{\partial V} \vec{\boldsymbol{t}} d\partial V = \vec{\mathbf{0}} \tag{2.49}$$

Using the definition of stress 2.10 and Gauss' theorem, equation 2.49 can be rewritten as

$$\int_V \vec{\boldsymbol{f}} dV + \int_{\partial V} \vec{\boldsymbol{n}}.\boldsymbol{\sigma} d\partial V \overset{Gauss}{=} \int_V \left(\vec{\boldsymbol{f}} + \vec{\nabla}.\boldsymbol{\sigma} \right) dV = \vec{\mathbf{0}} \tag{2.50}$$

Given the previously mentioned condition that the above must be valid for any arbitrary volume V, we obtain the so-called *strong formulation* of static force equilibrium inside a solid body $\mathscr{B}$.

$$\overset{\forall V}{\Longrightarrow} \; \vec{\boldsymbol{f}} + \vec{\nabla}.\boldsymbol{\sigma} = \vec{\mathbf{0}} \tag{2.51}$$

This differential equation provides the exact solution to force equilibrium for the continuum state of the solid body $\mathcal{B}$, provided that the definitions of body forces $\vec{\boldsymbol{f}}$, traction forces $\vec{\boldsymbol{t}}$, stresses $\boldsymbol{\sigma}$, volume and area are precise and complete. For practical engineering problems, we will try to find an approximated and interpolated solution to these equilibrium equations at a discrete set of points in 3D space. The first step in going to such a *finite element* approximation is to modify the equilibrium vector equation 2.51 to an equivalent 'weak' form, a single

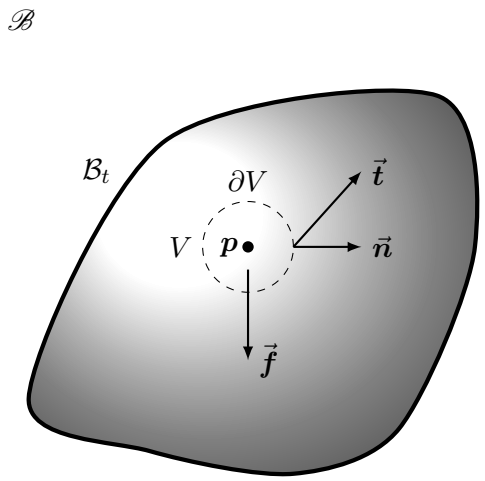

Figure 2.5: Force equilibrium inside a solid body $\mathscr{B}$ with current configuration $\mathcal{B}_t$. Body forces $\vec{\boldsymbol{f}}$ and traction forces $\vec{\boldsymbol{t}}$ are acting upon an arbitrary volume V and its boundary surface ∂V around the material point $\boldsymbol{p}$. The surface ∂V is characterized by its unit normal vectors $\vec{\boldsymbol{n}}$.

scalar equation that is obtained via vector multiplication of 2.51 with an arbitrary test function $\delta\vec{\boldsymbol{v}}$ and integrating over the volume V.

$$\int_V \left(\vec{\boldsymbol{f}} + \vec{\nabla}.\boldsymbol{\sigma}\right).\delta\vec{\boldsymbol{v}}dV = 0 \tag{2.52}$$

We call the above equation the *weak formulation* of static force equilibrium. The test function $\delta\vec{\boldsymbol{v}}$ can be interpreted as a virtual velocity field so that the equilibrium equation 2.52 indicates that the total virtual work done over the volume V must be zero. The work rate balance of equation 2.52 can be rewritten as follows by subsequently using the chain rule and Gauss' theorem.

$$\int_V \left(\vec{\boldsymbol{f}}.\delta\vec{\boldsymbol{v}} + \vec{\nabla}.\left(\boldsymbol{\sigma}.\delta\vec{\boldsymbol{v}}\right) - \boldsymbol{\sigma} : \nabla\delta\vec{\boldsymbol{v}}\right) dV = 0 \tag{2.53}$$

$$\int_{\partial V} \vec{\boldsymbol{n}}.\boldsymbol{\sigma}.\delta\vec{\boldsymbol{v}}d\partial V + \int_V \left(\vec{\boldsymbol{f}}.\delta\vec{\boldsymbol{v}} - \boldsymbol{\sigma} : \nabla\delta\vec{\boldsymbol{v}}\right) dV = 0 \tag{2.54}$$

The term $\nabla\delta\vec{\boldsymbol{v}}$ can be read as a virtual velocity gradient $\delta\boldsymbol{L}$, similar to the velocity gradient $\boldsymbol{L}$ as in definition 2.7. Analogous to 2.8, $\delta\boldsymbol{L}$ can be split into a virtual deformation rate $\delta\boldsymbol{D}$ and a virtual spin tensor $\delta\boldsymbol{W}$. Due to the symmetry of $\boldsymbol{\sigma}$ it follows that $\boldsymbol{\sigma} : \delta\boldsymbol{W} = 0$ so that finally we obtain the following expression for the weak formulation of the force equilibrium inside a continuum body:

$$\underbrace{\int_{\partial V} \vec{\boldsymbol{t}}.\delta\vec{\boldsymbol{v}}d\partial V + \int_V \vec{\boldsymbol{f}}.\delta\vec{\boldsymbol{v}}dV}_{\text{external}} = \underbrace{\int_V \boldsymbol{\sigma} : \delta\boldsymbol{D}dV}_{\text{internal}} \tag{2.55}$$

The left hand side of equation 2.55 represents the rate of work done by the external body forces $\vec{\boldsymbol{f}}$ and traction forces $\vec{\boldsymbol{t}}$ subjected to any virtual velocity field $\delta\vec{\boldsymbol{v}}$, and must equal the right hand side of the equation representing the rate of work done by the stresses on the rate of deformation $\delta\boldsymbol{D}$ of the same velocity field. This principle of virtual work is the basic equilibrium statement for the *finite element* formulation used in solid mechanics problems. The advantage of this weak formulation over the strong form of equation 2.51 is that by integrating over the volume of the solid body, we are able to introduce test functions $\delta\vec{\boldsymbol{v}}_n$ that are not entirely arbitrary but that vary at a discrete and finite number of nodal values.

2.6 The finite element method

The finite element approximate solution for a static solid mechanics problem starts from the virtual work equilibrium of equation 2.55, with the components of the internal work volume integrand projected to the reference configuration $\mathscr{B}_0$.

$$\int_{V_0} \boldsymbol{\tau}_c : \delta\boldsymbol{\varepsilon} dV_0 = \int_{\partial V} \vec{\boldsymbol{t}}.\delta\vec{\boldsymbol{v}} d\partial V + \int_V \vec{\boldsymbol{f}}.\delta\vec{\boldsymbol{v}} dV \tag{2.56}$$

The *finite element method* (FEM) approximates the volume V_0 by a discrete number of cells with usually simple geometrical shapes (tetrahedrons, cuboids, etc) called *elements*, of which the vertices, i.e. the *nodes* form the equilibrium integration points. The nodal variables u^N are interconnected by the element interpolation functions or *shape functions* $\boldsymbol{N}_N$ so that in general, the variable $\boldsymbol{u}$ will be interpolated as:

$$\boldsymbol{u} = \boldsymbol{N}_N u^N \tag{2.57}$$

We apply the interpolator to the virtual velocity field, $\delta\boldsymbol{v} = \boldsymbol{N}_N \delta v^N$ and to the virtual strain field $\delta\boldsymbol{\varepsilon} = \boldsymbol{\beta}_N \delta v^N$, where $\boldsymbol{\beta}_N$ is an interpolation matrix that in general also depends on the current position, $\boldsymbol{\beta}_N = \boldsymbol{\beta}_N(\boldsymbol{x}, \boldsymbol{N}_N)$. This allows us to approximate the static equilibrium equation as

$$\delta v^N \int_{V_0} \boldsymbol{\beta}_N : \boldsymbol{\tau}_c dV_0 = \delta v^N \left(\int_{\partial V} \boldsymbol{N}_N^T.\boldsymbol{t} d\partial V + \int_V \boldsymbol{N}_N^T.\boldsymbol{f} dV \right) \tag{2.58}$$

By choosing each individual δv^N non-zero and all other variables $\delta v^{M \neq N}$ zero, we arrive to the following (in general non-linear) set of equations.

$$\int_{V_0} \boldsymbol{\beta}_N : \boldsymbol{\tau}_c dV_0 = \int_{\partial V} \boldsymbol{N}_N^T.\boldsymbol{t} d\partial V + \int_V \boldsymbol{N}_N^T.\boldsymbol{f} dV \tag{2.59}$$

Equation 2.59 can be symbolically summarized into the following general expression for a static displacement finite element analysis.

$$F^N(u^M) = 0 \tag{2.60}$$

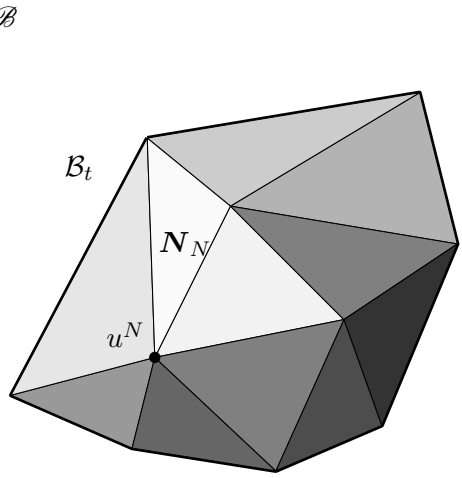

Figure 2.6: Finite element approximation of the solid body $\mathcal{B}$. The volume is subdivided into a discrete number of simple geometrical shapes, called the elements. The element shape functions $\boldsymbol{N}_N$ couple the nodal variables u^N.

For a dynamic finite element problem the inertial forces $M^{NM}\ddot{u}^M$ have to be added to the system equations, where M^{NM} is a mass interpolation matrix.

$$F^N(u^M) + M^{NM}\ddot{u}^M = 0 \tag{2.61}$$

Usually, an iterative computational approach is followed to solve this often very large system of equations and several commercial and open-source FEM-software packages are available for this purpose. In this research, the commercial finite element solver Abaqus (Dassault Systèmes) was used.

2.7 Explicit and implicit integration of the finite element problem

The finite element (FE) solver used during this research was Abaqus (Dassault Systèmes), which provides an explicit (Abaqus/explicit) and implicit (Abaqus /standard) solution technique to solve the set of equations that defines the FE-problem. The discretized dynamic finite element problem has the following shape, as in equation 2.61.

$$F^N(u^M) + M^{NM}\ddot{u}^M = I^N(u^M) - E^N(u^M) + M^{NM}\ddot{u}^M = 0 \tag{2.62}$$

$I^N(u^M)$, $E^N(u^M)$ and $M^{NM}\ddot{u}^M$ are the internal force vector (caused by internal stress), the external force vector and the force vector due to inertia (often referred to as the d'Alembert forces) of which the integrand expressions are given in equation 2.59. In a *static* finite element problem, the contribution of inertial forces is negligible, $M^{NM}\ddot{u}^M = 0$. A finite element problem is called *dynamic* if $M^{NM}\ddot{u}^M \neq 0$. A (in general non-linear) static FE-problem $F^N(u^M) = 0$ is preferably solved via an implicit solution technique. To do so, the solution of the current mechanical state can be obtained via iterative solution of the equilibrium equations. Abaqus/standard uses Newton's method to implicitly solve a static FE-problem. For a given estimate of the incremental solution Δu_i at iteration i, the equilibrium equations can be rewritten using Taylor-series expansion as

$$F^N(\Delta u^M) = F^N(\Delta u_i^M) + \frac{\partial F^N}{\partial \Delta u^M}(\Delta u_i^M)\left(\Delta u^M - \Delta u_i^M\right) + \cdots = 0 \tag{2.63}$$

The first two terms of the Taylor-expansion form a linear set of equations that is used to update the correction term $c_{i+1}^M = \Delta u_{i+1}^M - \Delta u_i^M$ for every iteration.

$$F_i^N + K_i^{NM} c_{i+1}^M = 0 \;\rightarrow\; c_{i+1}^M = -(K_i^{NM})^{-1} F_i^N \tag{2.64}$$

In Abaqus/standard, every iteration is repeated until convergence is achieved, i.e. displacement corrections c_i^M have to be sufficiently small compared to the incremental displacements Δu_i^M, contact conditions have to satisfy, and force and moment equilibrium have to be obtained, and this for every node of the FE-model. Abaqus tries to find a solution for a given increment Δu^k and will step to a new Δu^{k+1} increment if a solution was obtained. The size of the newly chosen increment is increased if convergence was fast in the previous increment or decreased if convergence was slow. If no solution could be obtained for Δu^k within a reasonable amount of iterations, the size of Δu^k will be reduced and a new attempt will be undertaken. For many static problems Abaqus/standard will be able to find a solution for a small number of increments and is therefore very efficient for static FE-problems. However, for highly non-linear problems such as models involving complex contact conditions, the amount of increments and the number of iterations per increment might become large and an explicit solution technique might become preferable.

An explicit solution for structural FE-problems starts from the dynamic equilibrium $F^N(u^M) + M^{NM}\ddot{u}^M = 0$. The solution at a time increment $t + \Delta t$ is simply obtained through extrapolation of the state at a the previous time increment t. Suppose we obtained a solution for the state at time increment t, which allows us to solve for the nodal accelerations at time t:

$$M^{NM}\ddot{u}^M\big|_t = -\,F^N\big|_t \;\rightarrow\; \ddot{u}^M\big|_t = -\left(M^{NM}\right)^{-1} F^N\big|_t \tag{2.65}$$

The velocities $\dot{u}$ and displacements u can be updated using central difference integration.

$$\dot{u}^M\big|_{t+\frac{\Delta t}{2}} = \dot{u}^M\big|_{t-\frac{\Delta t}{2}} + \left(\frac{\Delta t|_{t+\Delta t} + \Delta t|_t}{2}\right)\ddot{u}^M\big|_t \tag{2.66}$$

$$u^M\big|_{t+\Delta t} = u^M\big|_t + \Delta t|_{t+\Delta t}\,\dot{u}^M\big|_{t+\frac{\Delta t}{2}} \tag{2.67}$$

The explicit integration scheme is stable for time increments Δt smaller than a certain threshold value Δt_{stable}.

$$\Delta t_{stable} = \min\left(\frac{L_e}{c_d}\right) \tag{2.68}$$

Here, L_e and c_s are the characteristic element length and the dilatational wave speed, a material characteristic which e.g. for a linear elastic material can be defined as $c_d = \sqrt{(\lambda + 2\mu)/\rho}$ with λ and μ the Lamé constants and ρ the material density. For an explicit solution technique, simulation times will increase for increasing values of total step time t_{step} of the problem and of the material stiffness K_{mat}, and for decreasing values of the material density ρ_{mat} and the smallest element sizes L_e.

$$t_{step}\uparrow, K_{mat}\uparrow, \rho_{mat}\downarrow, L_e\downarrow \;\rightarrow\; \text{simulation time}\uparrow \tag{2.69}$$

For quasi-static problems, i.e. if contributions of $M^{NM}\ddot{u}^M$ are small, the dilational wave speed c_d becomes small which results in relatively long simulation times. Therefore an implicit solution technique is generally prefered for this kind of FE-problem. However,

the individual time steps do not require iteration and therefore require little computer memory, so that for large models with complex non-linear characteristics an explicit solution could become preferable over an implicit solution technique. Stent degradation is basically a dynamic problem but the degradation times are very long compared to the inertial effects time scale and therefore it is quasi-static. To correctly capture local degradation effects, very small element sizes have to be used which also increases simulation time. Therefore, an implicit solution technique might prove more efficient for these simulations. Previous studies have however all used an explicit solution technique, because of complex contact interaction, the integration of the degradation laws and the necessity to delete elements after complete degradation. However, this research aimed at using implicit integration as much as possible for the sake of computation times and the better reliability of stress output.

2.8 Modelling degradation with continuum damage mechanics

To capture the transitional mechanical behaviour of the biodegradable stents studied in this work, we made use of continuum damage theory. Continuum damage theory allows to account for the effects of e.g. polymer degradation or metal corrosion on the structural integrity of the material without resorting to an explicit description of the microscopic phenomena and their progression. It is therefore a phenomenological approach rather than a physical description. Continuum damage is – apart from degradation – also often used to model fatigue induced damage in metal or fracture mechanics. The effects of progressing damage upon the material mechanics are represented by means of one or more arbitrary state variables that depend on material point position (close to the surface or at the bulk), time, concentration of corrosive agents, local stress levels, deformation. Lemaitre and Desmorat [59] [58] originally proposed the following relation between a scalar damage field d, the true stress $\boldsymbol{\sigma}$ and an effective stress $\tilde{\boldsymbol{\sigma}}$:

$$\tilde{\boldsymbol{\sigma}} = \frac{\boldsymbol{\sigma}}{1-d} \tag{2.70}$$

The relation between true and effective stress and the progressing degradation field can be understood as illustrated in figure 2.7. A solid bar subjected to a tensile load has a stress value $\boldsymbol{\sigma}$, which is the load divided by the cross section area A_0. If, because of degradation, this cross section area reduces to A_d, the effective stress $\tilde{\boldsymbol{\sigma}}$ in that area

will be the load divided by A_d. The degradation parameter d from equation 2.70 thus resembles $1-A_d/A_0$, the relative reduction of cross section area. The degradation or damage field d has values between 0 (non-degraded) and 1 (fully degraded). In practice, each element of the finite element mesh is assigned with a varying value of d and once fully degraded ($d = 1$), the element is removed from the mesh. For erosion, corrosion or surface degradation in general, only elements at the surface of the mesh are subjected to degradation. When elements are deleted, a new surface has to be assigned.

For materials that follow Hooke's law 2.15, the true stress can be derived as the degradation field multiplied with the contraction of the stiffness matrix and the strain tensor.

$$\boldsymbol{\sigma} = (1 - d)\mathbb{C} : \boldsymbol{\varepsilon} \tag{2.71}$$

For such materials it can be convenient for implementation purposes to express degradation as directly influencing the material properties, e.g. $E_d = (1-d)E_0$ with respect to the degraded elastic modulus E_d and the initial elastic modulus E_0. For hyperelastic materials, degradation can be directly expressed by relating a degraded energy function ψ_d with the non-degraded strain energy function ψ_0 [83].

$$\psi_d = (1 - d)\psi_0 \tag{2.72}$$

In fracture mechanics, d is often directional and written as a tensor field D. Within the context of material degradation or erosion however, the degradation parameter d is a scalar field.

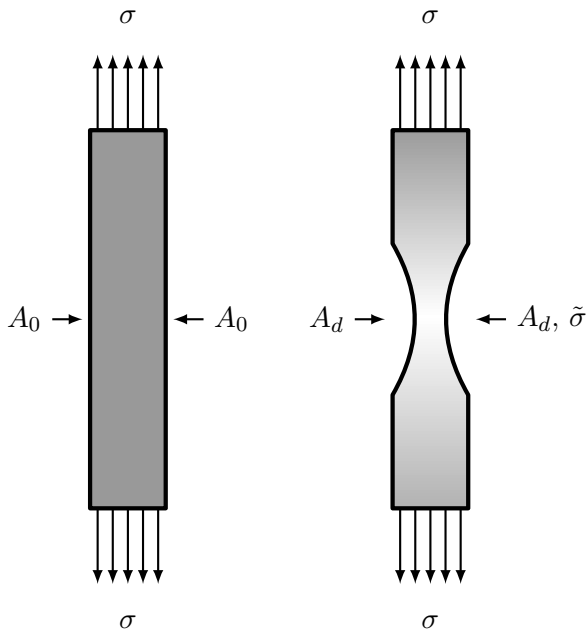

Figure 2.7: Illustration of the continuum damage approach. A solid bar is subjected to a tensile load and has a stress value $\boldsymbol{\sigma}$, which is the load divided by the cross section area A_0. Because of degradation the cross section area reduces to A_d. The effective stress $\tilde{\boldsymbol{\sigma}}$ in that area will be the load divided by A_d. The degradation field d is the relative reduction of cross section area $d = 1 - A_d/A_0$ and has values between 0 (non-degraded) and 1 (fully degraded). The true and effective stress then relate as $\tilde{\boldsymbol{\sigma}} = \frac{\boldsymbol{\sigma}}{1-d}$.

Chapter 3

Finite element modelling of biodegradable stents

Mathematical and computational modelling in general and finite element analysis (FEA) in particular have proven to be valuable and time efficient tools to characterize the short term and long term mechanical performance of biomedical implantable devices such as stents. These virtual bench tests can provide informational support throughout the entire product development chain – FEA can be used to assess the feasibility of new product ideas, it can optimize geometries and overall device characteristics of existing designs and it can be used as a planning tool for clinical trials. Many studies have shown the applicability of FEA to investigate the mechanical behaviour of stents [9, 48, 61, 64]. By combing validated models for a particular device with patient specific images it can be used in planning surgical procedures and to classify specific devices for different kinds of atherosclerotic lesions [8, 49, 63]. When combined with computational fluid mechanics, the finite element method is able to reveal insight into aspects of drug elution and coating biodegradation [15, 20, 57]. Analysing the mechanical behaviour of biodegradable stents via finite element simulations however poses new challenges due to the complexity of the stent materials which display transitional mechanics both in the long term range (polymer degradation, metal corrosion) and the short term range (viscoplasticity in case of polymeric stents). A limited number of FEA-studies on biodegradable stents has

been performed. With respect to polymeric scaffolds, Soares et al. proposed a continuum degradation model which includes the effect of deformation upon the degradation rate of poly-L-lactic acid (PLLA) and applied it to biodegradable stents [90]. Bokov et al. investigated the interaction of a biodegradable polymeric stent with the vascular wall using FEA [12]. Our group has studied the effect of the deployment rate on the mechanical integrity of a PLLA stent via FEA [22]. Several computational methods have been proposed to physically model surface degradation of corrodible metals and of biocorrodible stents in particular, such as the boundary element method (BEM) which limits discretization to the boundaries of the problem domain [52] and more recently numerical models applying arbitrary Lagrangian Eulerian (ALE) meshing which are capable of tracking a moving corrosion boundary [104], where the aim is to accurately predict both the corrosion rate and the displacement of the corrosion surface [35]. These numerical models allow to efficiently evaluate the performance of biodegradable stents *in silico*, thereby narrowing the range of designs to be tested in vitro or in clinical trials. The current section reviews the modelling methods to simulate degradation of absorbable polymeric stents and corrodible metal stents.

3.1 Finite element modelling of biodegradable polymeric stents

One of the first biomedical applications of synthetic biodegradable polymeric materials are bioabsorbable surgical sutures, which have been used in clinical practice since the 1970's [55]. A commonly used polymer for this application is poly-L-lactic acid (PLLA) which was later selected as a good candidate biodegradable material for absorbable stents (cfr. chapter 1). Polymers have a low elastic modulus and tensile strength compared to metals, resulting in bulky implants with thick struts. Degradation of aliphatic polyesters such as PLLA occurs via hydrolytic scission of the polymer chains. For most naturally occuring aliphatic polyesters, enzymes exist which act as a catalyst for hydrolysis, often referred to as active hydrolysis. For a synthetic polyester such as PLLA, hydrolysis *in vivo* is restricted to passive hydrolysis caused by diffusion of water molecules into the polymer matrix, due to the absence of aggressive enzymes. The fact that polymer degradation of PLLA is limited to passive hydrolysis *in vivo* considerably simplifies the development of appropriate mathematical degradation models. A schematic representation of hydrolytic degradation of PLLA is given in figure 3.1.

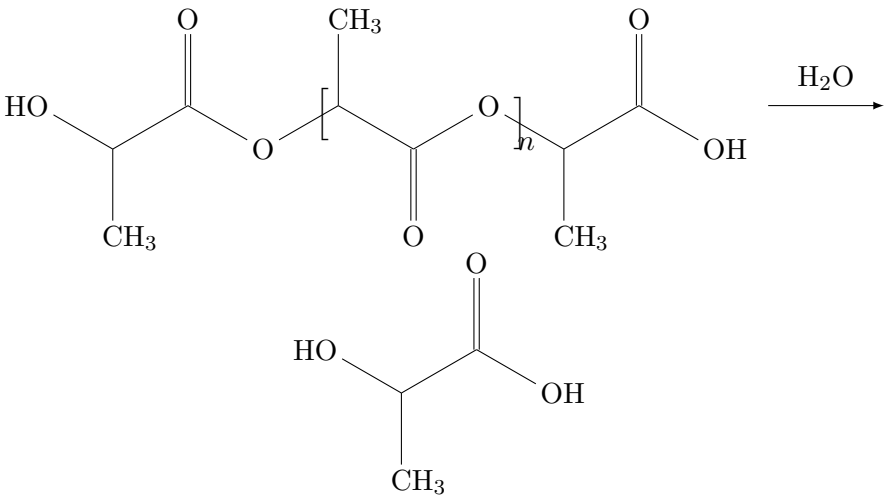

Figure 3.1: Hydrolytic degradation of poly-L-lactic acid.

The most important factors influencing hydrolytic scission of aliphatic polyesters in vivo are the local water concentration inside the polymer matrix and the pH-values. Increased acidity accelerates the degradation progress [34]. PLLA consists of both a crystalline and an amorphous phase for temperatures below its glass temperature (60 to 65 °C), with a crystallinity of around 37%. The polymer chains of the crystalline phase are ordered in a densely compacted structure with relatively small interstitial space compared to the amorphous phase, where the polymer chains form a random spaghetti-like structure (cfr. Figure 3.3). The concentration of H_2O-molecules will therefore be higher in the amorphous phase causing it to degrade faster than the crystalline phase. Preferential degradation of the amorphous phase is a beneficial characteristic for bioabsorbable polymeric stents: during the first months, degradation is confined to the amorphous phase while the load-bearing crystalline phase stays mostly intact, causing the stent to maintain its radial strength during this period. Once the amorphous phase has degraded, the crystalline phase is affected by hydrolytic scission and the stent gradually loses its radial strength.

Biodegradable polymers can be subjected to both surface erosion and bulk degradation. For hydrophobic polymers that allow little diffusion of water, hydrolytic degradation will be restricted to the polymer surface. For hydrophilic polymers such as PLLA, diffusion rates of water are several orders of magnitude larger than the kinetic degradation rates. Therefore, PLLA is subjected to bulk degradation: the water degradation rate is independent of a material point's

distance to the surface. This principle can be mathematically understood as follows. Suppose we have a polymer with an initial molecular weight W_0 which is exposed to water at its surface. Water will then diffuse into the polymer matrix with a diffusion coefficient α and reduce the molecular weight of the polymer chains via hydrolysis. The evolution of the reduction of molecular weight $\dot{W}$ can be written as a first order concentration dependent kinetic equation with kinetic constant β and evolution of concentration inside the polymer matrix obeys Fick's law, which results in the following couple of differential equations.

$$\dot{W}(c) : -\beta c \quad , \dot{c} = \alpha \nabla^2 c \tag{3.1}$$

The solution for concentration evolution for the 1D case of a straight surface of a semi-continuous polymer bulk in contact with water is given by the following expression, making use of the complementary error function erfc

$$c\,(x,t) = c_0 \mathrm{erfc}\left(\frac{x}{\sqrt{4\alpha t}}\right) \tag{3.2}$$

This results in the following expression for the evolution of the molecular weight W.

$$W\,(x,t) = W_0 - \beta c_0 \int_0^t \mathrm{erfc}\left(\frac{x}{\sqrt{4\alpha s}}\right) ds \tag{3.3}$$

Depending on the ratio between the diffusion constant α and the degradation kinetic constant β, degradation of the polymer will express itself as surface degradation or bulk degradation. This is illustrated in figure 3.2. The x-axis represents the distance to the polymer surface which is in contact with H_2O. The y-axis represents the molecular weight of the polymer and thus the degree of degradation. For the case where $\alpha >> \beta$, the degree of degradation throughout the polymer will be constant whereas when $\alpha << \beta$, degradation will be localized to a thin region close to the progressing surface. For the case where $\alpha \simeq \beta$, degradation will occur throughout the material with highest level of mass loss reduction at the surface [95].

In vitro experiments have shown PLLA sutures to degrade faster when under tensile load. This phenomenon has been attributed to the opening of the interstitial space between the polymer chains when under tensile load, allowing more diffusion of water molecules into

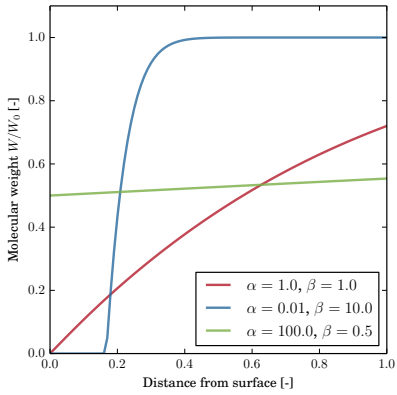

Figure 3.2: Schematic illustration of hydrolytic degradation inside a polymer according to equation 3.3 (α: diffusion coefficient, β: kinetic degradation constant).

the polymer matrix and to deformational activation of the chemical bonds [89]. This mechanism is schematically depicted in Figure 3.3. Soares et al. [90] have numerically investigated the possible effect of deformation upon degradation of polymeric absorbable stents [87]. In general, a deformation dependent degradation kinetic equation for the local degradation field d can be written as follows.

$$\dot{d} = K(\boldsymbol{F}, d, \dots) \tag{3.4}$$

Here $\dot{d} = \partial d/\partial t$ represents the degradation rate and $\boldsymbol{F}$ the deformation gradient (cfr. chapter 2). The expression of the kinetic function K takes the following form in [90].

$$\dot{d} = \frac{1-d}{\tau_d}\left[(I_1-3)^2 + (I_2-3)^2\right]^{\frac{1}{2}} \tag{3.5}$$

The expression takes into account the relative mass loss $1-d$ and the first and second invariant of deformation I_1 and I_2. τ_d is the overall degradation time constant. The degradation model can be implemented as a user defined field (UFIELD) and coupled with an appropriate constitutive model for the polymer mechanical behaviour (e.g. including visco-elasticity) to be compatible with the finite element solver Abaqus. For example, if a hyperelastic model is used, the degraded shear modulus μ_d could be obtained from the initial shear modulus μ_0 as

$$\mu_d = (1-d)\mu_0 \tag{3.6}$$

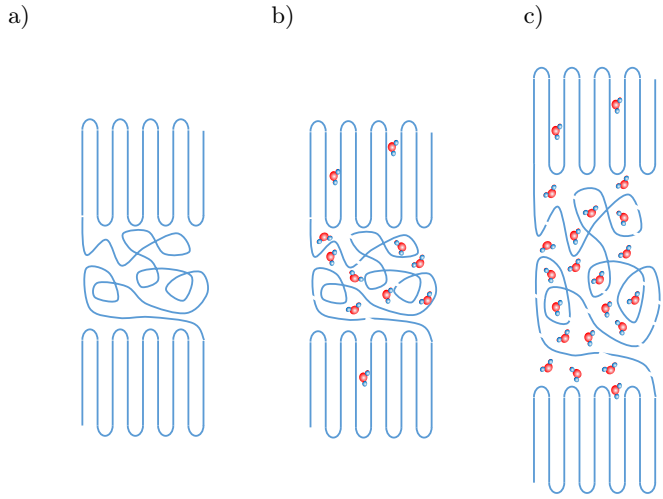

Figure 3.3: Schematic illustration of deformation accelerated hydrolytic degradation of a semi-crystalline polymer. Figure a): A semi-crystalline polymer consists of a crystalline phase (regularly order polymer chains) and a unordered amorphous phase. Figure b): The interstitial space between the polymer molecules is larger in the amorphous phase, allowing higher water concentration. Degradation will therefore preferentially occur inside the amorphous phase. Figure c): when the polymer matrix is deformed or stretched, the spaces between the molecule chains will open, allowing even more diffusion of water molecules into the polymer bulk. This mechanism is thought to cause deformation accelerated degradation [88].

Attempts have been undertaken to validate this model using pH-accelerated *in vitro* degradation tests of loaded sutures [90], where a significant increase of degradation rate and mass loss was found for cyclically loaded wires. However, applicability of the model to normal degradation time scales *in vivo* remains yet to be demonstrated.

3.2 Finite element modelling of biodegradable metallic stents

Degradation of metallic absorbable stents occurs via a combination of micro-galvanic corrosion, pitting corrosion, intergranular corrosion stress corrosion cracking and corrosion fatigue [13]. These phenomena affect the surface of the stent while the bulk of the stent struts remains unaffected. For stents, modelling of surface degradation has mainly focussed on pitting corrosion and stress corrosion of magnesium alloys. These models are phenomenological: the actual corrosion mechanisms at micro-scale level are not modelled explicitly but are approximated by a macro-scale degradation kinetic equation. The degradation field

only affects elements of the mesh that lay at the surface. Once an element is fully degraded ($d = 1$), the element is removed from the mesh and a new surface has to be assigned. Usually degradation of elements also effects the degradation rate of elements in the vicinity. Typically, the size of the elements has to be taken into account in the degradation rate equations.

The simplest model for surface degradation is uniform erosion, where degradation rates are distributed equally over the surface of the metal. It is used as an approximate representation of micro-galvanic corrosion of magnesium alloys with a homogeneous distribution of the alloying components. The continuum damage mechanics approach described in 2.8 can be combined with an appropriate description of the degradation field evolution. Rewriting equation 5.1, we find the general relation between the components of the effective 'non-degraded' stress tensor components $\tilde{\sigma}_{ij}$ and the nominal 'degraded' stress tensor components σ_{ij} for a given state of the degradation field d.

$$\sigma_{ij} = (1 - d)\tilde{\sigma}_{ij} \tag{3.7}$$

The general description of the evolution of uniform surface degradation d_u can be represented as follows.

$$\dot{d}_u = \frac{\delta_u}{L_e} K_u \left(d_u, \dots\right) \tag{3.8}$$

The term δ_u / L_e is introduced to make progression of the degradation surface less dependent of element size and contains the local element size L_e and a global uniform degradation element size factor δ_u. The form of the kinetic function $K_u \left(d_u, \dot{d}_u, \dots\right)$ is by most authors [30, 36, 102] reduced to a single kinetic constant k_u.

$$\dot{d}_u = \frac{\delta_u}{L_e} k_u \tag{3.9}$$

The uniform corrosion condition has been shown [35] to represent the best case scenario for biodegradable stent corrosion with respect to material mass loss rates and loss of radial strength, as localized weakening of the de stent is absent. However, as shown in chapter 4, uniform corrosion does not yield for the metal alloys used in current biodegradable stents, which display localized pitting corrosion and stress corrosion cracking. Gastaldi et al. [30] have presented the

following kinetic equation – which was originally introduced by [19] to model degradation of stainless steel – to model stress corrosion cracking of absorbable metal stents:

$$\dot{d}_{sc} = \begin{cases} \frac{L_e}{\delta_{sc}} \left(\frac{S\sigma_{eq}}{1-d} \right)^R & \text{if } \sigma_{eq} \geq \sigma_{th} \\ 0 & \text{if } \sigma_{eq} < \sigma_{th} \end{cases} \tag{3.10}$$

Here, L_e/δ_{sc} is a term introduced to reduce sensibility of the FE-mesh to local differences in element size L_e. The parameters S and R are kinetic constants that determine the shape and overall rate of the stress corrosion process, and σ_{eq} is the equivalent threshold stress at which stress corrosion occurs. For maximum principal stress levels lower than σ_{eq}, $\dot{d}_{sc}$ is set to zero. In [30], this equivalent stress was assumed to be 50% of the yield stress. The applicability of this model has been investigated by Wu et al. [103] through in vitro tests, showing that degradation material parameters could be fit to experimental data. However, this model does not account for localized pitting corrosion, which is present in both in vitro and in vivo degradation of absorbable magnesium alloys. Grogan et al. [36] have introduced a method to model localized corrosion by introducing an element-dependent pitting corrosion parameter λ_p into the equation 3.9 for uniform corrosion.

$$\dot{d}_p = \frac{\delta_p}{L_e} k_p \lambda_p \tag{3.11}$$

The FE-mesh surface elements are initially seeded with randomly distributed pitting corrosion parameters λ_p. Higher values of the pitting parameter will locally accelerate the degradation of an element. Once an element has fully degraded ($d = 1$), it is removed from the mesh and adjacent elements adopt the pitting parameter of the deleted element $\lambda_{p,del}$. In [36], this parameter is multiplied with a factor β to be able to model decelerated ($\beta < 1$) or accelerated ($\beta > 1$) pit formation.

$$\lambda_{p,adj} = \beta \lambda_{p,del} \tag{3.12}$$

After element removal, the surface of the FE mesh needs to be updated. Elements that were previously located at the bulk of the surface are new involved in degradation. The non-uniformity of pitting degradation in this model depends on the shape of the random

distribution of the seeded pitting parameters. Grogan et al. have proposed a Weibull-distribution for random seeding.

$$f(\lambda_p) = \begin{cases} \gamma \lambda_p^{\gamma-1} e^{\lambda_p^{\gamma}} & \text{if } \lambda_p \geq 0 \\ 0 & \text{if } \lambda_p < 0 \end{cases} \tag{3.13}$$

The shape of this distribution can be adjusted through the parameter γ. For values of $\gamma < 1$, the distribution becomes skew with a higher probability for small values of λ_p. In [35], a λ_p was set to 0.8, resulting in an initial seeding of the surface with low values of λ_p for most elements, except for some randomly distributed elements with high λ_p-values, to mimic localized pitting corrosion.

Two

Experiments

Chapter 4

In vitro experiments to characterize the evolution of the mechanical properties of a biodegradable stent magnesium alloy

The mechanical and degradation properties of the mathematical material models used during this research were calibrated by means of in vitro immersion testing on a magnesium alloy foil. Both degradation rates and mechanical properties have been measured. The experimental set-up used here was similar to the one used in [37] and includes degradation of dumbbell shaped specimens obtained via laser cutting out of a magnesium alloy (AZ31) film. Also, a series of stent strut shaped specimens have been laser cut and subjected to in vitro corrosion testing.

4.1 Corrosive degradation of magnesium and its alloys

4.1.1 Corrosion of pure magnesium

Metals undergo electrochemical oxidation when in an aggressive environment. During a redox reaction – or oxidation-reduction reaction – an oxidizing agent or oxidant increases its electric charge by removing

electrons from a reducing agent, the reductant. Metals willingly give away electrons and are therefore oxidized according to the following general oxidation half-reaction:

$$\mathrm{M} \longrightarrow \mathrm{M^{n+}} + \mathrm{ne^-} \tag{4.1}$$

The oxidants and reductants have to be in electrical contact to allow for the transfer of electrons, e.g. via an aqueous environment. In a physiological fluid such as blood which contains several inorganic ion species, the released ions of a corrodible metal can combine to form oxides or salts. The susceptibility of a metal alloy to corrosion is generally reflected by its standard hydrogen electrode potential. Galvanic corrosion occurs when two metals with differing electrode potentials get into electrochemical contact, i.e. the more active material or the metal with the lowest redox potential will react preferentially while corrosion of the more noble material decelerates. Figure 4.1 shows the galvanic series of metals and metal alloys in flowing seawater and clearly illustrates their relative corrosion tendencies. Pure magnesium and magnesium alloys are the most active of all structural materials and have, without modifications, a very low corrosion resistance and will act as anode when coupled to any other metal.

A magnesium alloy consists of several material phases which can all be affected by corrosion attack when in an aqueous environment. Magnesium will dictate the corrosion properties of the alloy because of its high corrosive reactivity in water. When looking at pure magnesium, corrosion proceeds via an electrochemical reaction of magnesium with water, producing magnesium hydroxide and hydrogen gas (H_2), resulting in one molecule of H_2-gas for every dissolved magnesium ion.

$$2\mathrm{Mg} + 2\mathrm{H_3O^+} \longrightarrow 2\mathrm{Mg^{2+}} + 2\mathrm{OH^-} + 2\,\mathrm{H_2} \ \text{(overall reaction)} \tag{4.2}$$

$$\mathrm{Mg^{2+}} + 2\mathrm{OH^-} + 2\,\mathrm{H_2} \longrightarrow \mathrm{Mg(OH)_2}\downarrow \ \text{(salt formation)} \tag{4.3}$$

Here, the overall corrosion reaction is the sum of the following electrochemical partial reactions:

$$2\mathrm{Mg} \longrightarrow 2\mathrm{Mg^+} + 2\mathrm{e^-} \ \text{(anodic reaction)} \tag{4.4}$$

$$2\mathrm{H^+} + 2\mathrm{e^-} \longrightarrow \mathrm{H_2} \ \text{(cathodic reaction)} \tag{4.5}$$

$$2\mathrm{Mg^+} + 2\mathrm{H_2O} \longrightarrow 2\mathrm{Mg^{2+}} + 2\mathrm{OH^-} + \mathrm{H_2} \ \text{(chemical reaction)} \tag{4.6}$$

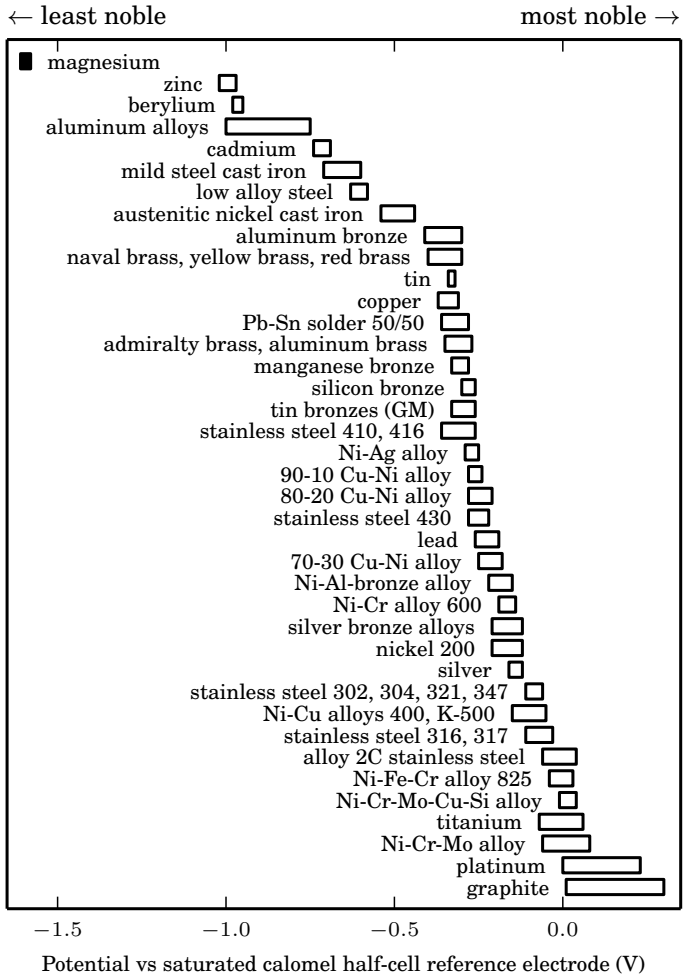

Figure 4.1: Galvanic corrosion of metals and metal alloys in flowing seawater. Adapted from [38].

As can be seen from Equation 4.2, the overall reaction consumes H^+ and produces OH^-, thereby increasing the pH-value of the solution. The decreasing acidity favours the formation of $Mg(OH)_2$-precipitates as shown in equation 4.3, thus forming a semi-permeable deposition layer on the metal surface, acting as a protective barrier and slowing down further corrosion.

Atrens et al. [6] have proposed a more detailed reaction mechanism for pure magnesium corrosion, introducing Mg^+ as intermediate between metallic Mg and the dissolved Mg^{2+}-ions.

$$Mg \longrightarrow Mg^+ + e^- \tag{4.7}$$

$$kMg^+ \longrightarrow kMg^{2+} + ke^- \tag{4.8}$$

$$(1+k)H_2O + (1+k)e^- \longrightarrow \tfrac{1}{2}(1+k)H_2 + (1+k)OH^- \tag{4.9}$$

$$(1-k)Mg^+ + (1-k)H_2O + (1-k)OH^- \longrightarrow (1-k)Mg(OH)_2 + \tfrac{1}{2}(1-k)H_2 \tag{4.10}$$

Only a fraction k of the intermediate Mg^+-ions is converted to stable $Mg_2{}^+$-ions (Equation 4.9), whereas the complementary fraction $1-k$ reacts chemically to form magnesium hydroxide $Mg(OH)_2$ (Equation 4.10). As a consequence, electrochemical measurements of pure magnesium corrosion will yield corrosion rates that are lower than the actual corrosion rate. To obtain the real corrosion rate, gravimetric techniques and measurement of hydrogen evolution are the preferred methods. This passivation mechanism is not valid for chloride-containing electrolyte solutions, where the metastable magnesium hydroxide $Mg(OH)_2$ is converted into highly soluble magnesium chloride. This causes the protective $Mg(OH)_2$-layer to brake down and exposes the metallic surface to further dissolution of magnesium.

$$Mg(OH)_2 + 2Cl^- \longrightarrow Mg_2{}^+ + 2Cl^- + 2OH^- \tag{4.11}$$

The stability of the partially protective $Mg(OH)_2$-layer depends on the applied electrode potential difference. For potential differences lower than a threshold potential – the pitting potential E_p – the metallic surface remains entirely covered by the protective $Mg(OH)_2$-film. For voltages above the pitting potential E_p, the protective film will start to break down, exposing the metallic magnesium surface to localized corrosion attack. The presence of impurities causes localized galvanic corrosion or pitting corrosion and increases the anodic reaction rate and the rate of formation of H_2-gas. Due to the formation

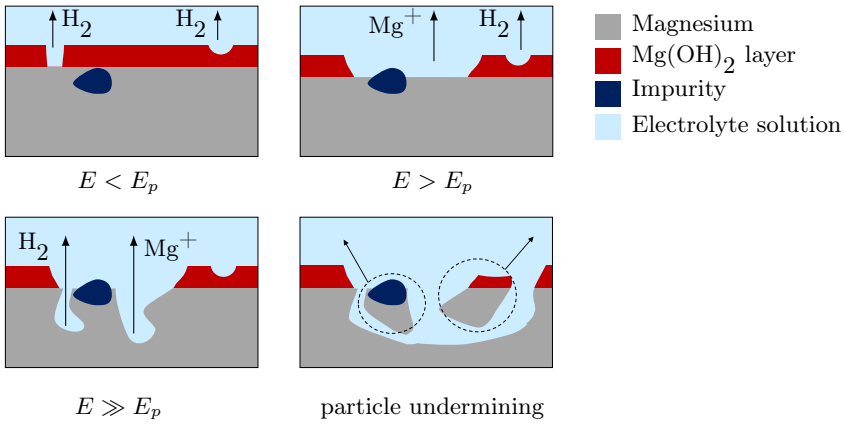

Figure 4.2: Corrosion of pure magnesium at different values of the electrode potential difference. For a potential difference E smaller than the pitting potential E_p, a magnesium hydroxide ($Mg(OH)_2$) layer acts as a partially protective barrier ($E < E_p$). For values of E that slightly exceed E_p, the protective layer is broken down and magnesium ions are able to dissolve ($E > E_p$). Impurities cause localized galvanic corrosion or pitting with the metallic magnesium acting as anode for further increasing potential differences ($E \gg E_p$). Additional loss of mass is caused by undermining of magnesium particles [6].

of pits, the total exposed surface area increases, thereby further increasing the corrosion rate. Magnesium mass loss is also accelerated by particle undermining and the release of metal grains.

4.1.2 Corrosion of magnesium alloys

The above described mechanisms are valid for pure metallic magnesium. For magnesium alloys, the corrosion process becomes more complex and also metallurgic factors such as the alloying conditions influence the final corrosion mechanism. In general, magnesium alloys are more resistant to corrosion. In aluminium (Al) containing magnesium alloys, the protective film at the metal surface is stabilized by the formation of Al_2O_3, thereby increasing corrosion resistance up to an Al-content of maximally 4 weight-percent (wt%). Higher Al-contents lead to the formation of a second phase which is detrimental for corrosion resistance because large secondary phase particles tend to be undermined by laterally spreading corrosion fronts. Because of its low standard electrode potential compared to other engineering metals, magnesium will undergo both micro- and macro-galvanic corrosion when in electrical contact with nobler secondary phase metals.

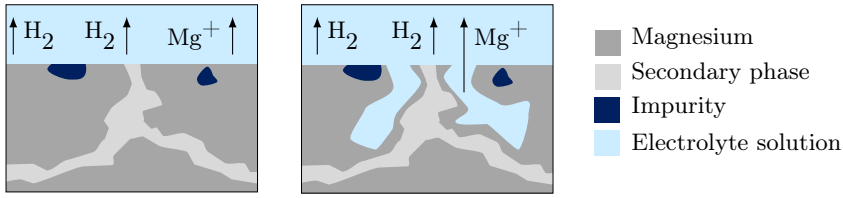

Figure 4.3: Illustration of the micro-galvanic corrosion mechanism for magnesium alloys in an aqueous environment. A secondary phase alloying metal concentrates at the grain boundaries and acts as a local cathode for micro-galvanic corrosion, causing the corrosion fronts to advance laterally along these grain boundaries. Adapted from [6].

The effect of increasing alloying levels upon corrosion resistance for various alloying elements has been investigated by Song and Atrens [91]. Most alloying metals serve as cathodic sites when their weight-percentage exceeds an element-specific tolerance limit, causing micro-galvanic induced acceleration of magnesium corrosion. Secondary phase alloying metals concentrate at the magnesium grain boundaries and at impurities and act as local galvanic cathodes compared to the anodic magnesium matrix which is dissolved preferentially. Scanning electron microscopy (SEM) studies have confirmed that localized pitting corrosion is the dominant corrosion mechanism for most magnesium alloys. However, for medical device applications such as biodegradable stents, uniform surface degradation would constitute the preferred corrosion mechanism as it would result in more predictable corrosion properties and more reliable time-dependent mechanical properties, and would also avoid the loss of large particles that could trigger unwanted inflammatory reactions and cause blocking of the downstream capillaries.

Next to pitting corrosion, magnesium alloys that are subjected to static or cycling loading can also undergo stress corrosion cracking (SCC). Inter-granular stress corrosion cracking (IGSCC) originates from the propagation of cracks along the grain boundaries which

contain the secondary alloy phases. Trans-granular stress corrosion cracking (TGSCC) is caused by strain-induced rupture of the protective $Mg(OH)_2$-film and the subsequent formation of crack due to hydrogen embrittlement.

4.2 Experimental techniques to characterize magnesium corrosion

4.2.1 In vivo and in vitro magnesium corrosion

The general clinical consensus states that corrodible medical devices should not dissolve prior to six months to prevent early mechanical device failure and to avoid loss of material fragments that could trigger embolisation of the treated vessel. Several studies have attempted to quantitatively determine corrosion rates of magnesium devices *in vivo*. However, a major limitation of these in vivo studies is that degradation rates cannot be assessed without disrupting the physiological environment. Specimens have to be explanted to establish the degree of corrosion, which – next to relatively high costs – causes the obtained information to be fragmentary and providing little insight into the actual in vivo processes. A more flexible and less costly alternative to in vivo experiments are models that allow for almost real-time characterisation of magnesium corrosion by using an aqueous or (simulated) physiological environment *in vitro*. By using an in vitro setup, quantitative and accurate information can be obtained within a feasible period of time. However, the in vitro test conditions also show some important limitations. Several studies have pointed out significant discrepancies between the corrosion rates observed under in vivo and simulated in vitro conditions, which were substantially higher for the in vitro cases. In vitro corrosion rates have been reported to be up to four orders of magnitude higher than corresponding in vivo results. The vast number of factors influencing corrosion in vivo and the complexity of the dynamic in vivo environment are the main reason why the strongly simplified in vitro test bench conditions have not yet proven suitable to predict in vivo corrosion rates. A simulated in vitro experimental setup was nonetheless chosen for this study because of its feasibility and the ability to observe corrosion rates real-time. Furthermore, the obtained data will be sufficient to use as input for the here used mathematical models, which are mostly conceptual.

Various in vitro test setups have been proposed and designed to quantify the corrosion rates of magnesium alloys in saline environments. Electrochemical testing is an elegant and convenient way

of characterizing corrosion properties based on the measurement of the open circuit electrode potential, or via electrochemical impedance spectroscopy. However, as mentioned previously, electrochemical measurements do not fully capture the total corrosion rate. Immersion testing is therefore more commonly used. In case of a biocompatible and biodegradable metal such as a magnesium alloy, the preferred immersion fluid is a solution that mimics body fluids such as blood plasma. Table 4.1 lists the ion concentrations of blood plasma and two commonly used buffered electrolyte solutions, conventional simulated body fluid (c-SBF) and Hanks' solution. Also a revised simulated body fluid solution (r-SBF) exists which exactly matches the ion concentrations of blood plasma. The composition of the electrolyte solution highly influences the outcome of the corrosion tests. As mentioned previously, chloride-ions (Cl^-) contribute aggressively to the corrosion rate because they convert the $Mg(OH)_2$-precipitate into soluble magnesium chloride ($MgCl_2$) and therefore break down the partially protective film. Apart from the inorganic ions, also the organic compounds contained in blood plasma play a major role. For example, the adsorption of proteins such as albumin on the metal surface and the subsequent formation of a biofilm has a tempering influence on the corrosion rate: it has been shown that diffusion of ions is severely restricted by cell-line biofilms that tend to stabilize the protective $Mg(OH)_2$-cover. The absence of organic compounds for largely explains why magnesium degradation rates can be orders of magnitude higher during in vitro experiments, compared to in vivo corrosion.

Table 4.1: Ion concentrations of human blood plasma and of two artificial and commonly used simulated solutions, conventional simulated body fluid (c-SBF) and Hanks' solution.

ion	ion concentration (mmol/l)		
	blood plasma	c-SBF	Hanks'
Na^+	142.0	142.0	141.6
K^+	5.0	5.0	5.4
Mg^{2+}	1.5	1.5	0.9
ca^{2+}	2.5	2.5	1.3
Cl^-	103.0	147.8	144.6
HCO_3^-	27.0	4.2	4.2
HPO_4^{2-}	1.0	1.0	0.8
SO_4^{2-}	0.5	0.5	0.9

As can be seen from equation 4.11, apart from the formation of soluble $MgCl_2$, the presence of Cl^--ions promotes the formation of OH^- and therefore increases the pH-value of the solution. The presence of Ca^{2+}-ions is thought to promote the formation of a magnesium-containing calcium phosphate precipitate layer. The formation of such a precipitate layer is mediated by the presence of OH^--ions and is stimulated with increasing pH-values.

$$(i - i')\mathrm{Ca}^{2+} + i'\mathrm{Mg}^{2+} + j{\mathrm{PO}_4}^{3-} + k{\mathrm{CO}_3}^{2-} + l\mathrm{OH}^- \longrightarrow (\mathrm{Mg, Ca})_\mathrm{i}(\mathrm{PO}_4)_\mathrm{j}(\mathrm{CO}_3)_\mathrm{k}(\mathrm{OH})_\mathrm{l} \quad (4.12)$$

The deposition of a calcium phosphate or hydroxylapatite layer might be beneficial for the biocompatibility of magnesium alloys as a material for e.g. bone implants. The composition of the surface precipitate layer and the substrate can be determined via energy-dispersive X-ray spectroscopy (EDX) or alternatively via X-ray crystallography (XRD) or Fourier transform infra-red spectroscopy (FTIR).

The simplest method to quantify the corrosion rate of a test specimen undergoing in vitro degradation is the gravimetric technique, where the amount of mass loss at a given degradation time is simply defined by subsequently extracting the sample from the corroding solution, cleaning the sample to remove adhered corrosion products and then measuring the remaining mass to compare with the original mass of the sample. The corrosion rate CR is defined as the mass loss W per unit of surface area A and per unit of time t and has dimensions $\mathrm{mg/cm^2/h}$:

$$CR = \frac{W}{At} \quad (4.13)$$

However, this method has some severe limitations. The main disadvantage of the gravimetric corrosion estimation technique is the perturbation of the system and the necessity to sacrifice each specimen at the time of evaluation, therefore requiring a large amount of testing samples to obtain a statistically reliable estimation of the corrosion rate. The largest experimental error is induced in the process of rinsing the specimens to remove corrosion products: cleaning with distilled water might be insufficient to remove all corrosion products, brushing could leave scratches and therefore contribute to mass loss while aggressive chemical solutions could react with the non-corroded metal matrix in case of excessive exposure times.

In this study we used the method proposed by Song et al. to quantify static in vitro magnesium corrosion rates, which derives the amount of corroded magnesium by measuring the amount of hydrogen gas produced during the corrosion reaction. As can be seen from reaction equations 4.2 and 4.3, dissolution of one Mg^{+}-ion results in the formation of one molecule of H_2-gas. Therefore measuring the amount of evolved hydrogen gas is equivalent to measuring the amount of dissolved magnesium. We can use the ideal gas law to derive the number of moles n of H_2 (and Mg^{+}) from the measured volume of evolved H_2-gas:

$$n_{Mg^+} = n_{H_2} = \frac{pV}{RT} \tag{4.14}$$

R is the ideal gas constant. At a standard atmospheric pressure ($p = 101.325\,\text{kPa}$) and at room temperature ($T = 293\,\text{K}$), 1 ml of H_2-gas corresponds with 1.01 mg of Mg mass loss.

The hydrogen evolution method is applicable to pure magnesium as under the assumption of equations 4.2 and 4.3, but is also valid for magnesium alloys with a single or multi-phase microstructure. Loss of larger particles due to undermining also contribute to H_2 formation, unless consisting of a non-corroding secondary phase. The maximal error due to particle undermining has been estimated to be 10% for the relevant engineering magnesium alloys. Another prerequisite for the above method is that the contribution of oxygen reduction should be negligible.

4.3 Materials and Methods

The magnesium/aluminium/zinc alloy (AZ31, Mg31/Al96/Zn1) was sourced in the form of a 0.25 mm thick foil (Goodfellow, UK). The foil had dimensions 100 mm × 100 mm × 0.25 mm and a net weight of 4.5 g (density $\rho = \text{g/cm}^3$). AZ31 is a magnesium alloy which has properties similar to the magnesium alloy WE43 which is used as the backbone material for the Absorbable Metal Stent (AMS) of Biotronik [43, 73]. For example, both materials AZ31 and WE43 have a grain size of 40 μm, [107] and a UTS of resp. 264 MPa and 295 MPa. Dumbbell shaped tensile test specimens were obtained by laser cutting, as shown in figure 4.4. All samples have been cleaned with isopropyl alcohol to remove oils from the surface and have subsequently been dried in a glassware drying oven at 50°C. To restrict corrosion to the gauge section of the dumbbell specimens, the end regions have been

covered with a layer of petroleum jelly, which acts as a water repellent protective coating. Initial corrosion products were removed from the surface using a 20% chromium acid solution, which leaves the alloy base material unaffected. The samples are subsequently rinsed using ethanol and dried. Some samples have been selected for scanning electron microscopy (SEM). They were put in a vacuum furnace for 4 hours to remove contaminants. The vacuum prevents further oxidation of the material. Also created via laser cutting were strut shaped tensile testing specimens, also shown in figure 4.4. These samples were first loaded inside an Instron tensile tester at different strain levels and later subjected to corrosion to investigate the possible influence of deformation upon corrosion rates.

The corrosive medium used for immersion testing was so-called conventional simulated body fluid (c-SBF). c-SBF ion concentrations resemble those of blood plasma. The solution was prepared by sequentially dissolving the reagents listed in Table 4.2 in distilled water, while magnetically stirring and heating to 36.5°C. Titration with 1M HCl aqueous solution is performed to adjust the pH to 7.4. After cooling to room temperature, pure water is added to obtain a volume of 1000 ml. Since the pH has a major influence on the in vitro corrosion rate, the solution was buffered using tris(hydroxylmethyl)aminomethane (TRIS). The electrolyte solution was stored in a closed container at 4°C.

Tensile testing was carried out on an Instron 5800R electromechanical testing system with a static 1 kN load cell. The speed of the

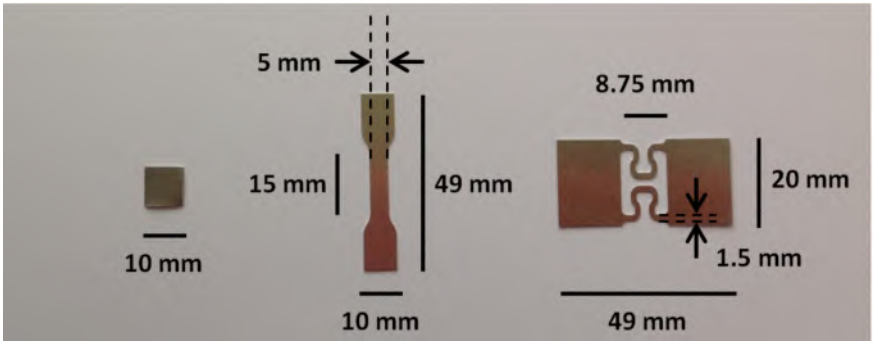

Figure 4.4: Magnesium foil test specimens used in the degradation and tensile testing experiments. The samples were obtained by laser cutting. The first sample was used to quantify corrosion rates. A series of the second dumbbell shaped specimen were used to establish the mechanical properties as a function of degradation time. The last specimen represents two stent struts. All samples had a thickness of 0.2 5mm.

Table 4.2: Reagent amounts per 1000ml distilled water for c-SBF, in the order of addition.

Reagent	Amount of c-SBF per 1000 ml
NaCl	8.036 g
$NaHCO_3$	0.352 g
KCl	0.225 g
$K_2HPO_4 \cdot 3\,(H_2O)$	0.230 g
$MgCl_2 \cdot 6\,(H_2O)$	0.311 g
1M HCl	40 ml
CaCl	0.293 g
Na_2SO_4	0.072 g
TRIS	6.063 g

crossheads was set to 2 mm/min for all tests. The analog signal coming from the system was sampled at a frequency of 10 Hz.

The general setup for the static immersion corrosion experiment is shown in Figure 4.5. An oil bath was used to maintain the solution temperature at 36.5°C and distilled water was added to the container at regular time intervals to compensate for evaporation. The magnesium corrosion specimen is immersed in the cSBF solution and placed under a glass funnel. When the corrosive medium reacts with the magnesium-alloy, H_2 gas bubbles form, which are collected by the

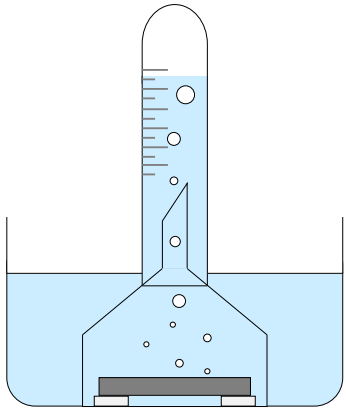

Figure 4.5: Schematic representation of the in-vitro magnesium alloy corrosion experimental set-up.

funnel and accumulate inside a graduated test tube. By measuring the amount of H_2 at regular time intervals we can derive the corrosion rate dynamically without having to perturb the system. A number of samples have been selected for scanning electron microscopy (SEM) to visualise the corrosion mechanism based on the surface topology.

4.4 Experimental results

The measured evolution of mass loss as a function of immersion time is plotted in the left chart of figure 4.6. Initially, i.e. within the first few hours, the corrosion rate is relatively low with a value of 0.080 mg cm^{-2} h^{-1}. After six hours of immersion, the corrosion rate increases significantly to a value of 0.115 mg cm^{-2} h^{-1} and then stabilizes to a quasi steady state value of 0.103 mg cm^{-2} h^{-1}. During the 100 h period of immersion, the pH of the solution was observed to tend to slightly increase, deviating form the initial value of pH 7.4 up to a pH 7.8. Because increasing pH levels can have a decelerating effect on degradation, the pH was regularly measured and manually adjusted if necessary. The sudden increase of the corrosion rate after 6 h of immersion is difficult to understand and not in correspondence with observations made by other authors. The later stabilization of the corrosion rate can be explained by the formation of a partially protective $Mg(OH)_2$-layer on the specimen's corroding surface. The measured steady state corrosion rate is similar to the value measured in [35], i.e. a value of 0.103 mg cm^{-2} h^{-1} vs. a value of 0.084 mg cm^{-2} h^{-1}.

The experimental results were subsequently used to fit the models presented by Gastaldi et al. [30] (stress corrosion) and Grogan et al. [36] (pitting corrosion) – see chapter 3 for a description of these models. The corrosion models were implemented as Fortran subroutines to be compatible with the finite element solver Abaqus/standard (Simulia, Dassault Systèmes). Finite element models for the different test specimens were generated using the in-house developed open-source software pyFormex. The experiments described above were then repeated virtually to fit the parameters in the degradation rate equations below:

$$\text{Gastaldi}: \ \dot{d}_{sc} = \begin{cases} \frac{L_e}{\delta_{sc}} \left(\frac{S\sigma_{eq}}{1-d} \right)^R & \text{if } \sigma_{eq} \geq \sigma_{th} \\ 0 & \text{if } \sigma_{eq} < \sigma_{th} \end{cases} \tag{4.15}$$

$$\text{Grogan}: \ \dot{d}_p = \frac{\delta_p}{L_e} k_p \lambda_p \tag{4.16}$$

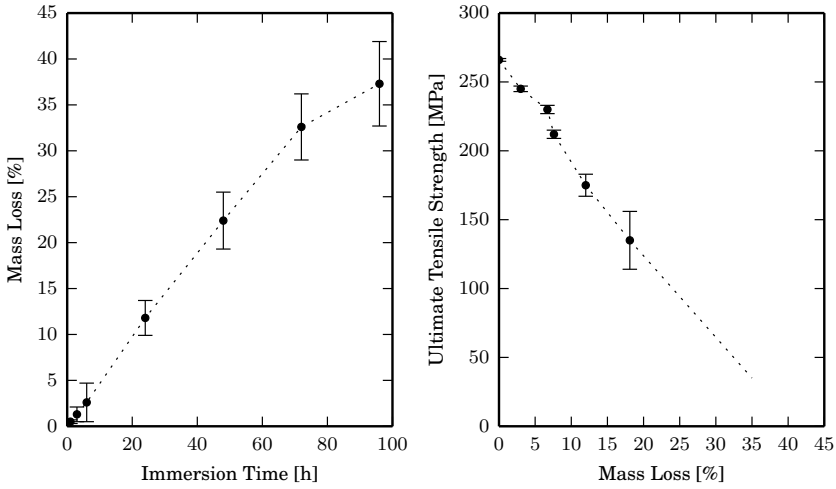

Figure 4.6: Results of the static immersion tests and tensile testing of the magnesium alloy AZ31 specimens. The left graph shows the relative amount of magnesium mass loss over time. The right graph shows the evolution of the ultimate tensile strength (UTS) as a function of magnesium mass loss.

Meshing resulted into geometric models with 31360 C3D8-elements (3D 8 node continuous elements) for the dumbbell shaped model and 38000 C3D8-elements for the stent cell shaped model. Repetitive manual adjustment of the model parameters resulted in values of 0.144 mm for the parameter δ_u (cfr. $\delta_u = 0.017$ mm in Grogan et al. and $\delta_u = 0.100$ mm in Gastaldi et al.) and $K_u = 0.0065h^{-1}$ (cfr. $K_u = 0.0042h^{-1}$ in Grogan et al. $K_u = 0.0050h^{-1}$ in Gastaldi et al.). The model of Grogan uses a value of 0.8 for the parameter *beta*, which couples the transition of pitting parameters to neighbouring elements after element deletion. In our simulations, a value of 0.5 for β was giving better results. The other parameters were not fitted but assumed the same as in [30] and [36]. As an example, simulation results for the straight section of the dumbbell specimens are shown in Figure 4.8.

The stress corrosion experiment by making use of strut-shaped specimens, deformed at different strain rates gave no clear results. Although literature suggests accelerated degradation in regions of high stress or deformation – the basic assumption for the model of Gastaldi et al. – no such corrosion acceleration could be observed during the experiments. The small dimensions of the struts resulted in fast embrittlement of the magnesium. Variations on the tensile testing re-

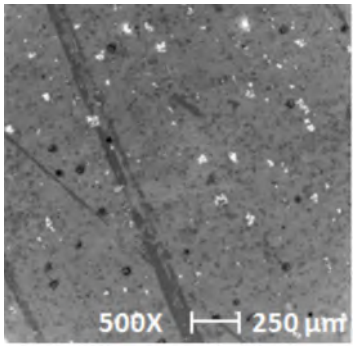

(a) Surface prior to corrosion

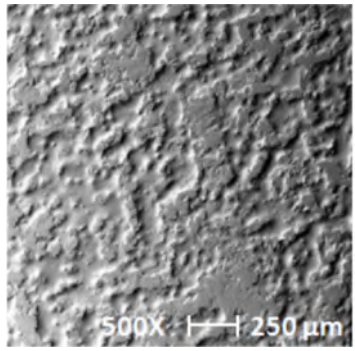

(b) Surface after 6 hours of corrosion

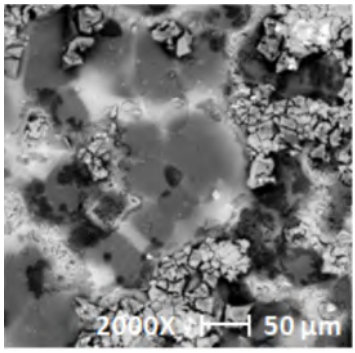

(c) Surface with precipitates

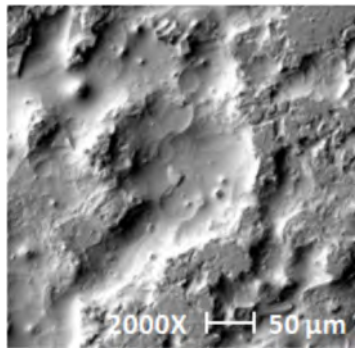

(d) Surface without precipitates

Figure 4.7: Scanning Electron Microscope (SEM) images of the AZ31 magnesium alloy surface. Figure 4.7a shows the non-corroded alloy surface. Figure 4.7b shows the same specimen after 6 hours of immersion in a corrosive solution, with the precipitates removed from the surface. Non-uniform pitting corrosion can be observed. Figures 4.7c and 4.7d zoom in on the precipitate cover and the underlying pits. Magnification scales are included in the images.

sults were therefore large, overriding any measurable effect of stress corrosion.

4.5 Conclusions

An *in vitro* approach was chosen to investigate the degradation behaviour of the magnesium alloy AZ31. This alloy is a representative material for magnesium stents and is comparable to WE43, which forms the backbone of the Absorbable Magnesium Stent (AMS) of Biotronik. A limitation of the *in vitro* experiments is that they result in accelerated corrosion compared to *in vivo* conditions, mainly because of the formation of a protective protein and cell adhesion layer on the metal surface *in vivo*. On the other hand, *in vitro* magnesium

corrosion experiments are relatively simple and allow to continuously monitor corrosion rates without disrupting the corrosive environment. Animal studies would require a large amount of subjects to obtain *in vivo* corrosion data at isolated time points. For the scope of fitting material model parameters, an *in vivo* approach was considered to be sufficient. The experimental results showed values for magnesium corrosion rates slightly higher than values reported in literature, though within the same range of magnitude. The data could eventually be used to fit material degradation constants to existing corrosion models by virtual repetition of the real experiments.

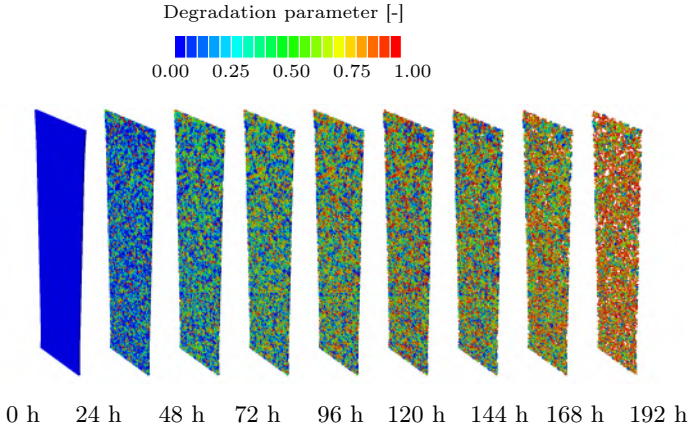

Figure 4.8: Simulated corrosion of the rectangular section of a magnesium dumbbell specimen at 9 different time points. The color plot indicates the degradation field d which has values between 0 (blue) and 1 (red).

Three

Computer Modelling

Chapter 5

A computational framework to model degradation of biocorrodible metal stents using an implicit finite element solver

Bioresorbable stents represent an emerging technological development within the field of cardiovascular angioplasty. Their temporary presence avoids long-term side effects of non-degradable stents such as in-stent restenosis, late stent thrombosis and fatigue induced strut fracture. Several numerical modelling strategies have been proposed to evaluate the transitional mechanical characteristics of biodegradable stents using a continuum damage framework. However, these methods rely on an explicit finite-element integration scheme which, in combination with the quasi-static nature of many simulations involving stents and the small element size needed to model corrosion mechanisms, results in a high computational cost. To reduce the simulation times and to expand the general applicability of these degradation models, this paper investigates an implicit finite element solution method to model degradation of biodegradable stents. This work was accepted for publication into the Annals of Biomedical Engineering.

5.1 Introduction

5.1.1 Biodegradable stents

The emergence of percutaneous coronary intervention (PCI) with stenting to treat arterial stenosis, a minimally invasive procedure, has led to shortened revalidation times and decreased mortality rates compared to open-chest bypass surgeries [86]. The primary function of stents is to open and scaffold a locally narrowed blood vessel, thereby restoring blood flow. Conventional stents have a metallic backbone and reside permanently in the body after placement. They are often coated with an anti-proliferative drug containing polymeric layer to locally inhibit side effects such as in-stent restenosis due to excessive neo-intimal tissue growth. The need for mechanical support of the healing artery however is temporary and beyond the first few months there are disadvantages of a permanent metallic prosthesis: next to in-stent restenosis [29], prolonged exposure of the metallic stent surface to the blood stream increases the risk for late stent thrombosis [96] and long periods of cyclic loading of the stent can lead to fatigue induced strut fracture [56]. This is why biodegradable stents, which only temporarily support the blood vessel and afterwards fully disintegrate, have been gaining much interest over the past two decades. Ideally, the biodegradable stent should be able to retain its mechanical integrity during the 6 to 12 months arterial healing period and subsequently degrade into non-toxic and non-inflammatory by-products that are readily soluble inside the human body [73]. Its temporary nature allows for arterial remodelling and vessel growth, making the biodegradable stent particularly interesting for paediatric applications [4]. biodegradable (polymeric) stents could also serve as a vehicle for local drug or gene delivery systems [50].

Two classes of biocompatible and biodegradable materials are currently being used for biodegradable stents: biocorrodible metals and biodegradable polymers. Polymeric materials for stents are biodegradable aliphatic polyesters such as poly-L-lactic acid (PLLA) [98]. These polymers can be tailored to have well-defined degradation kinetics and display relatively long degradation times (6 to 24 months) but have rather poor mechanical strength. Biocorrodible metals for stents include magnesium alloys (such as magnesium-aluminium-zinc alloys) and pure iron [27]. Biocorrodible metalic stents have the advantage of displaying material properties resembling those of conventional stents, but show less predictable and relatively fast (< 6 months) degradation behaviour (corrosive surface degradation) [26].

An ideal stent would combine the advantages of both classes of biomaterials, e.g. a biocorrodible metallic stent coated with a bioabsorbable protective polymeric layer [85].

Several biodegradable stents have been developed and are subject of clinical trials. The biodegradable Vascular Scaffold (BVS) of Abbott Vascular is a polymeric biodegradable stent made of PLLA and is coated with an everolimus-eluting poly-D,L-lactic acid (PDLLA) layer [82]. Extensive testing of this stent in the ABSORB clinical trials suggests sufficient long-term safety with acceptable stent recoil and reduced late stent thrombosis [32]. Thanks to these good results, the BVS has been approved with the European CE marking since 2012 [1]. The main stent representing the class of biocorrodible metallic stents is the Absorbable Metal Scaffold (AMS) of Biotronik which is followed up in the PROGRESS-trials [40]. Early clinical results for this stent have raised concerns with respect to safety: fast degradation and subsequent early loss of radial force result in early recoil and excessive neointima formation, causing a high restenosis recurrence rate after 4 months [97]. Newer designs aim at prolonging the radial support by changing the geometry, alloy composition, strut dimensions or by applying a drug eluting coating.

5.1.2 Computational modelling of biodegradable stents

Computational modelling is a valuable tool when optimizing stent designs and when evaluating stent mechanics. Finite element analysis (FEA) has proven to be a valid and efficient method to virtually investigate and optimize the mechanical behaviour of minimal invasive devices such as stents [9, 48, 61, 64] and can be combined with patient specific images to plan a surgical procedure or to classify specific devices for different kinds of atherosclerotic lesions [8, 49, 63]. When combined with computational fluid mechanics, the finite element method is able to reveal insight into aspects of drug elution and coating biodegradation [15, 20, 57]. Analysing the mechanical behaviour of biodegradable stents via finite element simulations poses new challenges due to the complexity of the stent materials which display transitional mechanics both in the long term range (polymer degradation, metal corrosion) and the short term range (viscoplasticity in case of polymeric stents). A limited number of FEA-studies on biodegradable stents has been performed. With respect to polymeric scaffolds, Soares et al. proposed a continuum degradation model which includes the effect of deformation upon the degradation rate of polylactic acid and applied it to biodegradable stents [90]. Bokov et al. investigated the interaction of a biodegradable polymeric stent

with the vascular wall using FEA [12]. Our group has studied the effect of the deployment rate on the mechanical integrity of a PLLA stent via FEA [22].

Several computational methods have been proposed to physically model surface degradation of corrodible metals and of biocorrodible stents in particular, such as the boundary element method (BEM) which limits discretization to the boundaries of the problem domain [52] and more recently numerical models applying arbitrary Lagrangian Eulerian (ALE) meshing which are capable of tracking a moving corrosion boundary [104], where the aim is to accurately predict both the corrosion rate and the displacement of the corrosion surface [35]. However, to be able to model the mechanical and degradation behaviour of complex 3D structures such as stents, a different strategy has to be followed. A more practical engineering approach applicable to complex 3D geometries is the use of continuum damage mechanics. Continuum damage theory allows to account for the effects of corrosion on the structural integrity of the material without resorting to an explicit description of microscopic phenomena and their progression. It is therefore a phenomenological approach. Here, the effects of progressing damage upon the material mechanics are represented by means of one or more arbitrary state variables. Lemaitre and Desmorat [58] originally proposed the following relation between a scalar damage field d, the true stress $\boldsymbol{\sigma}$ and an effective stress $\bar{\boldsymbol{\sigma}}$:

$$\bar{\boldsymbol{\sigma}} = \frac{\boldsymbol{\sigma}}{1-d} \tag{5.1}$$

The degradation or damage field d has values between 0 (non-degraded) and 1 (fully degraded) and can be a function of a number of variables such as time t, the position $\boldsymbol{x}$ within a material, local deformation $\boldsymbol{\varepsilon}$, local stresses $\boldsymbol{\sigma}$ etc., $d = d(t, \boldsymbol{x}, \boldsymbol{\varepsilon}, \boldsymbol{\sigma}, ...)$. For surface degradation mechanisms such as corrosion or erosion, only elements at the surface are subject to degradation. Once fully degraded ($d = 1$), the element is removed from the mesh and a new surface has to be assigned. The latter requires an element adjacency map containing element to element connectivity information. Continuum damage mechanics has been applied with stents to predict two main types of corrosion in structural materials under loading: stress induced fatigue cracking or stress corrosion cracking (SCC) and random pitting corrosion (PC).

5.1.3 Stress corrosion of biocorrodible stents

Gastaldi et al. [31, 101, 103] developed a phenomenological finite element framework dedicated to absorbable metal stents by combining

uniform surface degradation with stress-dependent damage evolution and applied this modelling strategy to the optimization of different biocorrodible stent designs. The evolution law of the degradation parameter d is a superposition of uniform surface corrosion d_u and stress corrosion d_{sc} which is dependent of an equivalent measure of internal stress σ_{eq}. Degradation is updated for every time step by using following expressions for the degradation rates $\dot{d}_u$ and $\dot{d}_{sc}$.

$$\dot{d}_u = \frac{\delta_u}{L_e} k_u \tag{5.2}$$

$$\dot{d}_{sc} = \begin{cases} \frac{L_e}{\delta_{sc}} \left(\frac{S\sigma_{eq}}{1-d} \right)^R & \text{if } \sigma_{eq} \geq \sigma_{th} \\ 0 & \text{if } \sigma_{eq} < \sigma_{th} \end{cases} \tag{5.3}$$

Here, L_e is the characteristic element length, δ_u and δ_{sc} are characteristic material dimensions related to uniform and stress corrosion, k_u is a kinetic parameter and S and R are parameters governing stress corrosion. For a detailed description of the stress corrosion model we refer to [30].

5.1.4 Pitting corrosion of biocorrodible stents

Grogan et al. extended the temporal evolution of the damage parameter through the introduction of a randomly distributed element-specific pitting parameter λ_p to account for heterogeneous corrosion [36]. Numerically, the degree of heterogeneity of the corrosion process is described by the probability density function (PDF) of the pitting parameter distribution. The degradation rate is then defined as

$$\dot{d}_p = \frac{\delta_p}{L_e} k_p \lambda_p \tag{5.4}$$

The shape of the PDF for the random variable λ_p follows a Weibull distribution. Once an element is fully degraded, the corresponding element is removed from the FE mesh and the FE surface is updated based on an element adjacency as mentioned in section 5.1.2. Additionally, neighbouring elements inherit the scaled pitting parameter value of the deleted element. This step accounts for pit growth acceleration. Interestingly, the randomized assignment of the pitting parameters can be used to computationally investigate the statistical variability of the configuration of a corrodible stent during degradation. For a more thorough description and for a validation of the stress corrosion model we refer to [35, 36].

5.1.5 Going from an explicit to an implicit finite element integration scheme

Degradation is a per definition a dynamic problem, which suggests the use of an explicit finite element solution technique to model biodegradable stent corrosion. Therefore, the above mentioned models of Grogan et al. and Gastaldi et al. have been implemented to be applicable to the commercial explicit finite element solver Abaqus/explicit (Dassault Systèmes, Providence, RI, USA) [30, 36]. However, the degradation time scale is large compared to time scale at which stent deformation occurs during e.g. stent deployment. Overall, degradation can be considered a quiasi-static process (i.e. inertial effects are small) and the time step needed to integrate the degradation evolution laws is much larger than the stable time increment needed for explicit integration of the finite element problem. This explicit stable time increment Δt follows the relation $\Delta t \propto L_e^{min}\sqrt{\rho/\mu_e}$, where L_e^{min} is the smallest element size, ρ is the density and μ_e represents element stiffness. Because small elements sizes are needed to accurately model surface corrosion the latter results in very short stable time increments for this kind of simulations, thereby increasing the computational cost.

Therefore, this study investigates the use of an implicit finite element solution scheme to model corrosion of biodegradable stents, to increase general applicability of the continuum damage modelling approach and to reduce the computational cost. Also, implicit integration ensures reliable and accurate output of the stresses and deformations. The here suggested framework was implemented as a Fortran material user subroutine UMAT to be compatible with the implicit finite element solver Abaqus/standard (Dassault Systèmes, Providence, RI, USA). The validity of this approach will be shown via a number of proof of concept examples.

5.2 Materials and Methods

5.2.1 Implementation of the corrosion model

This study presents a method to implement the continuum damage approach for surface degradation and the damage evolution laws discussed sections 5.1.2, 5.1.3 and 5.1.4 into a framework compatible with the implicit finite element solver Abaqus/standard to simulate corrosion of an absorbable magnesium stent. Two problems have to be solved to be able to use the continuum damage mechanism in Abaqus/standard. The first issue concerns element deletion: once an

element has fully degraded (i.e. $d \simeq 0$) it has to be removed from the mesh and a newly formed surface has to be assigned. In contrast to Abaqus/explicit, Abaqus/standard does not allow for element deletion. Therefore, we propose to assign a different material to the fully deleted elements, with a very low overall stiffness (i.e. a factor 10^{-8} smaller) compared to the original material. Second, a sufficiently small time step should be selected during the degradation step of the simulation to ensure proper integration of the degradation laws.

A schematic representation of the implementation of the here used corrosion model for magnesium stents is shown in figure 5.1. We used the in-house developed and open-source software pyFormex [94] (based on the programming language python) to generate a high-quality hexahedral mesh of the magnesium stent, see section 5.2.2. The same software was used to generate an adjacency table containing element to element connectivity information. Here, two hexahedral elements are said to be adjacent if they share a common face. The same software was used to seed the initial values of the random pitting parameter used in equation 5.4. Following [36], random pitting parameters are mapped to a Weibull-PDF with the additional constraint that values of λ_p should be between 0 and 1. The Weibull-PDF was therefore adjusted accordingly. $\bar{r}$ being a uniformly distributed random parameter, the corresponding Weibull distributed parameter λ_p was calculated as:

$$\lambda_p = \left[-ln\left(1 - \bar{r}\left(1 - \frac{1}{e}\right)\right)\right]^{\frac{1}{\gamma}} \tag{5.5}$$

The geometrical and connectivity output from pyFormex were then coupled with the FE-solver Abaqus/standard via a user material subroutine UMAT. This Fortran-coded subroutine implements the material behaviour of non-degraded magnesium as linear elastic-plastic with an isotropic plasticity hardening law, modifies the stresses and stiffness tensor according to continuum damage theory and updates the mesh surface and the pitting distribution in case of element deletion. The correctness of the implementation of the plasticity model was verified by comparison with the available isotropic plasticity model in Abaqus. To avoid accessing and modifying the databases externally during the simulation, the data are stored and updated internally inside so-called Fortran common modules and are only imported once i.e. prior to the first increment using the subroutine UEXTERNALDB. Storing connectivity data prior to the actual simulation also allows for parallelization of the computations.

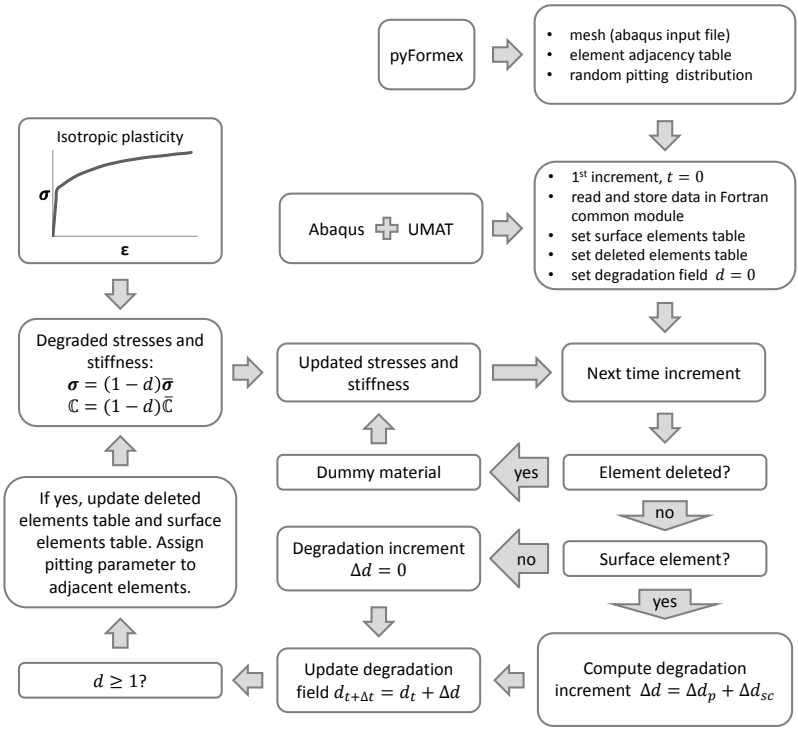

Figure 5.1: Schematic representation of the implementation of the corrosion mechanism using pyFormex and a material subroutine UMAT compatible with Abaqus.

All elements are assigned with a flag indicating whether an element is deleted (1) or not (0). The deletion flag is set to 1 once an element is fully degraded and scaled pitting parameters are assigned to adjacent elements. The same adjacency table is used to update the table indicating whether an element is laying at the corrosion surface.

5.2.2 Finite element geometry

The stent design used in this study is generic though was made to resemble the second generation AMS. General geometrical information (stent shape and dimensions) was taken from literature [41]. The stent consists of 10 zigzag hoops, laterally connected by thin links. When expanded, the stent has a nominal outer diameter of 3 mm and a total length of 11 mm. The stent's strut width and thickness are 0.1 mm and have rounded corners. A high-quality parametric mesh of the stent was made using the previously mentioned software pyFormex by first drawing a planar sketch of a single stent cell path,

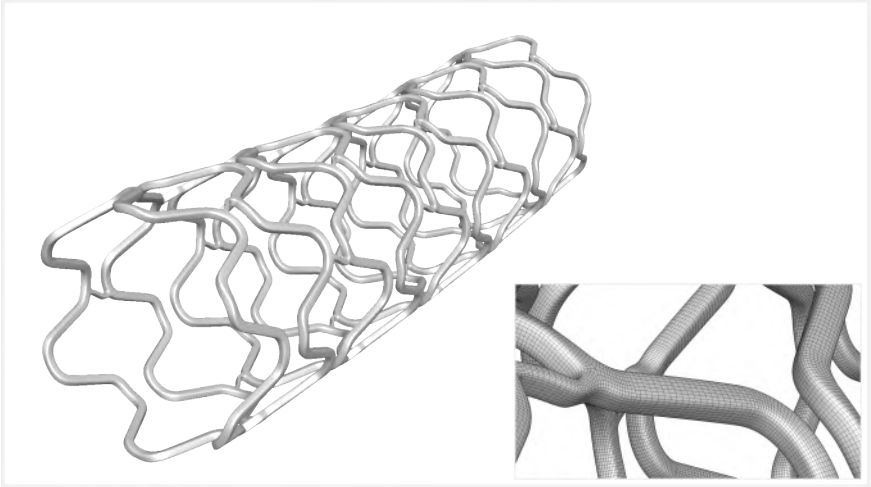

Figure 5.2: Finite element mesh of the absorbable magnesium stent. Included is a zoomed in section showing the individual elements at the surface.

next sweeping the strut cross section along this path and subsequent replication and converting to a cylindrical configuration. The mesh was tailored to have relatively uniformly shaped elements. The final mesh geometry consists of 200500 hexahedral elements with a mean element size of 0.02 mm. The meshed geometry of the stent is shown in its expanded configuration in figure 5.2.

Similarly, 5 different mesh geometries of stenotic blood vessels have been created to serve as input for the simulations. The blood vessel geometries have a length of 20 mm, a global inner diameter of 2 mm, a thickness of 0.3 mm and a central stenotic diameter of 1.2 mm. The stent and vessel configurations are shown in figure ref-fig:stress_stent_vessel. Each vessels was given a different curvature, varying between 0° and 90°. For the sake of simplicity, the blood vessels were assigned with incompressible hyperelastic material properties (neo-Hookean material), where the shear modulus μ was fit to result in a 5% arterial distension for a 40 mmHg (5 kPa) increase of inner pressure.

5.2.3 Deployment of a corrodible magnesium stent inside a stenotic blood vessel

As a proof of the applicability of the implicit FE-solution technique to the modelling of stent corrosion, the methodology and the geometries described in sections 5.2.1 and 5.2.2 were applied to simulate the expansion and subsequent corrosion of a magnesium stent inside 50%

stenotic blood vessels with different degrees of curvature. The meshes and simulation setup can readily be exported from pyFormex into the input file format compatible with Abaqus/standard. Element type C3D8H for incompressible materials was assigned to the blood vessel, whereas the reduced integration element type C3D8R was used for the stent. The stent was first crimped and subsequently expanded inside these vessels by use of cylindrical surfaces (Abaqus element type SFM3D8) interacting with stent and blood vessel through node to surface contact. A surface to surface interaction with friction coefficient 0.1 was applied between stent and blood vessel. The combined stress and pitting corrosion model was then used to model corrosion of the stent. Non-degraded magnesium was set to have Young's modulus $E = 43.5$ GPa, Poisson ratio $\nu = 0.35$ and yield stress $\sigma_y = 172.0$ MPa. Relative material mass loss during corrosion was computed as the ratio of the sum of the volumes of every element multiplied with $1 - d$ with respect to the initial volume of the stent. The stent's loss of mechanical strength was then evaluated through the reduction of the stent's diameter as a function of material mass loss for every case of the stenotic vessel. To account for statistical variability due to the random behaviour of pitting corrosion, each experiment was repeated 8 times for different initial seedings of the random pitting parameter λ_p.

5.3 Results and discussion

5.3.1 Assessing the degradation time increment and validation of the implicit integration scheme

To asses the required time increment to be used during the degradation simulation step, a virtual tensile test was done on a rectangular magnesium sample sheet. The sample was stretched and subsequently subjected to corrosive degradation. The reduction of tensile force was recorded as a function of degradation time and the simulation was repeated for decreasing values of the time step increment. A relatively coarse mesh was used to reduce simulation times. The results are shown in figure 5.3 and indicate that an increment of 1% of the total degradation time is sufficiently small. Therefore, this increment size was used in all simulations.

To check the validity of the implicit FE-solution approach, the pitting corrosion mechanism of Grogan et al. was implemented in both a UMAT and a VUMAT material subroutine to be applicable to the implicit an explicit solvers of Abaqus respectively. The above

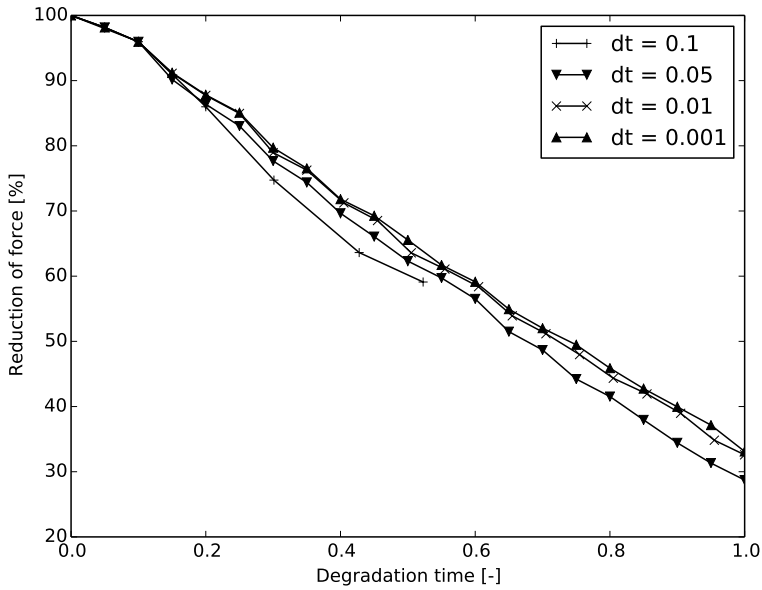

Figure 5.3: Influence of the time step size dt upon integration of the degradation laws.

described experiment was repeated for both types of simulations using fine mesh was used resulting in a total of 32000 elements. Figure 5.4 shows the relative reduction of mean stress over all elements as a function of degradation time. Both simulation results coincide thus establishing the validity of the implicit FE-method.

A more complex geometry representing a stent with two hoops was used to check the proper functioning of the corrosion model. The stent was first expanded and subsequently subjected to increasingly longer degradation times after which the stent's radial strength was obtained by compression with a cylindrical surface as shown in figure 5.5. Here the radial strength was defined as the maximal value of the total reaction force in radial reaction force exerted by the stent on the cylinder surface during compression. Figure 5.5 shows the relative loss of radial strength as a function of material mass loss. The simulations predict well the exponential decay of mean stress for increasing degrees of mass loss. Thanks to the implicit solver, computation times for this simulation containing 38880 elements is less than 30 minutes for 8 cpu's.

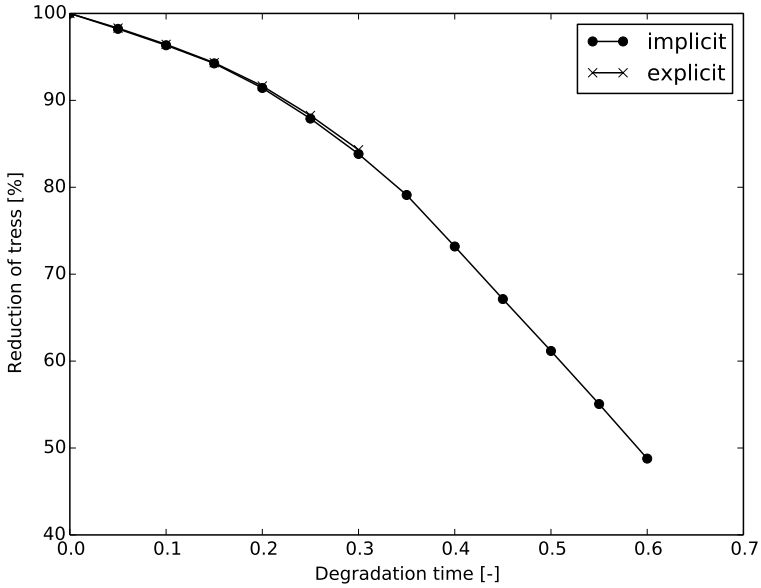

Figure 5.4: Reduction of mean stress inside a rectangular plate subjected to deformation as a function of degradation stress for an implicit and an explicit finite element analysis.

5.3.2 Influence of random pitting distribution

Figure 5.6 illustrates the influence of the pitting parameter distribution upon the heterogeneity of the corrosion process. Shown are the histograms of the λ_p-parameters of a simple rectangular plate subjected to a pitting corrosion simulation for different values of the Weibull-parameter γ. As can bee seen, increasing values of γ result in a more homogeneous distribution of the corrosion process and, in case the remaining parameters in equation 5.4 are left unadjusted, an increase of the overall degradation rate. In this study, a value of of 0.1 was taken for γ. The effect of using a random distribution of material properties is shown in figure 5.7. The graph represents the force needed to maintain a magnesium plate at a fixed stretch as a function of (scaled) degradation time. Included are results for 8 simulations, each having different initial values for the pitting distribution. The force decreases and the statistical deviation of the mean force increases as corrosion is evolving.

5.3.3 Pitting corrosion versus stress corrosion

As a first proof of concept example, we want to quantitatively compare outcomes for the pitting corrosion and stress corrosion evolu-

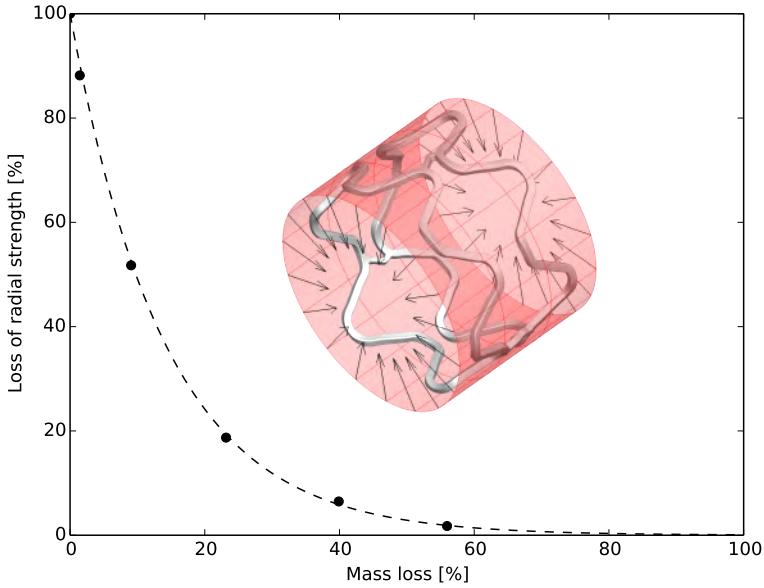

Figure 5.5: Reduction of radial strength of a corrodible stent as a function of material mass loss. Included in the graph is a representation of how the stent radial strenth was obtained.

tion laws. We set up a simple virtual experiment to deploy a stent ring inside an elastic cylindrical tube. As corrosion progresses, the stent's diameter will be reduced due to loss of mechanical strength. Figure 5.7 shows the configurations and the distribution of the degradation field variable at 20% mass loss, where red zones indicate a high degree of degradation. As can be seen, degradation is more uniform and mainly located at the crowns of the stent strut for stress corrosion due to locally high stresses, whereas the corrosion is heterogeneously scattered over the stent's surface for pitting corrosion. The plot shown in figure 5.8 represents the evolution of the stent's outer diameter as a function of material mass loss. For the stress corrosion model, there is a fast onset of material loss of strength followed by decrease in the degradation rate. When the stent is fully loaded by the elastic tube, the stent's internal stresses are high and mainly located at the load-baring crowns of the strut. As the stent corrodes, the diameter of the stent reduces and so does the force acting on the stent by the cylidrical tube and the resulting stresses, which explains the slowing down of the corrosion process.

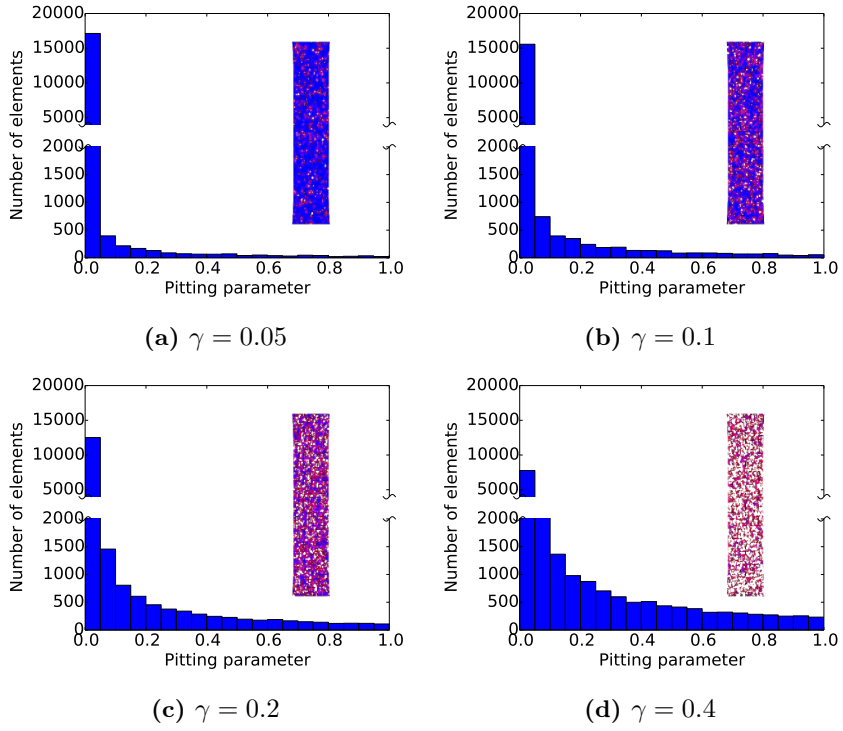

(a) $\gamma = 0.05$ **(b)** $\gamma = 0.1$

(c) $\gamma = 0.2$ **(d)** $\gamma = 0.4$

Figure 5.6: Influence of the pitting parameter distribution upon corrosion of a magnesium plate. Shown are the histograms of the randomly distributed pitting parameters for every element and for different values of the parameter γ of the Weibull-distribution. Included are the simulation results for these plates, with blue indicating little degradation and red indicating almost complete degradation.

5.3.4 Corrosion of a magnesium stent for different stenotic blood vessels

As a second proof concept example, we want to investigate the effect of blood vessel geometry on stent corrosion as described in section 5.2.3. Figure 5.9 displays the internal stress levels inside the stent immediately after deployment and prior to degradation. Zones of high stress (indicated in red) become more dominant for increasing degrees of blood vessel curvature. This is reflected in the overall corrosion rate. Increasing degrees of vessel and stent curvature result in more localized corrosion and subsequent loss of stent diameter and radial strength. A quantative comparison is made in figure 5.10, showing the relative reduction in diameter size as a function of mass loss for every level of vessel curvature.

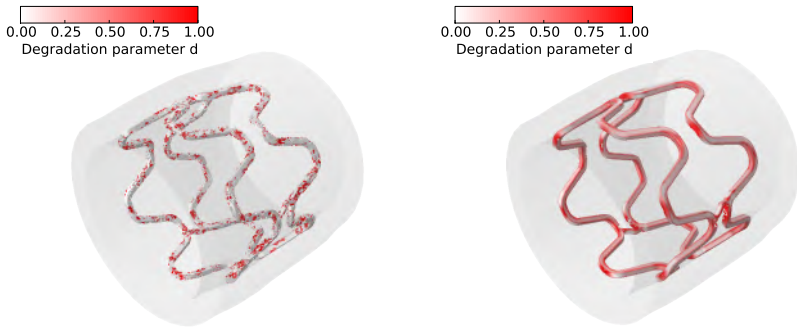

(a) Pitting corrosion model **(b)** Stress corrosion model

Figure 5.7: Comparison between simulation outcomes for a pitting corrosion (left) and a stress corrosion (right) experiment. The stents hoops were expanded inside a hyperelastic tube (transparent) and subsequently subjected to degradation. Results are shown for 20 % mass loss: red zones indicate zones with a high degree of degradation. For the stress corrosion model, degradation is higher in the crowns of the stent struts. For the pitting corrosion model, local weakening of struts is random throughout the stent.

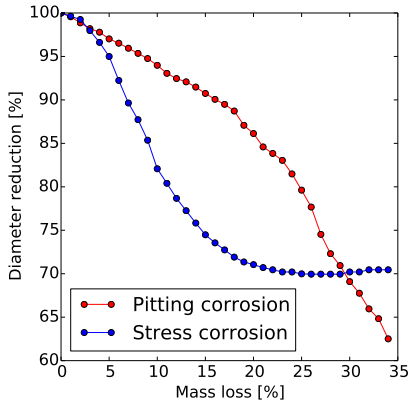

Figure 5.8: Relative reduction of the stent diameter as a function of material mass loss for the FE setup in figure 5.7, for pitting and stress corrosion.

5.4 Conclusions

This paper presents a finite element strategy based on continuum damage mechanics to model corrosion of bioabsorbable magnesium stents using an implicit finite element solver. We were able to implement and combine two models previously proposed by [101] and [36], originally developed for use with and explicit solver, into a material user subroutine UMAT compatible with the implicit FE_solver

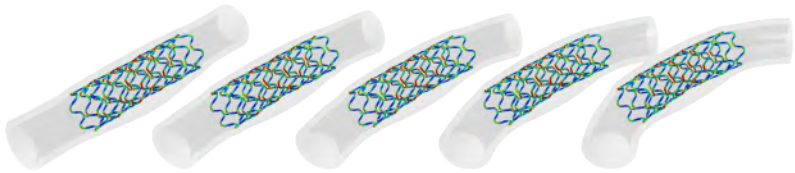

Figure 5.9: Geometrical configuration and distributions of the von Mises stress inside the stents immediately after deployment.

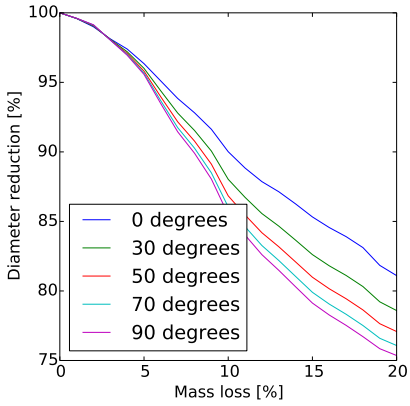

Figure 5.10: Reduction of stent diameter as a function of mass loss for the 5 stent-vessel configurations.

Abaqus/standard. By using an implicit FE solution technique, we can reduce the number of time steps needed to complete the simulation and we obtain accurate and reliable results for the output of stresses and deformation. We found that a increment size of 1% of the total degradation time is sufficiently small to integrate the corrosion mechanism. The here presented framework is able to indicated the different contributions of pitting corrosion and stress corrosion to the rate of degradation for this computational set-up. A high-quality hexahedral mesh of a generic stent was generated using the open-source software pyFormex and combined with geometric models of stenotic blood vessels. The implemented finite element strategy was

successfully used to investigate localized corrosion of stent struts for increasingly complex vessel-stent configurations.

Chapter 6

A finite element strategy to investigate the free expansion behaviour of a biodegradable polymeric stent

Bioresorbable stents represent a promising technological development within the field of cardiovascular angioplasty because of their ability to avoid long-term side effects of conventional stents such as in-stent restenosis, late stent thrombosis and fatigue induced strut fracture. Finite element simulations have proven to present a useful research tool for the design and mechanical analysis of stents. However, biodegradable stents pose new challenges because of their transitional mechanical behaviour. For polymeric biodegradable stents, viscoplastic effects have to be accounted for. This article presents a method to analyse the mechanical behaviour of polymeric bioresorbable stents using an implicit finite-element solver. As an example, we investigate the mechanical behaviour of a commercially available bioresorbable stent. We examine how, due to the visco-elastic properties of the stent material, the balloon deployment rate influences the mechanical integrity of the stent. This chapter was published inside the Journal of Biomechanics [22].

6.1 Introduction

Percutaneous coronary intervention (PCI) with stenting has since its introduction in 1987 grown to become the golden standard to treat coronary artery stenosis, a disease caused by atherosclerosis, which is the local disposition of greasy plaques on the inner side of the arterial wall. PCI is a minimal invasive procedure and replaces the open-chest bypass surgeries, which has led to shorter revalidation times and decreased mortality rates. Conventional durable stents, including both bare metal stents and drug eluting stents (DES), are made of metal alloys such as stainless steel, cobalt-chromium or platinum-chromium and remain permanently inside the human body after placement. However, the need for mechanical support for the healing artery is temporary and beyond the first few months there are potential disadvantages of a permanent metallic prosthesis: excessive neo-intimal tissue growth causes in-stent restenosis and prolonged exposure of the metallic stent surface to the blood stream increases the risk for late stent thrombosis [29]. Despite the fact that repeated percutaneous and surgical revascularization procedures due to restenosis could be reduced with 50 to 70% by the use of DES [65] [93], biodegradable stents, which temporarily support the blood vessel and afterwards fully disintegrate, are gaining much interest. Possible advantages of biodegradable stents include abolished late stent thrombosis, facilitation of repeat treatments to the same site (surgical or percutaneous), restoration of vasomotion and prevention from restenosis [69]. Bioabsorbable stents also have a potentially paediatric role because they allow vessel growth and do not need surgical removal [73]. However, developing biodegradable stents comprises challenges in making a stent that has sufficient radial strength for an appropriate duration, that does not have unduly thick struts, that can be a drug delivery vehicle and where degradation does not generate an unacceptable inflammatory response [50].

Two classes of biomaterials are currently being used in biodegradable stent technology: biodegradable polymers and biocorrodible metal alloys. Polymers can be tailored to have a well-defined degradation pattern but have relatively poor mechanical properties. In contrast, biocorrodible metals such as magnesium alloys have excellent mechanical characteristics but display more complex and less predictive degradation behaviour.

Several biodegradable stents are under development and are subject of clinical trials. The Bioresorbable Vascular Scaffold (BVS) of

Abbott Vascular is a polymeric bioresorbable stent made of poly-L-lactic acid (PLLA) and is coated with an everolimus-eluting poly-D,L-lactic acid (PDLLA) layer [82] [24]. The stent has extensively been tested in the ABSORB clinical trials and has since 2012 been approved with the European CE marking [1]. The main stent representing the class of biocorrodible metallic stents is the AMS-stent of Biotronik that is followed up in the PROGRESS-trials [26][40].

Despite the promising results of these clinical trials, the design of novel biodegradable stents remains a considerable challenge because of the lack of precise engineering modelling tools. Finite element analysis (FEA) has proven to be a valid and efficient method to virtually investigate and optimize the mechanical behaviour of minimal invasive devices such as stents [64] [61] [9] [48]. It can also be combined with patient specific images to plan a surgical procedure or to classify specific devices for different kinds of atherosclerotic lesions [8] [49] [63]. In combination with computational fluid mechanics, the finite element method is able to reveal insight into aspects of drug elution and coating biodegradation [20] [15] [57].

Analysing the mechanical behaviour of biodegradable stents via finite element simulations poses new challenges due to the complexity of the stent materials which display transitional mechanics both in the long term range (polymer degradation, metal corrosion) and the short term range (viscoplasticity in case of polymeric stents). A limited number of FEA-studies on biodegradable stents has been performed. Soares et al. proposed a continuum degradation model which includes the effect of deformation upon the degradation rate of polylactic acid and applied it to biodegradable stents [90]. Bokov et al. investigated the interaction of a biodegradable stent with the vascular wall using FEA [12]. Wu et al. developed a continuum-mechanics based corrosion model for magnesium stents and optimized stent geometry for a better corrosion resistance [101]. A similar mechanical model has been proposed by Grogan et al. for corrosion of magnesium stents. Their work includes an arbitrary Lagrangian-Eulerian approach to model stent erosion [36] [35].

In this article, we will consider the commercially available Absorb BVS (Abbott Vascular, Santa Clara, CA, USA) and as a case study assess its mechanical performance via FEA. In particular, we want to investigate the influence of the deployment rate during stent balloon expansion. Because of the high degree of viscoplasticity of the polymeric stent material, the expansion rate might have an important influence on the mechanical performance and integrity of the deployed stent. To be able to do so, a sufficiently representative material

model was selected and its parameters were fitted to available experimental data. The commercial finite element solver Abaqus/standard (Dassault Systems Simulia, Providence, RI, USA) was used to solve the quasi-static stent deployment simulations. To overcome part of the contact problems which are inherent to this type of simulation, a simplified balloon model was used. The level of internal stresses and the degree of post-dilational recoil will be compared for a direct and a stepwise deployment procedure.

6.2 Methods

This section subsequently describes the use of a cylindrical anisotropic balloon model, the generation of a finite element mesh for the stent and the implementation of a hyperelastic-viscoplastic material for PLLA to be combined within an implicit finite element framework to model the balloon deployment of the bioresorbable BVS stent.

6.2.1 Balloon model

Since balloon expansion of a stent is basically a quasi-static problem (i.e. dynamic inertia effects do not play an important role), the obvious way is to use an implicit finite element solution technique. However, because balloon-stent deployment is dominated by complex non-linear contact problems including stick/slip frictional sliding, an explicit finite element procedure is often preferred. This however requires relatively high computational expenses because of the small time steps that are needed to fulfil the quasi-static criterion. We used a different strategy: an implicit solution technique was used for the FE problem, but the contact problem was largely simplified via the use of a cylindrical balloon with anisotropic hyperelastic material properties as proposed by Kiousis et al. [53]. Here, the material orientations are aligned with the longitudinal and circumferential directions of the balloon. The main idea is that the cylindrical balloon material should initially behave soft, to mimic the unfolding of the balloon. Once the balloon has reached its nominal diameter, an internal deformation threshold is exceeded and the balloon becomes much stiffer. Fig. 6.1 shows a segmented micro-CT scan of the crimped BVS-stent and its balloon illustrating the complexity of the folded structure of the balloon. On the right is a simplified representation of the balloon used in this study.

For a general description of the continuum mechanical framework we refer to [53]. In this model, the hyperelastic energy density function $\bar{\Psi}$ is split into an isotropic part $\bar{\Psi}_{iso}$ and an anisotropic part

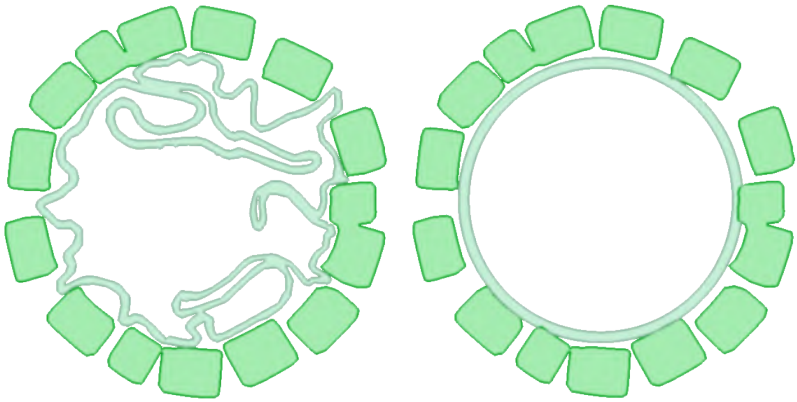

Figure 6.1: Left: segmented micro-CT scan of the crimped BVS-stent struts (green) and its folded balloon (blue). Right: simplified balloon geometry used in the finite element simulations.

$\bar{\Psi}_{aniso}$ that depend on the first invariant of deformation $\bar{I}_1$ and two pseudo-invariants $\bar{I}_\theta$ and $\bar{I}_z$ of deformation in the circumferential and longitudinal direction respectively.

$$\bar{\Psi}_{iso}(\bar{I}_1) = c_{10}(\bar{I}_1 - 3) + c_{20}(\bar{I}_1 - 3)^2 \tag{6.1}$$

$$\bar{\Psi}_{aniso}(\bar{I}_\theta, \bar{I}_z) = \bar{\Psi}_\theta(\bar{I}_\theta) + \bar{\Psi}_z(\bar{I}_z) \tag{6.2}$$

$$\bar{\Psi}_i(\bar{I}_i) = \begin{cases} \frac{k_i}{n}\left(\bar{I}_i - I_i^0\right)^n & \text{if} \quad \bar{I}_i \geq I_i^0 \\ 0 & \text{if} \quad \bar{I}_i < I_i^0 \end{cases} \quad i = \theta, z \tag{6.3}$$

Isotropic elasticity is governed by the parameters c_{10} and c_{20}. The term $c_{20}(\bar{I}_1-3)^2$ was added to the original model presented by Kiousis et al. to improve numerical stability of the implicit FE problem (see Section 6.2.2). The material parameters $k_{\theta,z}$, $I^0_{\theta,z}$ and n determine the stiffness of the balloon in the circumferential and longitudinal direction.

If we consider the balloon to be a thick walled straight cylindrical tube, fixed at its ends in the longitudinal direction, then it is straightforward to find an analytical relationship between the radial distension and the pressure drop ΔP over the cylindrical wall for the

above hyperelastic energy function through the use of the following integral.

$$\Delta P = \int_{x_1}^{x_2} \frac{\partial \bar{\Psi}/\partial x}{1-x}\,\mathrm{d}x \tag{6.4}$$

Here x represents the ratio of the squares of the radial position of a material point inside the cylindrical wall in the current (r) and reference (R) configuration, $x = r^2/R^2$. The invariants become $\bar{I}_1 = x + x^{-1}$, $\bar{I}_\theta = x$ and $\bar{I}_z = 1$. $x_1 = r_1^2/R_1^2$ and $x_2 = r_2^2/R_2^2$ correspond to positions at the inner and outer wall. Because of incompressibility of the material, the identity $x_2 = 1 + R_1^2/R_2^2(x_1 - 1)$ yields. Using the integral in equation 6.4 we can fit the balloon material constants to manufacturer data for given values of R_1 and R_2 (see section 6.3.1).

6.2.2 Ensuring numerical stability for the balloon model

The exact analytical solution of the pressure difference ΔP (see equation 6.4) for a thick walled cylinder for the Kiousis balloon model can be written as follows, by splitting ΔP into an isotropic part ΔP_{iso} and an anisotropic part ΔP_{aniso}.

$$\Delta P = \Delta P_{iso} + \Delta P_{aniso} \tag{6.5}$$

The respective solutions for the isotropic (with $c_{20} = 0$, $I_z^0 = 1$ and $n = 3$) and the anisotropic part are

$$\Delta P_{iso}(\lambda) = c_{10}\left[\ln\left(\frac{1+\alpha}{\lambda+\alpha}\right) - \ln\left(\frac{1}{\lambda}\right) + \frac{1+\alpha}{\lambda+\alpha} - \frac{1}{\lambda}\right] \tag{6.6}$$

$$\Delta P_{aniso}(\lambda) = \begin{cases} 0 & \text{if} \quad \lambda \le I_\theta^0 \\ \Delta P_{aniso}^a(\lambda) & \text{if} \quad I_\theta^0 < \lambda < (1+\alpha)\, I_\theta^0 - \alpha \\ \Delta P_{aniso}^b(\lambda) & \text{if} \quad (1+\alpha)\, I_\theta^0 - \alpha \le \lambda \end{cases} \tag{6.7}$$

Here, the full expressions of ΔP_{aniso}^a and ΔP_{aniso}^b can be written as follows.

$$\Delta P_{aniso}^a(\lambda) = k_\theta \left[\left(I_\theta^0 - 1\right)^2 \ln\left(\frac{\lambda - 1}{I_\theta^0 - 1}\right) + \frac{1}{2}\left(\lambda^2 - I_\theta^{0\,2}\right) - \left(2I_\theta^0 - 1\right)\left(\lambda - I_\theta^0\right) \right] \tag{6.8}$$

$$\Delta P^{b}_{aniso}(\lambda) = k_\theta \left[\left(I^0_\theta - 1\right)^2 \ln(1+\alpha) + \frac{1}{2}\left(\lambda^2 - \left(\frac{\lambda+\alpha}{1+\alpha}\right)^2\right) - \frac{\alpha}{1+\alpha}\left(2I^0_\theta - 1\right)(\lambda - 1)\right] \tag{6.9}$$

Here, we have set $\lambda = r_1^2/R_1^2$ and $\alpha = R_2^2/R_1^2 - 1$. The main problem with stability in Abaqus/standard arises when $\lambda < I^0_\theta$, when the anisotropic part of the material is not yet contributing to material stiffness. In this zone, for a simple neo-Hookean expression of the isotropic part, the diameter of the cylinder will rapidly increase for a small increase in pressure. For a non fully incompressible material, the pressure difference will even decrease for an increasing diameter. This means that there are multiple solutions of diameter displacement for a given internal balloon pressure state which causes an unstable implicit finite element solution. This problem can be solved in two ways. First, instead of increasing balloon pressure, the diameter of the balloon can be expanded by directly increasing the volume of the balloon by making use of the 'surface cavity'-option of Abaqus/standard. This requires however the creation of an extra surface mesh defining the inner volume of the balloon and the definition of a fluid exchange mechanism. The second option is to slightly modify the original expression of Kiousis et al. by adding a second order term to the isotropic material behaviour, so that the diameter/pressure curve for the balloon will be monotonically increasing. Because of ease of implementation, the second approach has been followed in this study.

6.2.3 Poly-L-lactic acid stent model

6.2.3.1 Stent geometry

The 2$^{\text{nd}}$ generation ABSORB BVS has a typical stent shape consisting of in-phase zigzag hoops linked by bridges. The scaffold has thick struts (150 µm) [32] to compensate for the relatively poor mechanical properties of PLLA. A reversed engineering approach was followed to construct the finite element geometry of the stent. High resolution (voxel size 2.5 µm) micro-CT based image data were used as input to make a segmented 3D-reconstruction of the BVS using the commercial software Mimics (Materialise, Belgium). The 3D-geometry has subsequently been imported into pyFormex [94], in-house developed open source software, to obtain the stent's characteristic dimensions

(strut width, thickness and length etc.). The software pyFormex has also been used to generate a high-quality hexahedral mesh of the stent in its non crimped configuration. An initial simulation was performed by shrinking of a cylindrical surface (consisting of SFM3D8 elements, cfr. Abaqus Manual) contacticting with the outside of the stent (using a node to surface contact approach), resulting in the stent's geometry in the crimped configuration. Also strut-to-strut self-contact was taken into account, using a surface to surface contact approach. This preliminary analysis was done to obtain the stent's initial internal stresses and to establish stent-balloon contact and stent-stent self contact. The overall procedure is schematically represented in Fig. 6.2.

6.2.3.2 Stent material

Poly-L-lactic acid (PLLA), a member of the aliphatic polyesters, degrades via simple hydrolysis of the ester bonds and does not require enzymes to catalyse this hydrolysis. The high molecular weight PLLA backbone of the BVS stent is a semicrystalline polymer displaying rate-dependent visco-plastic and hyperelastic material mechanics. Such complex material behaviour limits the use of simple material models such as linear elasticity and isotropic metal plasticity. An advanced material model that is sufficiently able to capture the material characteristics of PLLA was taken from literature as presented by Bergström et al. [11] [28]. A schematic overview of the rheology of this mechanical model is shown in Fig. 6.3. The model consists of an elastic Langevin-type spring in parallel with a visco-elastic plastic damper. The Kirchhoff stresses $\boldsymbol{\tau}$ are the sum of the stresses $\boldsymbol{\tau}_\alpha$ in the visco-plastic system and $\boldsymbol{\tau}_{\mathcal{L}}^{iso}$ in the elastic system.

$$\boldsymbol{\tau} = \boldsymbol{\tau}_\alpha + \boldsymbol{\tau}_{\mathcal{L}}^{iso} \tag{6.10}$$

The mechanical behaviour of the hyperelastic Langevin-type spring, and thus its internal stresses $\boldsymbol{\tau}_{\mathcal{L}}^{iso}$, are fully determined by its free energy function $\bar{\Psi}$:

$$\bar{\Psi}(\lambda_r) := \mu N \left(\lambda_r \mathcal{L}^{-1}(\lambda_r) + \ln \frac{\mathcal{L}^{-1}(\lambda_r)}{\sinh \mathcal{L}^{-1}(\lambda_r)} \right) \tag{6.11}$$

Here, the material parameters μ and N represent the shear modulus and the chain rank. $\lambda_r = \lambda/\sqrt{N}$ is the relative stretch with λ the local stretch $\lambda = \bar{I}_1/3$. $\mathcal{L}(x) = \coth(x) - 1/x$ is the Langevin function.

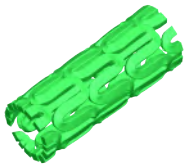

(a) Segmented micro-CT reconstruction of the BVS 3.5 mm stent.

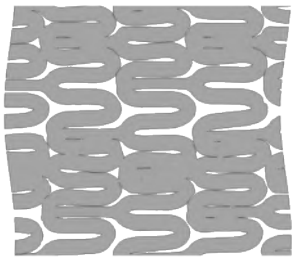

(b) Unrolling of the stent using pyFormex to obtain the stent dimensions.

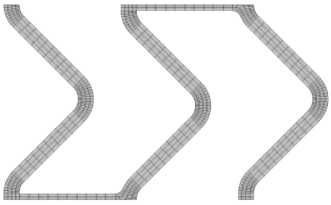

(c) Construction, meshing and replication of the stent base pattern using pyFormex.

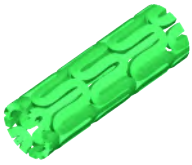

(d) An initial simulation is needed to obtain the stent geometry in its crimped configuration.

Figure 6.2: Reversed engineering procedure to generate a high quality mesh of the BVS3.5 stent.

In Fig. 6.3, the visco-plastic part is modeled as a visco-plastic dashpot and a linear elastic spring system. The governing material parameters are the elastic modulus E and the Poisson modulus ν for the elastic spring, and the plastic hardening parameter h, the viscosity η and the yield stress σ_y for viscoplastic contribution. For the implementation of the visco-plastic part of the material model, a corotational formulation was used. The material model was implemented as a fortran subroutine 'UMAT' to be compatible with the finite element solver Abaqus/standard. The set of material parameters $\{\mu, N, E, \nu, h, \eta, \sigma_y\}$ was fit by comparison of experimental tensile test data with virtual tensile tests on dumbbell specimens (see section 6.3.2).

6.2.4 Virtual balloon inflation of the BVS

The product manual of the Absorb BVS mentions the following instructions for use [2].

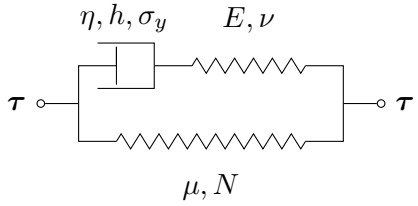

Figure 6.3: Mechanical equivalent of the constitutive material model for PLLA. In the viscoplastic branch, the parameters E and ν represent the modulus of elasticity and the Poisson ratio, h and σ_y account for plastic hardening and yielding, and η is a viscosity parameter. μ and N are the Langevin-network parameters that determine the mechanical behaviour of the hyperelastic branch.

> Deploy the scaffold slowly, by pressurizing delivery system in 2 atm increments, every 5 seconds, until scaffold is completely expanded. Maintain pressure for 30 seconds. If necessary, the delivery system can be repressurized or further pressurized to ensure complete apposition of the scaffold to the artery wall.

If a pressure of 12 atm is required, stent deployment takes more than one minute. We wished to gain a better insight into this instruction for use by virtually repeating the above described procedure combining the finite element stent model obtained in section 6.2.3 with the balloon model from section 6.2.1. The stent was first crimped onto the balloon and a node-to-surface contact interaction was established between the inner surface of the stent and the outer surface of the balloon. A uniform pressure load was applied on the inner surface of the balloon to force inflation. During a first simulation, pressure was linearly increased to a value of 14 atm over a timespan of 5 seconds. Immediately after deployment, pressure was gradually removed. A second simulation was performed, this time according to the instructions for use of the BVS. Balloon pressure was stepwise increased using 2 atm increments. Each increment has a timespan of 1 second after which pressure was maintained for 5 seconds. Prior to deflation, pressure was maintained for another 30 seconds. The outcome of these simulations is discussed in section 6.3.3.

6.3 Results and discussion

This section discusses the fitting of the material models for the balloon and PLLA to experimental data and the application of the developed finite element framework to the balloon inflation to the Absorb BVS.

6.3.1 Fit of balloon model

We set the material constants c_{10} and c_{20} to 0.5 MPa and 0.05 MPa to ensure sufficient compliance of the balloon in the unfolding region. The exponential factor n was set to 3 and the material parameters in the longitudinal direction were fixed as $k_z = 1000.0\,\text{MPa}$ and $I_z^0 = 1.0$. For the balloon, an initial outer diameter of 1.0 mm was taken with an initial wall thickness of 0.037 mm.

The analytical pressure-distension relation was subsequently fit to pressure-diameter manufacturer data for the Absorb stent [2] to obtain the remaining material parameters k_θ and I_θ^0 which were found to be 0.121 MPa and 9.09. The material model was implemented in the Fortran subroutine uanisohyper_inv to be compatible with the Abaqus/standard FE-solver. The balloon was modelled as a solid incompressible cylinder using hybrid solid C3D8H elements. A fit of the cylindrical balloon model pressure/outer diameter curve to the manufacturer data of the Absorb BVS3.5 mm stent is shown in Fig. 6.4.

6.3.2 Fit of PLLA model

A series of tensile tests were performed on dumbbell specimens made by laser cutting out of an extruded PLLA tube (however not from Absorb tubing). Laser cutting and tensile testing were done by the company Admedes (Pforzheim, Germany). The tests were performed at strain rates of 1 mm/min, 10 mm/min and 100 mm/min. These tensile tests have not been performed at body temperature and as such do not represent the actual mechanical behaviour of PLLA at the site of delivery. However, within this proof of concept study, the tensile testing experiments form a good basis for the fit of the PLLA material model. The solid black lines in Fig. 6.5 show the outcome of the tensile tests. The tensile test were then repeated virtually to manually fit the material properties $\{\mu, N, E, \nu, h, \eta, \sigma_y\}$ from the model presented in section 6.2.3.2. The simulation results are represented by dashed lines in Fig. 6.5. The phenomenon of 'necking' which occurs uppon the plastic deformation of PLLA was also reflected in the virtual tensile tests.

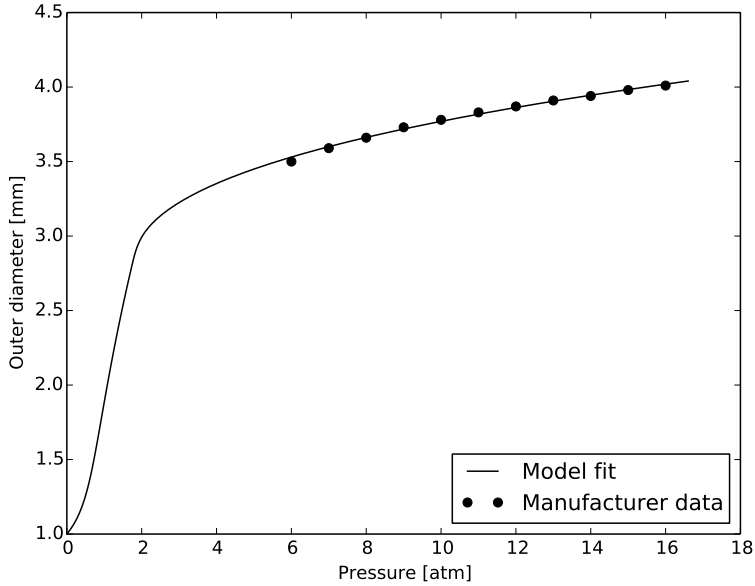

Figure 6.4: Fit of the cylindrical balloon model to the BVS 3.5 mm stent pressure-diameter manufacturer data

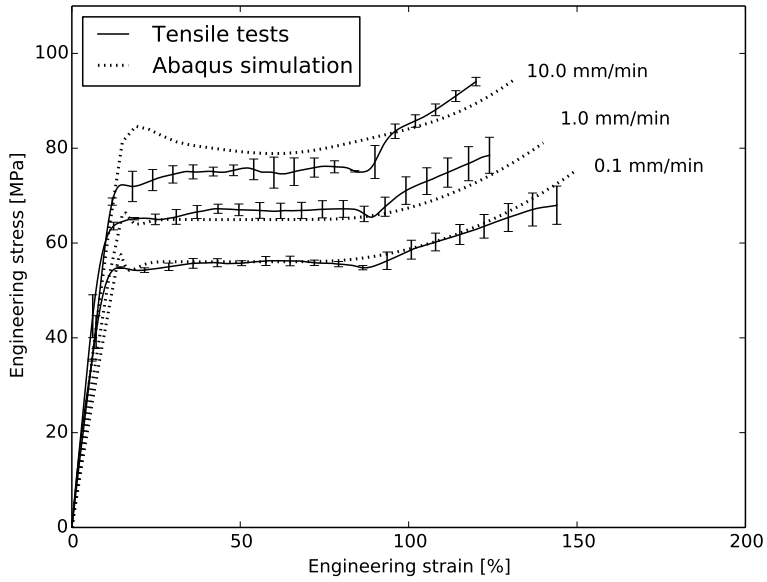

Figure 6.5: Experimental data from tensile tests on dumbbell specimens cut from PLLA tubes, performed at different strain rates, and fit of the PLLA material model through simulations.

6.3.3 Free stent balloon expansion simulation

Due to symmetry of the balloon-stent configuration, only one sixth of the geometry of the stent and balloon were used in the simulations. This geometrical reduction would no longer yield in more complex cases such as a configuration including a blood vessel, however, in this case it will not affect the outcome of the simulations and the use of symmetry reduction is justified. Prior to the actual simulations, a mesh sensitivity study was done for the stent to establish the required number elements, by expanding it with a cylindrical surface by comparing the outcome of the simulations (stent geometry and maximal stress levels) for increasingly finer meshes, until the results did not change significantly. A stent mesh consisting of 10464 linear hybrid brick (C3D8H) elements was found to give accurate results (e.g. a further increase to 35000 stent elements reduced the maximal value of the maximal principal stress with less than 0.1%). The nodes lying in symmetry planes were fixed in the tangential cylindrical direction. Node to surface contact was used to model balloon-stent contact interaction, using a friction coefficient of 0.1 . By using an implicit finite element solution technique, calculation times for these simulations could be kept lower than one hour for 8 cpu's. Fig. 6.6 gives the configuration of the stent at different time points during the balloon inflation procedure. At a pressure of 4 atm, the stent takes the typical dogbone shape [21]: the implemented cylindrical balloon model is thus very well able to capture this phenomenon, which would be absent in the case of a displacement driven simulation (e.g. using surface elements). In the interval from 8 atm till 14 atm, the balloon is fully inflated and the dogbone shape has disappeared. When balloon pressure is reduced to zero, the stent diameter slightly decreases due to elastic recoil.

6.3.3.1 Distribution of stresses

Fig. 6.7 shows the distribution of the maximum principal stresses inside the stent at maximal balloon pressure and at the final relaxed configuration, for both the direct and stepwise balloon inflation procedures. In Fig. 6.7a and Fig. 6.7b the red zones indicate stresses higher than 100 MPa. It is clear that high stress levels are less widespread in case a stepwise inflation procedure is applied. The same conclusion holds in the relaxed configuration, as shown in Fig. 6.7c and Fig. 6.7d. A more quantitative comparison is made in Fig. 6.8. The lower half of the plots depicts the application of the balloon pressure for the direct (dashed line) and the stepwise inflation procedure (full line). The upper half of the plot shows the evolution of the maximal value of the

maximum principal stress over all integration points during both simulation steps. The highest values of the internal stresses are reduced with over 20% when a stepwise balloon pressure increase is used. For the relaxed configuration, reduction of stress is less extensive.

(a) Pressure 0 atm - balloon and crimped stent before inflation.

(b) Pressure 4 atm - after maintaining pressure for 5 seconds.

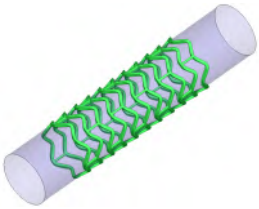

(c) Pressure 14 atm - after maintaining pressure for 30 seconds.

(d) Pressure 0 atm - fully deployed stent.

Figure 6.6: Different configurations of stent and balloon during the stepwise inflation procedure.

6.3.3.2 Final diameter of the stent

The viscoplasticity of the material affects the degree of elastic recoil and the final diameter of the stent. The simulation output for the outer diameter of the stent is given in Fig. 6.9. The upper part of the graph plots the outer diameter of the stent at a point in the distal D_d and the central D_c portion of the stent. The degree of dogboning, defined as $(D_d - D_c)/D_d$ [REF], is plotted in the middle part of Fig. 6.9. According to this simulation, the final diameter of the stent only slightly benefits (a 4% increase) from a stepwise inflation procedure. The rate of the balloon pressure increase does not seem to influence the degree of dogboning.

6.4 Conclusions

This study shows that is possible to use an implicit finite-element solver to model stent balloon expansion. To our knowledge, until now, only explicit solvers have been for this purpose. The use of an

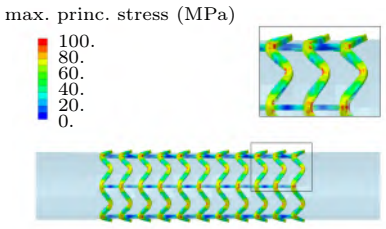

(a) Maximal inflation, direct inflation procedure. The red zones exceed 100 MPa.

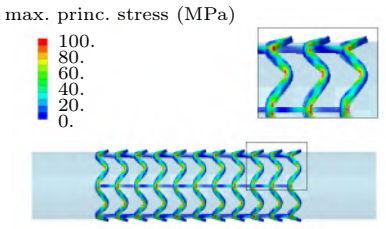

(b) Maximal inflation, stepwise inflation procedure. The red zones exceed 100 MPa.

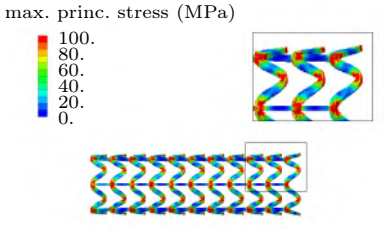

(c) Final configuration, direct inflation procedure. The red zones exceed 40 MPa.

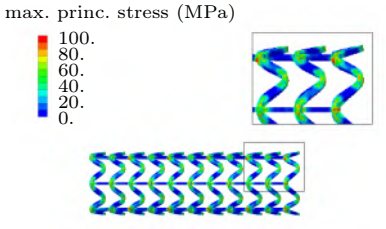

(d) Final configuration, stepwise inflation procedure. The red zones exceed 40 MPa.

Figure 6.7: Comparison of the distribution of the maximum principal stress inside the BVS 3.5 mm for the direct and stepwise inflation procedure at full inflation and the final relaxed configuration.

implicit solver benefits the accuracy and the reliability of the outputted stresses. It avoids dynamic inertia effects and therefore simplifies the interpretation of the simulation outcomes. We were able to use an implicit solver through reduction of the contact problem, by using a cylindrical balloon model as proposed [53]. The in this study presented implicit finite element solution strategy to model free balloon inflation of stents using a cylindrical balloon model and an anisotropic balloon material reflects well some of the stent's expansion characteristics such as the dogboning phenomenon.

The short term effects of stent deployment rate upon the stents mechanical integrity due to viscoplastic effects of the stent material were investigated. Whereas focus within the field of modeling of biodegradable stents has mainly been lying on implementing degradation mechanisms, this article reveals insights in the direct mechanical behaviour of polymeric stents. The implementation of a combined

visco-plastic hyperelastic material model is required to obtain insight into to the instructions for use of the Absorb BVS stent. Although the here presented material model was fitted to very preliminary experimental data, and should thus not be taken as representative for the actual mechanical behaviour of PLLA, the material model gives a qualitative indication of how a gradual expansion procedure reduces the build-up of internal stresses and consequently the risk for strut fractures. Possibly, it might also reduce the degree of elastic recoil after stent deployment.

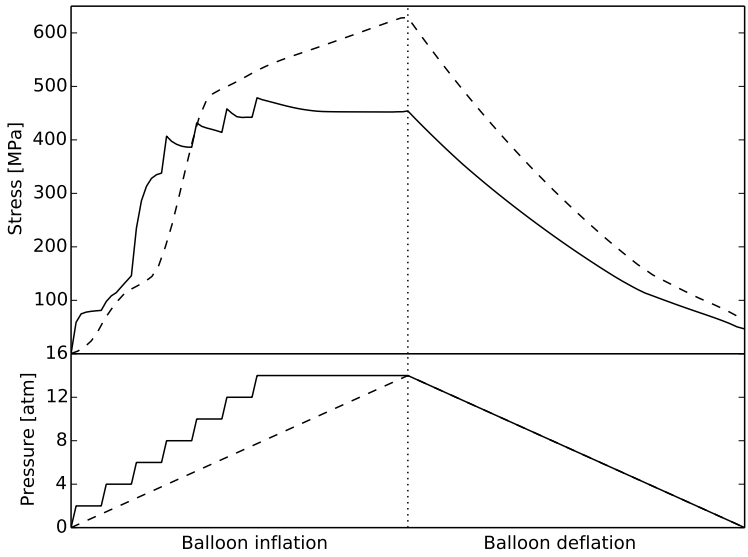

Figure 6.8: Evolution of the maximal maximum principal stress for all integration points (upper part). The lower part of this graph represents the application of pressure during the simulation. Values for stepwise inflation are represented by the full line, values for direct inflation are represented by the dashed line.

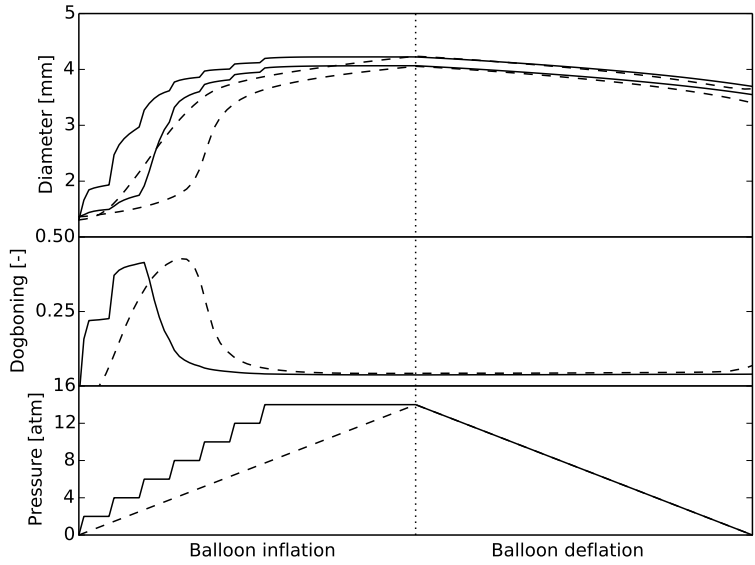

Figure 6.9: Evolution of the outer diameter at a distal and central portion of the stent (upper part). Evolution of the degree of dogboning (central part). The lower part of this graph represents the application of pressure during the simulation. Values for stepwise inflation are represented by the full line, values for direct inflation are represented by the dashed line.

Four

Conclusions

Chapter 7

Conclusions

7.1 Discussion

Finite element modelling has proven to be a valuable and time efficient tool to investigate the mechanical behaviour of minimally invasive biomedical devices such as stents. Computer models allow to obtained detailed insights into the mechanics of stents, especially for loading conditions and configurations which cannot be assessed via *in vitro* testing. By combining validated finite element models for stents with patient specific image data, models can be built that are able to simulate *in vivo* interaction of a specific device with the surrounding tissues. Finite element modelling has become a golden standard technique for investigating the feasibility and performance of new metallic stents and to optimize their geometry. The recent advent of biodegradable stents has posed new challenges for computer modelling because of their complex mechanical and degradational biomaterial backbone material behaviour. The research presented in this thesis aimed to contribute to the general understanding of the mechanical behaviour of both biodegradable polymeric and corrodible metallic stents via computer simulations.

Part I of this thesis gave an introduction to the general idea behind biodegradable stents. The main purpose of a degradable scaffold is to avoid long term complications of permanent stents such as in-stent restenosis and more importantly late in-stent thrombosis. An ideal biodegradable stent combines sufficient radial support during the arterial healing period with biocompatibility and a gradual loss of material mass and degradation products. We saw that both bioresorbable polymers and biocorrodible metal alloys are candidate materials for biodegradable stents, where polymers show excellent biocompatibility though poorer mechanical properties. Metal alloys instead have initially good scaffolding abilities – comparable to conventional stents – but display unpredictable degradation behaviour. Development of biodegradable stents has moved ahead during the last decade thanks to the availability of novel biomaterials, and some stents such as the Bioresorbable Vascular Scaffold (BVS) of Abbott and the Absorbable Metal Stent (AMS) of Biotronik are now entering the biomedical device market. By applying more biodegradable stents in clinic and by expanding the indications for use, more data will become available, possibly showing the advantages of a biodegradable stent over drug eluting stents (DES).

The fundamentals of solid mechanics and constitutive material modelling have been briefly explained in chapter 2. These theoretical concepts lead to the understanding of finite element modelling and its

combination with continuum damage mechanics to simulate material degradation. To be able to use complex models for e.g. polymer viscoplasticity or corrosion of magnesium alloys, Fortran-coded material subroutines had to be implemented, which requires an understanding of the concepts explained in chapter 2.

A literature overview was given of the limited number of studies that have proposed strategies to model degradation of biodegradable stents. Soares et al. have given a mathematical description of the coupling between deformation and degradation rates of polyesters such as poly-L-lactic acid (PLLA). This approach was based on the finding that absorbable PLLA sutures degrade faster when they are stretched. The models indicate faster degradation of the bioresorbable polymeric stents in the regions of high deformation (such as the crowns of the stent), however there is little experimental proof or validation for this simulated result. The available literature on modelling of biocorrodible metal stents is more extensive with Grogan et al. and Gastaldi et al. as main authors. Most of these models are based on a continuum damage mechanics approach, which couples the degradation laws with the overall mechanical constitutive laws of the corrodible material. The work of Grogan et al. focusses on pitting corrosion while Gastaldi et al. have investigated stress corrosion cracking.

Part II presents a methodology to characterize the corrosion behaviour of biodegradable magnesium alloy stents via *in vitro* degradation and mechanical experiments. These *in vitro* models allow for efficient and real-time collection of degradation data, but cannot be taken as a reference for actual *in vivo* corrosion of magnesium because of the absence of an inhibiting layer of adhesive proteins and cells. Instead they do provide the necessary data to prove the applicability of finite element modelling tools in predicting the mechanical behaviour of biocorrodible stents.

The resulting experimental data provide input for obtaining appropriate material constants used in the constutitutive models presented in part III of this thesis. Both chapters in this part have been submitted and published as scientific papers in the international journals *Journal of Biomechanics* and *Annals of Biomedical Engineering*. The first paper describes how finite element modelling can be applied to investigate the viscoplastic mechanical properties of polymeric stents. The results from this paper show that the deployment rate of stent balloon expansion has a high impact on the level of internal stress inside the absorbable scaffold and subsequently on its mechanical integrity. The second paper focussed on modelling

of biocorrodible magnesium alloy stents. An implicit finite element strategy has been proposed which allows to apply existing models for stent surface degradation in a computationally efficient way, with a high reliability of the stress and deformation output.

7.2 Limitations

The here developed finite element strategies represent a framework that can be applied to the simulation of stenting using biodegradable devices, and offer a methodology to set both the stent's non-degraded material characteristics and degradation behaviour. However, the validity of these models relies heavily on the input of available mechanical and degradation test data. Mechanical characterization should be done using testing conditions that resemble the in-vivo situation. Tensile testing must therefore be carried out at body temperature (37°C). This condition was fulfilled while testing the PLLA-dumbbell specimens in Chapter 6, however not to test the magnesium alloy samples used in Chapter 4. This limitation can be considered to be acceptable because the mechanical properties of polymers are usually much more temperature dependent than those of metal alloys. The main limitation with respect to experimental input is in the degradation data. The degradation experiments carried out during this research and the majority of the experimental data available from literature are based on *in vitro* testing. Although these experiments provide an insight into the degradation mechanisms, actual *in vivo* degradation rates can be very different. As mentioned in Chapter 4, many biological factors such as enzymes, deposition of proteins and cells on the stent surface etc. influence the degradation rate. Since degradation rates are quasi impossible to assess *in vivo*, this research field would benefit much from *in vitro* test bench setups that are able to mimic the conditions inside the human body.

The current research has mainly focussed on coupling stent geometries with material models that sufficiently capture the mechanical response of biodegradable stents. To model degradation, these mechanical models have been coupled with phenomenological degradation models via continuum damage mechanics. These models are based on the overall macroscopic behaviour of the biomaterials but do not take into account the micro and nano-scale physical mechanisms that govern degradation. This means that material and degradation constants have to be defined for every separate degradable polymer or metal alloy. In future, physical degradation models could be defined that are able to predict degradation rates based on e.g.

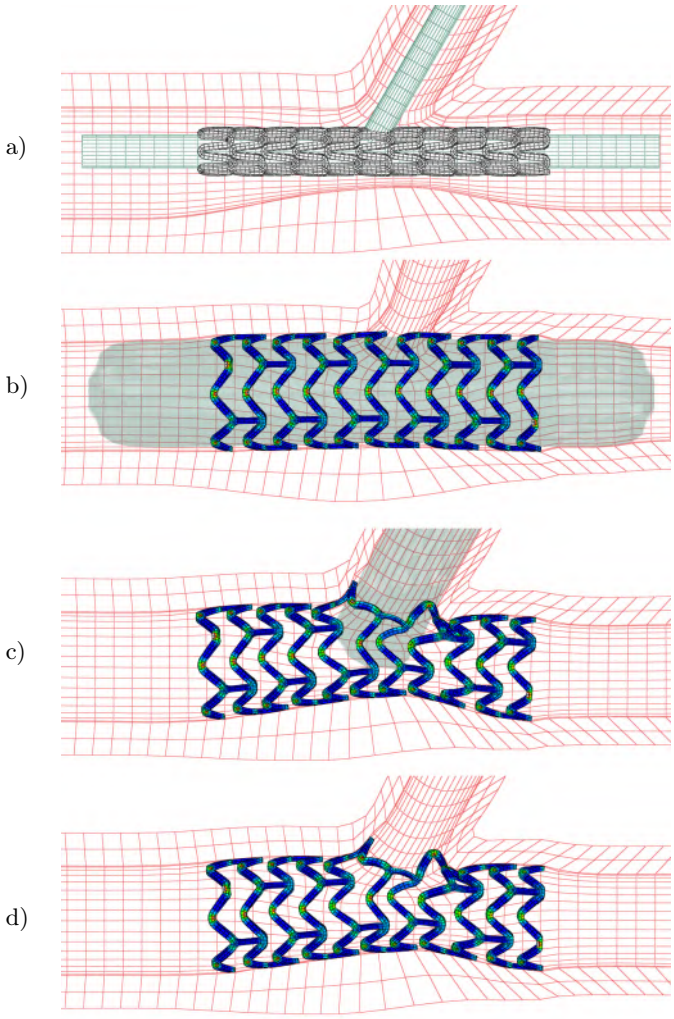

Figure 7.1: Simulation of the deployment of a bioresorbable stent inside a bifurcated blood vessel, using the FE-solver Abaqus/standard. The stent FE-geometry was modelled to resemble the Absorb BVS1.0 device. The bifurcated blood vessel geometry has hyperelastic material properties resembling those of the silicone material used with 3D-printing. Figure a) shows the initial configuration of the crimped stent. Two balloons were modelled as deformable cylinders with anisotropic hyperelastic material properties (cfr. Chapter 6, Section 6.2.1). First, the main balloon on which the stent was crimped is expanded (Figure b)). Second, the smaller balloon in the bifurcation side branch was expanded to push the struts that cover the side branch entrance aside (Figure c)). Figure d) shows the final geometry of the expanded absorbable stent.

the molecular weight of a give polymer or the alloying composition of a biocorrodible metal. These microscale models will then determine the macroscale degradation behaviour, which can in turn be coupled with the biomaterial mechanical behaviour using continuum damage mechanics.

The here presented methods have been applied to relatively simple geometrical and loading configurations, i.e. by modelling free stent balloon expansion or by modelling blood vessels as hyperelastic materials. To accurately model the interaction of an absorbable scaffold with a blood vessel – during deployment and during absorption – also reliable models for the blood vessel have to be taken into account. This means that not only a correct response of the blood vessel to stent expansion has to be modelled – i.e. plastic deformation of the fatty plaque and permanent deformation or rupture of the blood vessel layers – but also the subsequent remodelling and healing of the blood vessel. Indeed, purely elastic blood vessels will return to their original shape when the the stent gradually loses its mechanical strength.

7.3 Future validation

To be clinically applicable, the here developed modelling strategies should be thoroughly validated. In general, validation of the mechanical and degradation behaviour of biodegradable stents is hindered by the small size of the devices, the large variability in loading conditions and mechanical boundary conditions, and the difficulty to asses the *in vivo* interaction of the devices with the surrounding tissues.

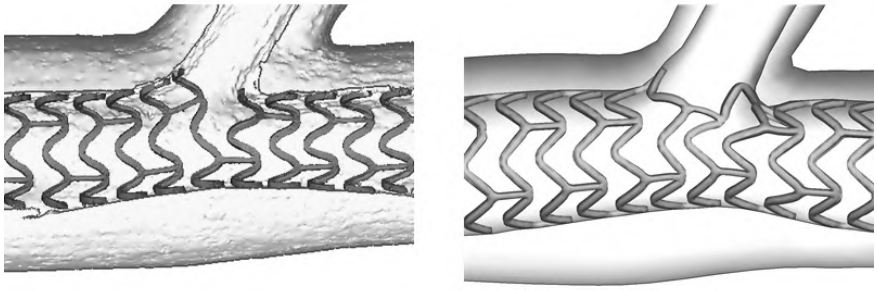

Figure 7.2: Qualitative comparison between a micro-CT reconstructed geometry of an absorbable Abbott BVS inside a 3D-printed silicone bifurcation model with the virtual deployment of a bioresorbable stent model inside a bifurcated blood vessel.

Since it is quasi impossible, with current technology, to obtain degradation characteristics of biodegradable devices *in vivo*, validation of the mechanical behaviour of biodegradable stents will be confined to comparing the simulated geometrical configuration of the stent and surrounding tissues, with geometries obtained via in vivo imaging. A very useful imaging modality to visualise the 3D-configuration of stents inside arteries is optical coherence tomography (OCT), which allows to capture micrometer-resolution, images by optical scattering of surrounding media such as biological tissues or stent struts. An OCT probe can be placed onto a catheter tip to minimally invasive retrieve an accurate and detailed 3D geometry of a coronary stent *in vivo* [45]. This 3D geometry could be measured at different time points during stent degradation and then be compared with the geometries resulting from the computer simulations.

A preliminary validation study was done in collaboration with prof. dr. Peter Smits, MD, and Kees-Jan Royaards, MD, from Maasstad Hospital (Rotterdam, The Netherlands) and dr. Peter Mortier from FEops, a spin-off company from the University of Ghent (Belgium). Here, the aim was to assess the applicability of biodegradable stents for coronary bifurcation stenting. This was done *in vitro* by implanting a series of absorbable BVS stents from Abbott inside 3D-printed silicone bifurcation models, under physiological conditions by using a warm water bath at 37°C. The implanted stents and silicone models were then converted to 3D-computer geometries via micro-CT imaging. This was done at the Centre for X-ray Tomography of the Ghent University (UGCT). The 3D-reconstructed geometries were then compared with data resulting from computer simulations by making use of the balloon expansion strategy and the material model described in Chapter 6. The deployment of the stent is shown in Figure 7.1 and includes opening of the stent strut cage towards the bifurcation side branch by using a second balloon. A qualitative comparison between the micro-CT reconstructed geometry and the simulation outcome is made in Figure 7.2, showing good overall correspondence between the *in vitro* and *in silico* geometries.

7.4 Conclusion

The aim of this research was to expand the finite element modelling tools that have been developed to investigate the mechanical behaviour of minimally invasive devices such as stents to a novel type of stents, the biodegradable stents. To be able to do so, material and degradation models had to be implemented that are able to sufficiently

capture the complex mechanical and degradational behaviour of these devices. During this research, existing explicit finite element analysis strategies have been expanded to be used with an implicit finite element solver. By using an implicit solver, simulation times can be significantly reduced and the reliability of the simulation output increased. Assessment of experimental data to serve as input for the material and degradation models used in this thesis was based on *in vitro* bench testing. In future, better experimental data, preferably based on *in vivo* measurements, will further increase the reliability and clinical applicability of the here investigated modelling strategies.

Bibliography

[1] Abbott. Abbott receives CE Mark approval for world's first drug-eluting bioresorbable vascular scaffold for treatment of coronary artery disease. Press release, January 2011.

[2] Abbott. *Absorb Bioresorbable Vascular Scaffold System*. Abbott Vascular, 3200 Lakeside Drive, Santa Clara, Ca 95054-2807 USA, 2012.

[3] Alexandre Abizaid, Johannes Brachmann, Jose D. Costa, Dariusz Dudek, Norbert Frey, Matthias Heigert, Matthias Lutz, Axel Schmermund, and Jeffrey Anderson. TCT-39 12-Month Angiographic and Clinical Results of the ReZolve(r) Sirolimus-Eluting Bioresorbable Coronary Scaffold: The RESTORE trial. *Journal of the American College of Cardiology*, 62(18_S1):B13, 2013.

[4] Ryan D Alexy and Daniel S Levi. Materials and manufacturing technologies available for production of a pediatric bioabsorbable stent. *BioMed research international*, 2013, 2013.

[5] Ellen M Arruda and Mary C Boyce. A three-dimensional constitutive model for the large stretch behavior of rubber elastic materials. *Journal of the Mechanics and Physics of Solids*, 41(2):389–412, 1993.

[6] Andrej Atrens, Ming Liu, and Nor Ishida Zainal Abidin. Corrosion mechanism applicable to biodegradable magnesium implants. *Materials Science and Engineering: B*, 176(20):1609–1636, 2011.

[7] Rafael A Auras, Loong-Tak Lim, Susan EM Selke, and Hideto Tsuji. *Poly (lactic acid): synthesis, structures, properties, processing, and applications*, volume 10. John Wiley & Sons, 2011.

[8] F. Auricchio, M. Conti, A. Ferrara, S. Morganti, and A. Reali. Patient-specific finite element analysis of carotid artery stenting: a focus on vessel modeling. *International Journal for Numerical Methods in Biomedical Engineering*, 29(6), 2013.

[9] M. Azaouzi, A. Makradi, and S. Belouettar. Numerical investigations of the structural behavior of a balloon expandable stent design using finite element method. *Computational Materials Science*, 72(0):54 – 61, 2013.

[10] Jörgen S. Bergström. *Large Strain Time-Dependent Behavior of Elastomeric Materials*. PhD thesis, Massachusetts Institute of Technology, 1999.

[11] J.S. Bergstrom, S.M. Kurtz, C.M. Rimnac, and A.A. Edidin. Constitutive modeling of ultra-high molecular weight polyethylene under large-deformation and cyclic loading conditions. *Biomaterials*, 23(11):2329–2343, 2002.

[12] Plamen Bokov. *Experimental and numerical description of the interaction between a biodegradable stent and the arterial wall*. PhD thesis, Paris 7, 2011.

[13] EndaL. Boland, Rosa Shine, Nicola Kelly, CaoimheA. Sweeney, and PeterE. McHugh. A Review of Material Degradation Modelling for the Analysis and Design of Bioabsorbable Stents. *Annals of Biomedical Engineering*, pages 1–16, 2015.

[14] Christos V Bourantas, Yaojun Zhang, Vasim Farooq, Hector M Garcia-Garcia, Yoshinobu Onuma, and Patrick W Serruys. Bioresorbable scaffolds: current evidence and ongoing clinical trials. *Current cardiology reports*, 14(5):626–634, 2012.

[15] Franz Bozsak, Jean-Marc Chomaz, and Abdul I Barakat. Modeling the transport of drugs eluted from stents: physical phenomena driving drug distribution in the arterial wall. *Biomechanics and modeling in mechanobiology*, 13(2):327–347, 2014.

[16] Carlo Briguori, Cristiano Sarais, Paolo Pagnotta, Francesco Liistro, Matteo Montorfano, Alaide Chieffo, Fabio Sgura, Nicola Corvaja, Remo Albiero, Goran Stankovic, et al. In-stent restenosis in small coronary arteries: impact of strut thickness. *Journal of the American College of Cardiology*, 40(3):403–409, 2002.

[17] Jia-Hui Chen, Yi-Zhe Wu, Li Shen, Feng Zhang, Zhi-Feng Yao, Jia-Sheng Yin, Meng Ji, Qi-Bing Wang, Lei Ge, Ju-Ying Qian, et al. First-in-man Implantation of the XINSORB Bioresorbable Sirolimus-eluting Scaffold in China. *Chinese medical journal*, 128(9):1275, 2015.

[18] Antonio Colombo and Evangelia Karvouni. Biodegradable stents: "fulfilling the mission and stepping away". *Circulation*, 102(4):371–373, 2000.

[19] HS da Costa-Mattos, IN Bastos, and JACP Gomes. A simple model for slow strain rate and constant load corrosion tests of austenitic stainless steel in acid aqueous solution containing sodium chloride. *Corrosion Science*, 50(10):2858–2866, 2008.

[20] Carlo D'Angelo, Paolo Zunino, Azzurra Porpora, Stefano Morlacchi, and Francesco Migliavacca. Model Reduction Strategies Enable Computational Analysis of Controlled Drug Release from Cardiovascular Stents. *SIAM Journal on Applied Mathematics*, 71(6):2312–22, 2011.

[21] M. De Beule, R. Van Impe, B. Verhegghe, P. Segers, and P. Verdonck. Finite element analysis and stent design: Reduction of dogboning. *Technology and Health Care*, 14(4):233 – 241, 2006.

[22] Nic Debusschere, Patrick Segers, Peter Dubruel, Benedict Verhegghe, and Matthieu De Beule. A finite element strategy to investigate the free expansion behaviour of a biodegradable polymeric stent. *Journal of biomechanics*, 2015.

[23] Roberto Diletti, Patrick W Serruys, Vasim Farooq, Krishnankutty Sudhir, Cecile Dorange, Karine Miquel-Hebert, Susan Veldhof, Richard Rapoza, Yoshinobu Onuma, Hector M Garcia-Garcia, et al. ABSORB II randomized controlled trial: a clinical evaluation to compare the safety, efficacy, and performance of the Absorb everolimus-eluting bioresorbable vascular scaffold system against the XIENCE everolimus-eluting coronary stent system in the treatment of subjects with ischemic heart disease caused by de novo native coronary artery lesions: rationale and study design. *American heart journal*, 164(5):654–663, 2012.

[24] D. Dudek, Y. Onuma, J.A. Ormiston, L. Thuesen, K. Miquel-Hebert, and P.W. Serruys. Four-year clinical follow-up of the ABSORB everolimus-eluting bioresorbable vascular scaffold in

patients with de novo coronary artery disease: the ABSORB trial. *EuroIntervention: journal of EuroPCR in collaboration with the Working Group on Interventional Cardiology of the European Society of Cardiology*, 7(9):1060–1061, 2012.

[25] Stephen G. Ellis, Dean J. Kereiakes, D. Christopher Metzger, Ronald P. Caputo, David G. Rizik, Paul S. Teirstein, Marc R. Litt, Annapoorna Kini, Ameer Kabour, Steven O. Marx, Jeffrey J. Popma, Robert McGreevy, Zhen Zhang, Charles Simonton, and Gregg W. Stone. Everolimus-Eluting Bioresorbable Scaffolds for Coronary Artery Disease. *New England Journal of Medicine*, 373(20):1905–1915, 2015. PMID: 26457558.

[26] R. Erbel, C. Di Mario, J. Bartunek, J. Bonnier, B. de Bruyne, F.R. Eberli, P. Erne, M. Haude, B. Heublein, M. Horrigan, et al. Temporary scaffolding of coronary arteries with bioabsorbable magnesium stents: a prospective, non-randomised multicentre trial. *The Lancet*, 369(9576):1869–1875, 2007.

[27] Paul Erne, Matthias Schier, and Therese J Resink. The road to bioabsorbable stents: reaching clinical reality? *Cardiovascular and interventional radiology*, 29(1):11–16, 2006.

[28] S.K. Eswaran, J.A. Kelley, J.S. Bergstrom, and V.L. Giddings. Material Modeling of Polylactide. *SIMULIA Customer Conference*, pages 1–11, 2011.

[29] S. Garg and P.W. Serruys. *Coronary Stents: Current Status; Looking Forward*. Elsevier, 2010.

[30] D Gastaldi, V Sassi, L Petrini, M Vedani, S Trasatti, and F Migliavacca. Continuum damage model for bioresorbable magnesium alloy devices-Application to coronary stents. *Journal of the mechanical behavior of biomedical materials*, 4(3):352–365, 2011.

[31] Dario Gastaldi, Valentina Sassi, Lorenza Petrini, Maurizio Vedani, Stefano P Trasatti, and Francesco Migliavacca. Continuum Damage Model for Biodegradable Magnesium Alloy Stent. *Advanced Materials Research*, 138:85–91, 2010.

[32] B.D. Gogas, V. Farooq, Y. Onuma, and P.W. Serruys. The ABSORB bioresorbable vascular scaffold: an evolution or revolution in interventional cardiology. *Hellenic J Cardiol*, 53(4):301–309, 2012.

[33] Bill D Gogas. Bioresorbable scaffolds for percutaneous coronary interventions. *Global cardiology science & practice*, 2014(4):409, 2014.

[34] Achim Göpferich. Mechanisms of polymer degradation and erosion. *Biomaterials*, 17(2):103–114, 1996.

[35] J.A. Grogan, S.B. Leen, and P.E. McHugh. Optimizing the design of a bioabsorbable metal stent using computer simulation methods. *Biomaterials*, 34(33):8049–8060, 2013.

[36] J.A. Grogan, B.J. O'Brien, S.B. Leen, and P.E. McHugh. A corrosion model for bioabsorbable metallic stents. *Acta biomaterialia*, 7(9):3523–3533, 2011.

[37] James Grogan. *The Mechanical Performance of Permanent and Bioabsorbable Metal Stents*. PhD thesis, National University of Ireland, Galway, 2012.

[38] Rowan Technology Group. Galvanic Series, 2015.

[39] Xue-Nan Gu and Yu-Feng Zheng. A review on magnesium alloys as biodegradable materials. *Frontiers of Materials Science in China*, 4(2):111–115, 2010.

[40] M. Haude, R. Erbel, S. Verheye, R. Waksman, N. Weissman, H. Degen, D. Boese, P. Erne, and J. Koolen. Comparison of intermediate term late lumen loss after coronary implantation of bare or paclitaxel eluting absorbable metal scaffolds: results from progress-ams and biosolve-1 trials. *Journal of the American College of Cardiology*, 59(13s1):E203–E203, 2012.

[41] Michael Haude, Raimund Erbel, Paul Erne, Stefan Verheye, Hubertus Degen, Dirk Böse, Paul Vermeersch, Inge Wijnbergen, Neil Weissman, Francesco Prati, et al. Safety and performance of the drug-eluting absorbable metal scaffold (DREAMS) in patients with de-novo coronary lesions: 12 month results of the prospective, multicentre, first-in-man BIOSOLVE-I trial. *The Lancet*, 381(9869):836–844, 2013.

[42] Anna Louise Hawkes, Madeleine Nowak, Benjamin Bidstrup, and Richard Speare. Outcomes of coronary artery bypass graft surgery. *Vascular health and risk management*, 2(4):477, 2006.

[43] H. Hermawan, D. Dubé, and D. Mantovani. Developments in metallic biodegradable stents. *Acta Biomaterialia*, 6(5):1693 – 1697, 2010. The THERMEC'2009 Biodegradable Metals.

[44] James B. Hermiller. ABSORB III and IV: Evaluating the Safety and Effectiveness of the Absorb Bioresorbable Vascular Scaffold, 2015.

[45] Nick Hiltrop, Dries De Cock, Bert Ferdinande, and Tom Adriaenssens. Detailed in vivo visualization of stent fracture causing focal restenosis using 3D reconstruction software for high-resolution optical coherence tomography images. *European Heart Journal-Cardiovascular Imaging*, page jet273, 2014.

[46] David R Holmes, Martin B Leon, Jeffrey W Moses, Jeffrey J Popma, Donald Cutlip, Peter J Fitzgerald, Charles Brown, Tim Fischell, Shing Chiu Wong, Mark Midei, et al. Analysis of 1-year clinical outcomes in the SIRIUS trial a randomized trial of a sirolimus-eluting stent versus a standard stent in patients at high risk for coronary restenosis. *Circulation*, 109(5):634–640, 2004.

[47] GerhardA. Holzapfel, ThomasC. Gasser, and RayW. Ogden. A New Constitutive Framework for Arterial Wall Mechanics and a Comparative Study of Material Models. *Journal of elasticity and the physical science of solids*, 61(1-3):1–48, 2000.

[48] Hao-Ming Hsiao, Yi-Hsiang Chiu, Kuang-Huei Lee, and Chien-Han Lin. Computational modeling of effects of intravascular stent design on key mechanical and hemodynamic behavior. *Computer-Aided Design*, 44(8):757 – 765, 2012.

[49] F. Iannaccone, N. Debusschere, S. De Bock, M. De Beule, D. Van Loo, F. Vermassen, P. Segers, and B. Verhegghe. The influence of vascular anatomy on carotid artery stenting: A parametric study for damage assessment. *Journal of biomechanics*, 47(4):890–898, 2014.

[50] Alfonso Ielasi, Azeem Latib, and Antonio Colombo. Current and future drug-eluting coronary stent technology. *Expert Review of Cardiovascular Therapy*, 9:485–503, 2011.

[51] Javaid Iqbal, Yoshinobu Onuma, John Ormiston, Alexandre Abizaid, Ron Waksman, and Patrick Serruys. Bioresorbable scaffolds: rationale, current status, challenges, and future. *European heart journal*, 35(12):765–776, 2014.

[52] Jimmy X Jia, Guangling Song, and Andrej Atrens. Influence of geometry on galvanic corrosion of AZ91D coupled to steel. *Corrosion Science*, 48(8):2133–2153, 2006.

[53] D.E. Kiousis, A.R. Wulff, and G.A. Holzapfel. Experimental studies and numerical analysis of the inflation and interaction of vascular balloon catheter-stent systems. *Annals of biomedical engineering*, 37(2):315–330, 2009.

[54] Tanja Kraus, Frank Moszner, Stefan Fischerauer, Michael Fiedler, Elisabeth Martinelli, Johannes Eichler, Frank Witte, Elmar Willbold, Michael Schinhammer, Martin Meischel, et al. Biodegradable Fe-based alloys for use in osteosynthesis: Outcome of an in vivo study after 52weeks. *Acta biomaterialia*, 10(7):3346–3353, 2014.

[55] H Laufman and T Rubel. Synthetic absorable sutures. *Surgery, gynecology & obstetrics*, 145(4):597–608, 1977.

[56] Michael S Lee, Daniel Jurewitz, Joseph Aragon, James Forrester, Raj R Makkar, and Saibal Kar. Stent fracture associated with drug-eluting stents: Clinical characteristics and implications. *Catheterization and Cardiovascular Interventions*, 69(3):387–394, 2007.

[57] Solki Lee, Chang Woo Lee, and Chang-Soo Kim. FEA Study on the Stress Distributions in the Polymer Coatings of Cardiovascular Drug-Eluting Stent Medical Devices. *Annals of biomedical engineering*, 42(9):1952–1965, 2014.

[58] Jean Lemaitre and Rodrigue Desmorat. *Engineering damage mechanics: ductile, creep, fatigue and brittle failures*. Springer Science & Business Media, 2005.

[59] Jean Lemaitre and Horst Lippmann. *A course on damage mechanics*, volume 2. Springer Berlin, 1996.

[60] Colin D Mathers and Dejan Loncar. Projections of global mortality and burden of disease from 2002 to 2030. *Plos med*, 3(11):e442, 2006.

[61] Francesco Migliavacca, Lorenza Petrini, Maurizio Colombo, Ferdinando Auricchio, and Riccardo Pietrabissa. Mechanical behavior of coronary stents investigated through the finite element method. *Journal of Biomechanics*, 35(6):803 – 811, 2002.

[62] Marie-Claude Morice, Patrick W Serruys, Paul Barragan, Christoph Bode, Gerrit-Anne Van Es, Hans-Peter Stoll, David Snead, Laura Mauri, Donald E Cutlip, and Eduardo Sousa. Long-term clinical outcomes with sirolimus-eluting coronary stents: five-year results of the RAVEL trial. *Journal of the American college of cardiology*, 50(14):1299–1304, 2007.

[63] Stefano Morlacchi, Sebastian George Colleoni, Rubén Cárdenes, Claudio Chiastra, Jose Luis Diez, Ignacio Larrabide, and Francesco Migliavacca. Patient-specific simulations of stenting procedures in coronary bifurcations: two clinical cases. *Medical engineering & physics*, 35(9):1272–1281, 2013.

[64] P. Mortier, M. De Beule, P. Segers, P. Verdonck, and B. Verhegghe. Virtual bench testing of new generation coronary stents. *EuroIntervention*, 7(3):369–376, 2011.

[65] M.D. Moses, Jeffrey W., M.D. Leon, Martin B., M.D. Popma, Jeffrey J., M.D. Fitzgerald, Peter J, M.D. Holmes, David R., MD O'Shaughnessy, Charles, M.D. Caputo, Ronald P., M.D. Kereiakes, Dean J., M.D. Williams, David O., M.D. Teirstein, Paul S., B.A. Jaeger, Judith L., and M.D. Kuntz, Richard E. Sirolimus-eluting stents versus standard stents in patients with stenosis in a native coronary artery. *The New England journal of medicine*, 349(14):1315–23, Oct 02 2003.

[66] Masataka Nakano, Fumiyuki Otsuka, Kazuyuki Yahagi, Kenichi Sakakura, Robert Kutys, Elena R Ladich, Aloke V Finn, Frank D Kolodgie, and Renu Virmani. Human autopsy study of drug-eluting stents restenosis: histomorphological predictors and neointimal characteristics. *European heart journal*, 34(42):3304–3313, 2013.

[67] Melanie Nichols, Nick Townsend, Peter Scarborough, and Mike Rayner. Cardiovascular disease in Europe 2014: epidemiological update. *European heart journal*, 35(42):2950–2959, 2014.

[68] National Institutes of Health. NIH home page. `http://www.nhlbi.nih.gov`, 2016.

[69] Y. Onuma and P.W. Serruys. Bioresorbable Scaffold The Advent of a New Era in Percutaneous Coronary and Peripheral Revascularization? *Circulation*, 123(7):779–797, 2011.

[70] Yoshinobu Onuma, Scot Garg, Takayuki Okamura, J Ligthart, R Jan Van Geuns, PJ De Feyter, and PW Serruys. Ten-year follow-up of the IGAKI-TAMAI stent. *A posthumous tribute to the scientific work of Dr. Hideo Tamai EuroIntervention*, 5(Suppl F):F109–11, 2009.

[71] Yosinobu Onuma, John Ormiston, and Patrick W Serruys. Bioresorbable scaffold technologies. *Circulation Journal*, 75(3):509–520, 2011.

[72] Yosinobu Onuma and Patrick W Serruys. Bioresorbable scaffold the advent of a new era in percutaneous coronary and peripheral revascularization? *Circulation*, 123(7):779–797, 2011.

[73] John A Ormiston and Patrick WS Serruys. Bioabsorbable coronary stents. *Circulation: Cardiovascular Interventions*, 2(3):255–260, 2009.

[74] Matthias Peuster, Phillip Beerbaum, Friedrich-Wilhelm Bach, and Hansjoerg Hauser. Are resorbable implants about to become a reality? *Cardiology in the Young*, 16(02):107–116, 2006.

[75] Matthias Peuster, Carola Hesse, Tirza Schloo, Christoph Fink, Philipp Beerbaum, and Christian von Schnakenburg. Long-term biocompatibility of a corrodible peripheral iron stent in the porcine descending aorta. *Biomaterials*, 27(28):4955–4962, 2006.

[76] Duane S Pinto, Gregg W Stone, Stephen G Ellis, David A Cox, James Hermiller, Charles OâĂŹShaughnessy, J Tift Mann, Roxana Mehran, Yingbo Na, Mark Turco, et al. Impact of routine angiographic follow-up on the clinical benefits of paclitaxel-eluting stents: results from the TAXUS-IV trial. *Journal of the American College of Cardiology*, 48(1):32–36, 2006.

[77] P Poncin, C Millet, J Chevy, and JL Proft. Comparing and optimizing Co-Cr tubing for stent applications. In *Proceedings of the Materials and Processes for Medical Devices Conference*, pages 279–283, 2004.

[78] Jean-Philippe Ponthot. Unified stress update algorithms for the numerical simulation of large deformation elasto-plastic and elasto-viscoplastic processes. *International Journal of Plasticity*, 18(1):91–126, 2002.

[79] Agung Purnama, Hendra Hermawan, and Diego Mantovani. Biodegradable Metal Stents: A Focused Review on Materials and Clinical Studies. *Journal of Biomaterials and Tissue Engineering*, 4(11):868–874, 2014.

[80] Steve Ramcharitar and Patrick W Serruys. Fully biodegradable coronary stents. *American journal of cardiovascular drugs*, 8(5):305–314, 2008.

[81] DS Rosa, I Chiovatto Neto, MR Calil, AG Pedroso, CP Fonseca, and S Neves. Evaluation of the thermal and mechanical properties of poly (ε-caprolactone), low-density polyethylene, and their blends. *Journal of applied polymer science*, 91(6):3909–3914, 2004.

[82] P.W. Serruys, Y. Onuma, H.M. Garcia-Garcia, T. Muramatsu, R.J. van Geuns, B. de Bruyne, D. Dudek, L. Thuesen, P.C. Smits, B. Chevalier, et al. Dynamics of vessel wall changes following the implantation of the Absorb everolimus-eluting bioresorbable vascular scaffold: a multi-imaging modality study at 6, 12, 24 and 36 months. *EuroIntervention: journal of EuroPCR in collaboration with the Working Group on Interventional Cardiology of the European Society of Cardiology*, 2013.

[83] JC Simo. On a fully three-dimensional finite-strain viscoelastic damage model: formulation and computational aspects. *Computer methods in applied mechanics and engineering*, 60(2):153–173, 1987.

[84] Simulia. *Abaqus theory manual*. Dassault Systèmes, 2012.

[85] Ferdinand Singer, Thomas Distler, and Sannakaisa Virtanen. Long-term Corrosion Behavior of Poly-L-lactic Acid Coated Magnesium in Dulbecco's Modified Eagle Medium at Body Temperature. *Int. J. Electrochem. Sci*, 9:7965–7976, 2014.

[86] Ilke Sipahi, M Hakan Akay, Sinan Dagdelen, Arie Blitz, and Cem Alhan. Coronary artery bypass grafting vs percutaneous coronary intervention and long-term mortality and morbidity in multivessel disease: meta-analysis of randomized clinical trials of the arterial grafting and stenting era. *JAMA internal medicine*, 174(2):223–230, 2014.

[87] João S Soares, James E Moore, and Kumbakonam R Rajagopal. Modeling of deformation-accelerated breakdown of polylactic acid biodegradable stents. *Journal of medical devices*, 4(4):041007, 2010.

[88] João S Soares, Kumbakonam R Rajagopal, and James E Moore Jr. Deformation-induced hydrolysis of a degradable polymeric cylindrical annulus. *Biomechanics and modeling in mechanobiology*, 9(2):177–186, 2010.

[89] JoaoS. Soares and Jr. Moore, JamesE. Biomechanical Challenges to Polymeric Biodegradable Stents. *Annals of Biomedical Engineering*, pages 1–20, 2015.

[90] J.S. Soares, J.E. Moore Jr, and K.R. Rajagopal. Constitutive framework for biodegradable polymers with applications to biodegradable stents. *Asaio Journal*, 54(3):295–301, 2008.

[91] Guangling Song, Andrej Atrens, and David StJohn. An hydrogen evolution method for the estimation of the corrosion rate of magnesium alloys. *Magnesium technology*, 2001:255–262, 2001.

[92] SM Stivaros, LR Williams, C Senger, L Wilbraham, and Hans-Ulrich Laasch. Woven polydioxanone biodegradable stents: a new treatment option for benign and malignant oesophageal strictures. *European radiology*, 20(5):1069–1072, 2010.

[93] M.D. Stone, Gregg W., M.D. Ellis, Stephen G., M.D. Cox, David A., M.D. Hermiller, James, MD O'Shaughnessy, Charles, M.D. Mann, James T., M.D. Turco, Mark, M.D. Caputo, Ronald, M.D. Bergin, Patrick, M.D. Greenberg, Joel, M.D. Popma, Jeffrey J., and M.D. Russell, Mary E. A Polymer-Based, Paclitaxel-Eluting Stent in Patients with Coronary Artery Disease. *The New England journal of medicine*, 350(3):221–31, Jan 15 2004.

[94] B. Verhegghe. pyFormex home page. `http://www.nongnu.org/pyformex`, 2014.

[95] Friederike von Burkersroda, Luise Schedl, and Achim Göpferich. Why degradable polymers undergo surface erosion or bulk erosion. *Biomaterials*, 23(21):4221–4231, 2002.

[96] M Vorpahl, R Virmani, E Ladich, and AV Finn. Vascular remodeling after coronary stent implantation. *Minerva cardioangiologica*, 57(5):621–628, 2009.

[97] Ron Waksman, Raimund Erbel, Carlo Di Mario, Jozef Bartunek, Bernard de Bruyne, Franz R Eberli, Paul Erne, Michael Haude, Mark Horrigan, Charles Ilsley, et al. Early-and long-term intravascular ultrasound and angiographic findings after bioabsorbable magnesium stent implantation in human coronary arteries. *JACC: Cardiovascular Interventions*, 2(4):312–320, 2009.

[98] Ron Waksman and Rajbabu Pakala. Biodegradable and bioabsorbable stents. *Current pharmaceutical design*, 16(36):4041–4051, 2010.

[99] Martin Werner, Antonio Micari, Angelo Cioppa, Giuseppe Vadalà, Andrej Schmidt, Horst Sievert, Paolo Rubino, Annalisa Angelini, Dierk Scheinert, and Giancarlo Biamino. Evaluation of the biodegradable peripheral Igaki-Tamai stent in the treatment of de novo lesions in the superficial femoral artery: the GAIA study. *JACC: Cardiovascular Interventions*, 7(3):305–312, 2014.

[100] Jens Wiebe, Holger M. Nef, and Christian W. Hamm. Current Status of Bioresorbable Scaffolds in the Treatment of Coronary Artery Disease. *Journal of the American College of Cardiology*, 64(23):2541–2551, 2014.

[101] W. Wu, D. Gastaldi, K. Yang, L. Tan, L. Petrini, and F. Migliavacca. Finite element analyses for design evaluation of biodegradable magnesium alloy stents in arterial vessels. *Materials Science and Engineering: B*, 176(20):1733–1740, 2011.

[102] W Wu, L Petrini, D Gastaldi, T Villa, M Vedani, E Lesma, B Previtali, and F Migliavacca. Finite element shape optimization for biodegradable magnesium alloy stents. *Annals of biomedical engineering*, 38(9):2829–2840, 2010.

[103] Wei Wu, Shanshan Chen, Dario Gastaldi, Lorenza Petrini, Diego Mantovani, Ke Yang, Lili Tan, and Francesco Migliavacca. Experimental data confirm numerical modeling of the degradation process of magnesium alloys stents. *Acta biomaterialia*, 9(10):8730–8739, 2013.

[104] J Xiao and S Chaudhuri. Predictive modeling of localized corrosion: an application to aluminum alloys. *Electrochimica Acta*, 56(16):5630–5641, 2011.

[105] WU Yizhe, SHEN Li, YAO Zhifeng, GE Lei, Qibing Wang, Juying Qian, HU Xi, XIE Jian, and GE Junbo. TCT-431 Long-term Angiographic and Optical Coherence Tomography Follow-up of XINSORB Scaffold in Porcine Coronary Model. *Journal of the American College of Cardiology*, 64(11_S), 2014.

[106] XB Zhang, GY Yuan, XX Fang, ZZ Wang, and T Zhang. Effects of solution treatment on yield ratio and biocorrosion behaviour of as-extruded Mg-Nd-Zn-Zr alloy for cardiovascular stent application. *Materials Science and Technology*, 28(3):155–158, 2013.

[107] Xiaobo Zhang, Guangyin Yuan, Lin Mao, Jialin Niu, and Wenjiang Ding. Biocorrosion properties of as-extruded Mg–Nd–Zn–Zr alloy compared with commercial AZ31 and WE43 alloys. *Materials Letters*, 66(1):209–211, 2012.

[108] Yaojun Zhang, Christos V Bourantas, Vasim Farooq, Takashi Muramatsu, Roberto Diletti, Yoshinobu Onuma, Hector M Garcia-Garcia, Patrick W Serruys, et al. Bioresorbable scaffolds in the treatment of coronary artery disease. *Med Devices (Auckl)*, 6:37–48, 2013.